ナノフォトニクス光集積素子に関する研究

博士学位論文

Research on nano-photonics integrated devices
ナノフォトニクス光集積素子に関する研究

Yu　Jiyao

于　済瑶

東北大学大学院 工学研究科
通信工学専攻

令和元年 8 月

Abstract

With the fast development of information technology and the demands for high speed and high quality communication network, information processing, and data storage and interconnect, the path of modern communication and signal processing systems are towards the high speed, large capacity, low power consumption and low cost. Photonics integrated chips (PICs) are treated as one of the newest technology in this field. In this thesis, several kinds of photonics integrated devices based on plasmonic waveguides and dielectric waveguides are presented and investigated for advanced features. Both plasmonic waveguides and dielectric waveguides play fundamental roles in modern PICs. Dielectric silicon waveguides, obeying the total internal reflection, occupies the important position in Silicon photonics. Plasmonic waveguides, in which surface plasmon polaritons (SPPs) on the metal/dielectric interface form the guided modes, can achieve nanometer-scale field confinement.

In chapter 1, the demands and development of photonics integrated devices are introduced. The trends of high speed, high integration and low power consumption on both chip-size interconnect and interconnect between data centers are the main drying force for transmission using photons instead of electrons. Then, the motivation and outline of this thesis are introduced.

In chapter 2, the waveguide theory of slab dielectric waveguide and plasmonic waveguide are introduced. The numerical calculation methods for mode and transmission characteristics are introduced at the same time.

In chapter 3, a kind of waveguide coupler between hybrid plasmonic waveguides and dielectric slot waveguides is proposed. The waveguide coupler serves as the interconnection between the two kinds of waveguides. The mode mismatch are investigated via numerical calculation and are explained in two ways: the mismatch of effective mode area and reflectivity. Calculation results show that both mismatch can be minimum via proper design of two kinds of waveguides. Besides, a kind of highly efficient mode converter are introduced along with the funnel effect, which are

explained by plotting the Poynting vector.

In chapter 4, a kind of side-coupled type plasmonic Fabry-Perot waveguide filter is proposed. The physical propagation model is analyzed by the scattering matrix and the coupling mode theory (CMT). The total devices are divided into several parts and applied scattering matrix in each part. The spatial and spectral responses obtained by the proposed model showed a good agreement with numerical simulations. These results could be useful in analyses of other similar plasmonic filter designs with side-coupled structures, and demonstrate the potentials for applications in optical integrated wavelength selectors or filters with a ultra-wide FSR.

In chapter 5, the slab space optics is investigated under the usage of planar slab waveguides. Compared with the traditional dielectric strip and ridge waveguides, the slab waveguides own the advantage of low propagation loss and large area. With these merits, several kinds of passive integrated devices are designed. First, a kind of planar chiral metamaterials (PCMs) is investigated for the characteristics of wavelength filtering. The multi-patterened PCMs are proved for the application on near-infrared imaging system. Then, a kind of dual-layer grating coupler is designed for vertical coupling between fibers and waveguides. Such grating coupler is the first report of fiber-chip coupling with characteristics of dual optical bands and dual polarization states. The design also owns the merit of function style of vertical coupling, which reduce the assemble difficulty. The two layer FP resonance is also investigated for high coupling efficiency. Finally, a kind of waveguide crossing coupler is analyzed based on curved silica-mirror. The fundamental propagation characteristics of Gaussian beams are analyzed with ABCD' law. The device also shows high bandwidth than other waveguide crossing design, like a MMI coupler.

In chapter 6, the summary of the whole thesis and the future work are drawn.

Keywords: Photonic integrated chips; Silicon photonics; Plasmonic photonics; Waveguide coupler; Waveguide crossing; Waveguide filter; Grating coupler; 2D-FDTD

Table of contents

List of figures

Chapter 1 Introduction

Photonics integrated devices are the promising building blocks in the field of information industry in the future world, which ranges from the optical communication [1-3], optical computing [4-6], biomedical applications [7-9], optical sensing [10-12], and even in quantum information theory [13-15]. In this chapter, the fundamental background of demands and developments of photonics integrated devices are introduced, in which the plasmonic waveguides and dielectric waveguides play important roles. Finally, the motivation and outline of the thesis is introduced.

1.1 Demands of photonics integrated chips

With the increasing history of the 21th century, the information theory reforms its shape and requires a growing demands of new technology. On the one hand, compared with the oldest communication industry, the new concept of big data, cloud computing, internet of thing (IoT), mobile communication, super computers, artificial intelligence (AI) are accustomed to every person in this world. While, on the other hand, the physical devices which support the above applications are growing slowly and facing the strait. Currently, the microelectronic integration technology based on the development of semiconductor industry are gradually facing the physical limitation and difficult to overthrowing the Moore's Law, which predicts that the number of transistors in a dense integrated circuit doubles about every two years in 1965. The line-width of complementary metal oxide semiconductor (CMOS) technology for integration chips fabrication is coming at the 7 nm, meanwhile the scientists and engineers promote the innovation of current technology for sanctifying the Moore's Law, which are difficult ways and facing new problems, like the increasing of cross-talk for neighboring channels, increasing of power consumption and increasing of the heat.

The problem does not only appear in front of the engineers and scientists. The

data explosion appears today is also a large drying force to innovate the current technology for higher communication speed, lower power consumption and so on. A report from IBM and Intel, which relates with the consumer application layer, points out that the amount of data grown almost 90% in the last 2 years [16, 17]. This simple case shows the grown speed of the recent data explosion impressively. The grown speed of data explosion is predicted even faster with the development of the penetration of data analyzing from the 'big data' and the Internet of Things (IoT), due to the huge demands of data analyzing for their applications, like real-time video, web-searching ,and AI, etc. The current data centers are confronted with such serious challenges to catch up with this data explosion. For the above analysis, requirements of wider band-width and high-density degree of integration, for which means wider band-width in another way, are urgent [18]. Meanwhile, the interchip band-width in personal computers, such as a CPU, has an overall bandwidth of about several Tbps, including the CPU-CPU interconnect, CPU-memory interconnect and the in connection with peripherals. The longer reach interconnects are also required with the appearance of mega data centers.

Three trends and requirements of computing systems in data centers are introduced according to the reference [19]. First, the clock frequency of transistors are gradually hit the limitation, although their size are still based on the Moor's law. The requirement of multi-core processors are naturally for keeping the demands of faster growing amount of information. The second is three-dimensional (3-D) packaging, which is mainly applied to increase the capacity of flash memory for the usage of solid-state drive for data storage. As a result, the demands of increasing handling of data quantity in a memory scale is necessary. The third is system in a package (SiP) [20]. The system in a package is the integration of multiple chips or systems in a single package and provides a variety functions with higher flexibility than system on a chip (SoC). The wider bandwidth is all necessary for the above three trends for inter-chip interconnects. Thus, a innovate technology instead of the current large scale integrated chips (LSIs) is urgently desired.

Optical inter-connectors and computers, instead of current microelectronic chips

and micro waves are a solution for the above problems. One the one hand, for large scale data transfer, instead of microwaves, optical waves are used as the carrier for information transmission. Optical wave is a kind of ultra-high frequency electromagnetic waves, especially suitable for high speed information transfer. Scientists and engineers have developed a optical fiber communication network all around the world since the last century. On the other hand, microelectronic chips using electrons as the information carrier in chip scale is gradually replaced by optical waves (photons). The photons owns superiority than electrons in many situations, such as no RC-delay, low power consumption ,etc.

1.2 Photonics integrated chips

As the chapter 1.1 mentioned, the development of electric circuits driven by the Moore's law has faced its limitation for situations of modern society for demands of communication with high bandwidth (speed). The microelectronic with the characteristics of faster and smaller contains billions of transistors in one micro-chip by using the technology of very large scale integration (VLSI) and the dimensions locate at a few of nano-meters. The integration of photonics are another choice instead. The information carrier vectors in photonics can be photonics, solitons, light balls, or plasmons. [21] The usage of photons as the carrier results in many benefits. For example, there are possibilities to transmit information with higher frequency (100 THz) and the ability to confine light in a very small dimensions. In fact, S. T. Miller from the Bell's labs already proposed the possibility of integration of photonics. However, the integration of photonics are still weak and general photonic integrated circuits only contains hundreds of optical components with a high production cost and low effectiveness. The integration of photonics does not follow the Moore's law. The reason can be roughly explained as follows. The integration of micro-electronics is based on a standard, which means a single material and a single production process is applied on a single building circuit. While for photonics, the integration contains a diversity of materials, circuits and production processes. So the development of

integration of photonics is not grown fast as micro-electronics.

Since the beginning of this century, due to the application of the platform of silicon-on-insulator, the silicon photonics have been studied widely. The reason is the unified material-Si and production process- the CMOS process. Based on these ideas, the photonics components are developed using a single material and a single production process. In this way, the level of integration of photonics become easier and cheaper than before, which reverse promotes the development of optical devices and increases the performance of photonics integrated circuits. At the same time, the development of device physics and fabrication technology allow the integration not limited by silicon, but from the semiconductors materials of group III to group V and mainly focus on group IV. The diversity choice of materials make the device more functional from a wide range of passive and active components. The controlling of light become easier and easier and form the basis for future optical network and processor. A series of complexity optical integrated components have been developed and taken into account manipulating light in a wide range of wavelength.

During recent years, additional materials, mainly germanium and III-V semiconductors, have been introduced in silicon photonics to reach efficient building blocks. The complexity of each device has gotten higher and higher to take into account light polarization and performance independence in a broad wavelength range. Manufacturing technology has shifted from a pure CMOS process and still kept in mind CMOS process compatibility, which allows the usage of other materials. The drying forces for the above results come from many aspects. For example, one reason is that the demands of high bandwidth communication from consumer and other is that the need for power consumption and low power dissipation. Other needs come from the application field of telecommunications, sensing areas, medicine, consumer electronics and energy field. The development of silicon photonics will be pushed further by the variety of applications and other new innovative concepts will be developed, such as the quantum information theory and quantum computing. There is no doubt that the silicon photonics will bring revolution and shock the current semiconductor industry.

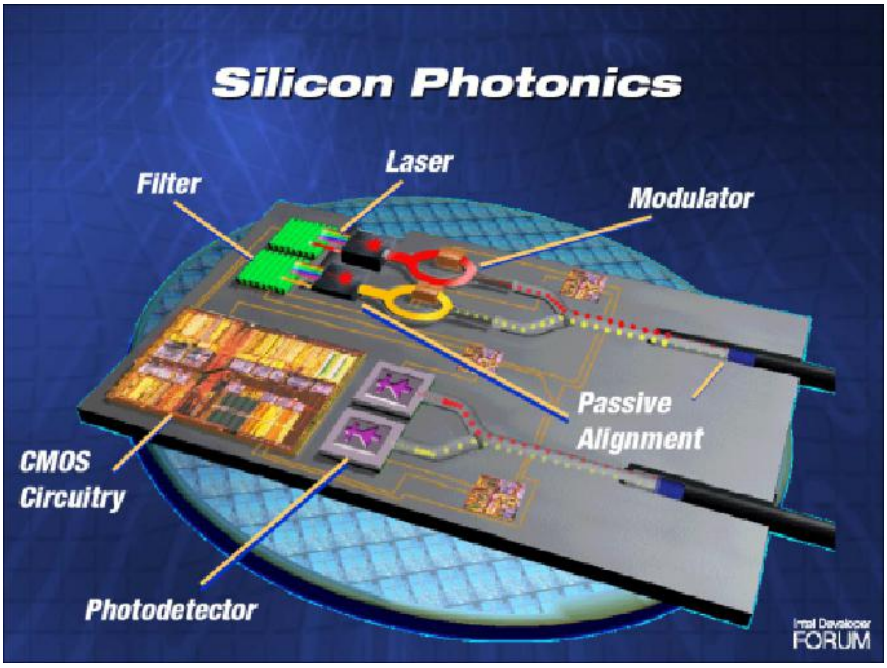

Fig.1 IBM opto-electric integrated system based on silicon photonics

The systems of CMOS-compatible electro-optic integrated circuits (i.e. Silicon photonics) can be roughly shown in the Fig. 1.1 from the reports of IBM, which introduce the opto-electric integrated system. It contains series of active and passive components in one single chips. The active components can be (arrayed) laser sources [22-24], optical modulators [25-27], and photo-detectors [28-30]. The passive components contains optical switches [31-33], waveguide crossings [34-36], grating coupler [37-39], and series of polarization splitters and rotation devices [40-42].

However, it's well known that the operating theory of guiding and confining light in silicon photonics is based on the total internal reflection (TIR), which limits the geometry sizes of silicon photonics components. The diffraction limit makes the integration of silicon photonics in a acceptable range but can not approach more, in which is typically micro-meter range. So what's the next generation technology making scientists towards the nano-meters range? It's clear that the integration of photonics components with nano-meters 'transmission line' will be superior than current technologies.

Typically, nano-meters sized electronic circuits or silicon photonics can not

satisfy the demands. The previous one is inherently slow due to the resistance-capacitance (RC) delay because of the transmission of high frequency signals and the latter one is limited by the diffraction limit and is essentially micro-meters size. It is interesting to show that electromagnetic waves propagate along the interface of metal and dielectric materials was found to overcome the diffraction limit and still hold the optical frequency, which is known as surface plasmons (SPs) or surface plasmons modes. [43-46] Fig. 1.2 shows the unique dispersion relation of the surface plasmon modes (SPPs). These modes come from the interaction of the surface charges and the electromagnetic waves and can be characterized by the wavelength of surface plasmon waves shorter than wavelength in dielectric material, exhibiting thereby sub-wavelength confinement. Among them, the metallic slot waveguide for guiding and confining light in subwavelength range is more attracted. However, due to the strong light-matter interaction, the propagation loss of plasmonic waveguides are still large than that of silicon photonics. This makes the plasmonic can not build the future photonics devices independently.

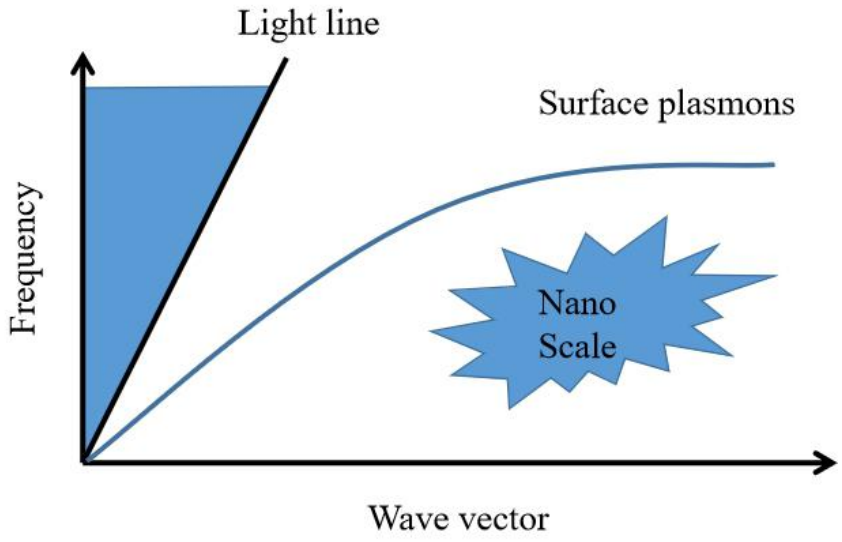

Fig. 2 The unique dispersion relation of surface plasmon polaritons (SPPs)

Thus, future photonic integrated devices will become diversified and combine both silicon photonics and plasmonic photonics together. It's also should note that the

current plasmonic photonics are also developed on the substrate of silicon, which make the combination convenient. The silicon photonics wish be behaved as the transmission line and partial core components and the plasmonic served as the core components. By doing so, the integration density of photonics chip will be increased. For this purpose, the way for the practical usage of plasmonic based photonics components is to build the faster and high density network on a chip for the application in data centers. The combination of plasmonic photonics, silicon photonic as well as the electronic circuits will make the realization of network on a chip with low power consumption, high integration density, enhanced bandwidth and capabilities. In this purpose, low propagation loss silicon photonics can be used for optical transmission line and input-output interface, while plasmonic can be used for small footprint and low power consumption active modulating component and electronic circuits can be used for intelligent controlling mechanisms. The benefits of each technology on-chip is concluded in the Fig. 1.3, in which the comparison of each carrier in the application of information transmission is shown.

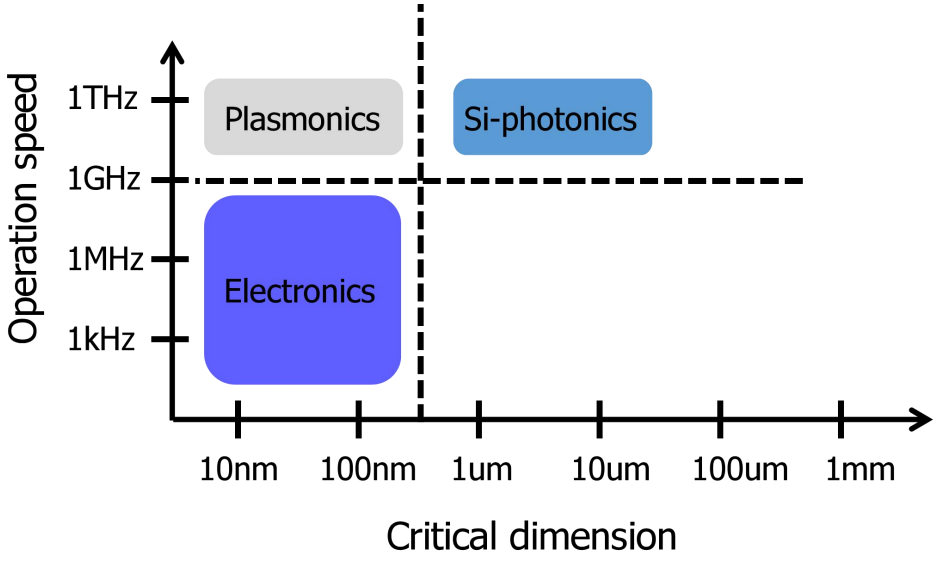

Fig. 1.3 Comparison of each carrier in the application of information transmission

1.3 Motivation and outline

Since the technology of plasmonic is a novel technology with only developed in these recent ten years, the functionality of plasmonic components are still limited in a few fields. Meanwhile, the combination of plasmonic and silicon photonics is also necessary, for which the circuits and chips containing the above two are named hybrid photonic chips and circuits or nano-photonic circuits. Thus, the following several questions are examined in this thesis for new features.

1) The functional plasmonic circuits are developed first. As the same as silicon photonics, plasmonic photonics can finish the same function. The passive and active plasmonic photonics are investigated as well. For passive case, the wavelength multiplexers and filters [47-49] are hot research. Sensing technology based on plasmonic waveguides is another research work [50-52]. For active case, the modulator [53-55] based on plasmonic waveguides are also developed yet.

2) The interconnection between silicon and plasmonic waveguides is investigated. Since both the two waveguides can be fabricated on a silicon-on-insulator platform, the low loss interconnection is used for the connection because of the large geometry size difference of waveguides. As mentioned above, the silicon waveguides work as the transmission line and this method can also effectively avoid the employment of the high loss plasmonic waveguides.

3) The interconnection between fibers and silicon wires is investigated. The simple way to provide light source for a photonic chip or circuit is to use fibers, while arrayed-integrated semiconductor laser is another choice. Due to the large geometry size difference between fibers and silicon waveguides, a method should be employed for effective light coupling between them.

4) The waveguide crossings in silicon photonics for large scale integration is investigated. Since silicon waveguides are still designed and fabricated only in one layer. The low loss and low crosstalk waveguide crossing should be investigated.

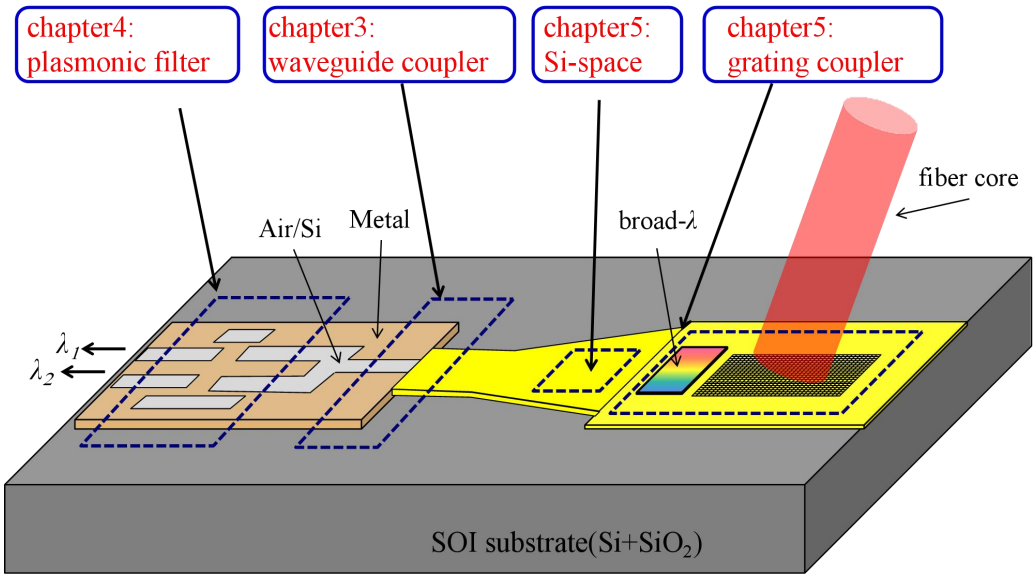

Fig. 1.4 Schematic of the hybrid PICs in the thesis

Fig. 1.4 shows the flow chart of the thesis consisting the research contents in a view of 3D dimension. The organization of this dissertation is the shown as follows. In chapter 2, the basic theories of the photonics utilizing the guided waves are introduced. It starts from the basic derivation of wave propagation equations and application in both dielectric waveguides and plasmonic waveguides. Then the numerical calculation for analyzing the mode characteristics and transmission characteristics of those waveguides are introduced. In chapter 3, a kind of functional plasmonic waveguide coupler is investigated for the effective connection between dielectric waveguides and plasmonic waveguides. The analysis starts from the basic coupler between the dielectric slab waveguides and metal-insulator-metal waveguides. In chapter 4, a kind of plasmonic filter based on side-coupled Fabry-Perot cavities is introduced, which could be used for multiplexer or demultiplexer in a wavelength-multiplexing system (WDM). The scattering matrix is established for analyzing the transmission characteristics. In chapter 5, a kind of grating coupler is introduced for the coupling between fibers and silicon wires. A kind of 2D planar meta-material is also investigated for filtering systems. The planar slab space optics utilizing curved silica mirrors for broadband waveguide crossing is also introduced.

Chapter 2 Waveguide theory and calculation methods

The waveguide theory and calculation methods are introduced in this chapter before presenting the academic results. It's necessary to introduce those knowledge since the whole thesis is based on these fundamental equations. In other words, these equations leads the design of the whole thesis.

First, the basic knowledge of wave equations and Helmholtz equations are introduced, which are based on the classical Maxwell's equations. Since the 1960s, Maxwell concluded the electro-magnetic phenomenon based on predecessor's work, especially the work from Faraday and Gaussian into a series of equations. The essence of optical waves is solved perfectly expect for the absorption and emission of photons, which are not included in the thesis. The waves equations and Helmholtz equations represent the optical waves in the infinite boundary medias, including the uniform and nonuniform medias. The slab waveguides are the special case for wave equations in finite area with boundary conditions. The wave equations satisfy the special boundary conditions, known as modes, are introduced. The mathematical calculation of the spatial and transmission characteristics of mode are then introduced. The above mentioned slab waveguides are fabricated with low loss dielectric materials, while the metal could also be used to form the waveguides. The plasmonic waveguides own superiority than traditional dielectric waveguides, especially for the ability of confining optical fields in the nano-meter range. The optical characteristics of metal and surface plasmon polaritons are then introduced.

Second, the numerical calculation methods for calculation of modes and transmission of waves are introduced, which are the basic tools of this thesis. The modes' characteristics of devices are usually analyzed by the finite-difference frequency domain (FDFD) method and the finite element method (FEM). While, in this thesis, only FEM method is applied. The transmission characteristics of devices

are analyzed by the beam propagation method (BPM) and finite-difference time-domain method (FDTD). Finally, a conclusion is obtained based on the chapter.

2.1 Waveguide theory

2.1.1 Waves equations and Helmholtz equation

The electronic magnetic theories of Maxwell's equations are first introduced in this sub-chapter. The macroscopic of electromagnetic phenomenon are described by the electric field **E**, the magnetic fields **B**, the strength of magnetic fields **H** and the electric displacement fields **D** in the following four equations:

$$\nabla \times \mathbf{H} = \mathbf{J} + \frac{\partial \mathbf{D}}{\partial t} \tag{2.1-1}$$

$$\nabla \times \mathbf{E} = -\frac{\partial \mathbf{B}}{\partial t} \tag{2.1-2}$$

$$\nabla \cdot \mathbf{B} = 0 \tag{2.1-3}$$

$$\nabla \cdot \mathbf{D} = \rho \tag{2.1-4}$$

where **J** is the current density vector and ρ is the charge density. The constitutive relationship of **D**, **B** and **E**, **H** are given by the following equations：

$$\mathbf{J} = \sigma \mathbf{E} \tag{2.2-1}$$

$$\mathbf{D} = \varepsilon_0 \mathbf{E} + \mathbf{P} \tag{2.2-1}$$

$$\mathbf{B} = \mu_0 \mathbf{H} + \mathbf{M} \tag{2.2-2}$$

where **P** is the media polarization density vector, **M** is the magnetization vector, σ is the media conductivity, ε_0 and μ_0 are dielectric permittivity and magnetic permeability, respectively.

The electric polarization density **P** could be represent in a tensor as a function of the dielectric permittivity, which represents the nonlinear characteristics of the optical media or the propagation of optical waves in nonlinear media. Since the whole thesis only discusses the linear situation, thus, usually the dielectric permittivity of media ε_0 is treated as a constant number and the polarization density **P** is not taken into considerable. The dielectric material owns the permittivity with only real number;

while, the metal material owns the permittivity with both real parts and imaginary parts, which will be discussed in the later chapter.

The above Maxwell's equations represent the electromagnetic field in infinite media with ε_0 and μ_0 are continuous numbers. While, in the case of ε_0 and μ_0 are not continuous numbers, the Maxwell's equations are not suitable and the following boundary equations should be applied for solving the fields on the boundary of two medias, which are shown in the Eqs. (2.3):

$$\mathbf{n} \cdot (\mathbf{B_1} - \mathbf{B_2}) = 0 \tag{2.3-1}$$

$$\mathbf{n} \cdot (\mathbf{D_1} - \mathbf{D_2}) = 0 \tag{2.3-2}$$

$$\mathbf{n} \times (\mathbf{H_1} - \mathbf{H_2}) = 0 \tag{2.3-3}$$

$$\mathbf{n} \times (\mathbf{E_1} - \mathbf{E_2}) = 0 \tag{2.3-4}$$

where **n** is the unite vector of normal direction on the boundary.

In a good conductivity, where **J** = 0 and **p** = 0, if the media gives the same optical characteristics in all directions and be uniform in everywhere, thus the tensor ε_0 will become a constant number. Under these conditions, the following two equations are got and named as 'passive' wave equations:

$$\nabla^2 \mathbf{E} - \frac{n_2}{c^2} \frac{\partial^2 \mathbf{E}}{\partial t^2} = 0 \tag{2.4-1}$$

$$\nabla^2 \mathbf{H} - \frac{n_2}{c^2} \frac{\partial^2 \mathbf{H}}{\partial t^2} = 0 \tag{2.4-2}$$

In the frequency domain, all the field components are oscillated at a specific angular frequency ω. Then, the wave equations, also known as the Helmholtz equations can be written in the following two equations:

$$\nabla^2 \mathbf{E} + k^2 \mathbf{E} = 0 \tag{2.5-1}$$

$$\nabla^2 \mathbf{H} + k^2 \mathbf{H} = 0 \tag{2.5-2}$$

where k is the wave vector in medium and $k = \omega^2 \varepsilon \mu$. In the following analysis of the guided optics, the Eqs. (2.4) and (2.5) form the basic equations of the rules of the

propagation of optical waves.

2.1.2 The dielectric slab waveguides

The example of a two dimensional dielectric slab waveguide is shown in the Fig. 2.1, which consists of three uniform layers. The refractive index of each layers are n_1, n_2 and n_3, which satisfy $n_1 > n_2$ and n_3 for satisfying the total internal reflection (TIR) of light. The theory of geometric ray optics are not introduced here, instead, the propagation characteristics of waves from Maxwell's equation are used.

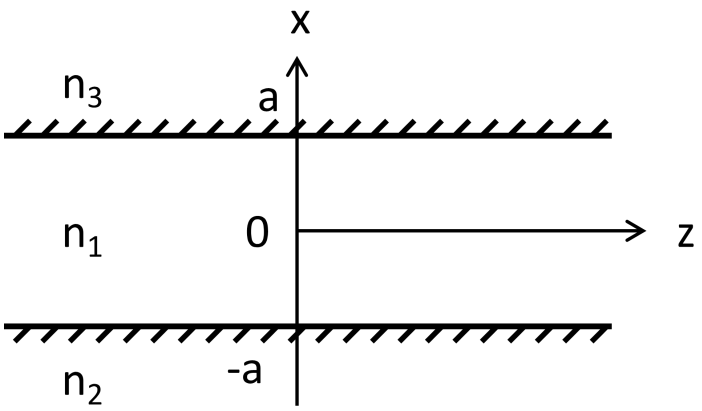

Fig. 2.1 Schematic of a 2D slab waveguide

For sinusoidal electromagnetic field with angular frequency of ω, the first and second equations of Maxwell's equations are

$$\nabla \times \mathbf{H} = j\omega\varepsilon\mathbf{E} \tag{2.6-1}$$

$$\nabla \times \mathbf{E} = j\omega\varepsilon\mathbf{H} \tag{2.6-2}$$

where **E** and **H** can be represented by the following two equations:

$$\mathbf{E} = E(x,y)e^{(i\omega t - i\beta z)} \tag{2.7-1}$$

$$\mathbf{H} = H(x,y)e^{(i\omega t - i\beta z)} \tag{2.7-2}$$

In a Cartesian coordinate system, the above two vector equations can be written in scalar forms, which are:

$$\frac{\partial \mathrm{H}_z}{\partial y} - \frac{\partial H_y}{\partial z} = j\omega\varepsilon E_x \tag{2.8-1}$$

$$\frac{\partial \mathrm{H}_{\mathrm{x}}}{\partial z} - \frac{\partial H_z}{\partial x} = j\omega\varepsilon E_y \tag{2.8-2}$$

$$\frac{\partial \mathrm{H}_{y}}{\partial x} - \frac{\partial H_x}{\partial y} = j\omega\varepsilon E_z \tag{2.8-3}$$

$$\frac{\partial \mathrm{E}_{z}}{\partial y} - \frac{\partial E_y}{\partial z} = j\omega\mu H_x \tag{2.8-4}$$

$$\frac{\partial \mathrm{E}_{x}}{\partial z} - \frac{\partial E_z}{\partial z} = j\omega\mu H_y \tag{2.8-5}$$

$$\frac{\partial \mathrm{E}_{\mathrm{y}}}{\partial x} - \frac{\partial E_x}{\partial y} = j\omega\mu H_z \tag{2.8-6}$$

Since the waveguide structure is infinite along the y direction and contacting with Eqs. (2.7), then the following two equations are got:

$$\frac{\partial \Psi}{\partial \mathrm{y}} = 0 \tag{2.9-1}$$

$$\frac{\partial \Psi}{\partial \mathrm{z}} = -j\beta\Psi \tag{2.9-2}$$

where the symbol of Ψ represents either **E** or **H** components.

Substituting the Eqs. (2.9) into (2.8), the following two groups of equations can be got:

$$\beta E_y = -\omega\mu H_x \tag{2.10-1a}$$

$$\frac{\partial \mathrm{E}_{\mathrm{y}}}{\partial \mathrm{x}} = -j\omega\mu H_z \tag{2.10-1b}$$

$$j\beta H_x + \frac{\partial H_z}{\partial x} = -j\omega\varepsilon E_y \tag{2.10-1c}$$

$$\beta \mathrm{H}_{y} = \omega\varepsilon E_x \tag{2.10-2a}$$

$$\frac{\partial \mathrm{H}_{\mathrm{y}}}{\partial \mathrm{x}} = j\omega\varepsilon E_z \tag{2.10-2b}$$

$$j\beta \mathrm{E}_{x} + \frac{\partial E_z}{\partial x} = j\omega\mu H_y \tag{2.10-2c}$$

In Eqs. (2.10-1), the three equations only contain the field components of E_y, H_x and H_z; meanwhile, the electric field is perpendicular to the propagation direction of waves, which is so called the transverse-electric (TE) mode (or waves) along the z direction. In Eqs. (2.10-2), the three equations only contain the field components of

H_y, E_x and E_z; meanwhile, the direction of magnetic field is perpendicular to the propagation direction of waves, which is called the transverse-magnetic (TM) mode (or waves) along the z direction. The characteristics of modes are then discussed below.

The characteristics of modes of TE polarization are introduced firstly. By derivativing from the Eq. (2.10-1b) and substituting the other two equations in it, the following wave equation is got:

$$\frac{\partial^2 E_y}{dx^2} + (k_0^2 n^2 - \beta^2) E_y = 0 \tag{2.11}$$

where $k_0 = \omega^2\varepsilon^2\mu^2$ and $n^2 = \varepsilon$. The refractive index n of the three layers, which composite the waveguide structure, are n_1, n_2 and n_3 and satisfying $n_1 > n_2$ and n_3 for allowing the power of waves mainly concentrated in the central core layer. The solution of Eq. (2.11) in three layers can then be written in the following three equations:

$$E_{1y} = E_1 \cos(k_x x - \phi) e^{-j\beta z}, |x| \le a \tag{2.12-1}$$

$$E_{2y} = E_2 e^{a_2(x+a)} e^{-j\beta z}, x \le -a \tag{2.12-2}$$

$$E_{3y} = E_3 e^{-a_3(x-a)} e^{-j\beta z}, x \ge a \tag{2.12-3}$$

where k_x, a_2, a_3 and β are the characteristics constants and E_1, E_2 and E_3 are the integral constants. k_x represents the phase constant of field in the core region along the x direction, while a_2 and a_3 represent the decay constant of field in the cladding and substrate layer along the x direction. The Eqs. (2.12) represent the power of field in the core region forming the distribution of standing waves along x direction, while ϕ represents the location of anti-nodes and wave festival of the standing waves, and k_x represents the distance between two wave festivals. The power at the cladding and substrate regions decay fast and are determined by the values of a_2 and a_3. The following texts represent the guided modes.

Compared with Eqs. (2.11) and (2.12), it's easy to get the following relations of k_x, a_2, a_3, β and n_1, n_2, n_3, which are:

$$k_x^2 + \beta^2 = k_0^2 n_1^2 \tag{2.13-1}$$

$$-a_2^2 + \beta^2 = k_0^2 n_2^2 \tag{2.13-2}$$

$$-a_3^2 + \beta^2 = k_0^2 n_3^2 \tag{2.13-3}$$

Substituting Eqs. (2.13) into (2.10), the three magnetic field of the three layers are got:

$$H_{1x} = -\frac{\beta}{\omega u_0} E_{1y} \tag{2.14-1}$$

$$H_{2x} = -\frac{\beta}{\omega u_0} E_{2y} \tag{2.14-2}$$

$$H_{3x} = -\frac{\beta}{\omega u_0} E_{3y} \tag{2.14-3}$$

and

$$H_{1z} = \frac{k_x x}{j\omega u_0} E_{1y} \tag{2.14-4}$$

$$H_{2z} = -\frac{a_2}{j\omega u_0} E_{2y} \tag{2.14-5}$$

$$H_{3z} = -\frac{a_3}{j\omega u_0} E_{3y} \tag{2.14-6}$$

where E_{1y}, E_{2y} and E_{3y} are determined by the boundary conditions and source excitation.

The boundary conditions determine tangential component of electric field (and magnetic field) on the boundary are the same, which are the following two conditions:

In $x = -a$ plane:

$$\mathrm{E}_{1y} = \mathrm{E}_{2y}; H_{1z} = H_{2z} \tag{2.15-1}$$

In $x = a$ plane:

$$\mathrm{E}_{1y} = \mathrm{E}_{3y}; H_{1z} = H_{3z} \tag{2.15-2}$$

According to the boundary conditions and Eqs. (2.14) and (2.15), the following two equations can be got by eliminating E_1, E_2 and E_3:

$$k_x \tan(k_x a + \phi) = a_2 \tag{2.16-1}$$

$$k_x \tan(k_x a - \phi) = a_3 \tag{2.16-2}$$

The Eqs. (2.16) can then be expressed by another type:

$$k_x a + \phi = \tan^{-1} \frac{a_2}{k_x} + p\pi \tag{2.17-1}$$

$$k_x a - \phi = \tan^{-1} \frac{a_3}{k_x} + q\pi \tag{2.17-2}$$

where p and q are arbitrary integral numbers.

The equations of k_x and ϕ are then got according to Eqs. (2.17) and shown as the follows:

$$k_x d = \tan -1 \frac{a2}{k_x} + \tan -1 \frac{a3}{k_x} + m\pi \tag{2.18-1}$$

$$\phi = \frac{1}{2} \tan \text{-} 1 \frac{a2}{k_x} - \frac{1}{2} \tan -1 \frac{a3}{k_x} + \frac{n\pi}{2} \tag{2.18-2}$$

where $d = 2a$ is the thickness of the slab waveguide, $m = p+q = 0,1,2...$ and $n = p-q = -2,-1,0,1...$ It's clear that $n = 0$ and 1 contain the whole situation. Then when $m = p+q$ is an even number, the field of E_y displays a cosine function in the core region along the x direction; while, when $m = p+q$ is an odd number, the field of E_y displays a sinusoidal function in the core region along the x direction. According to the basic analysis, the field in the core region can then be written in the following two equations:

$$E_{1y} = E_1 \cos(k_x x - \phi) e^{-j\beta z} \tag{2.19-1}$$

$$E_{1y} = E_1 \sin(k_x x - \phi) e^{-j\beta z} \tag{2.19-2}$$

where $\phi = \frac{1}{2} \tan^{-1} \frac{a_2}{k_x} - \frac{1}{2} \tan^{-1} \frac{a_3}{k_x}$ and Eq. (2.19-1) and (2.19-2) equal m is even number and odd number, respectively.

The Eqs. (2.18) are then called a series of electromagnetic waves along the z

direction, i.e. the transverse electric mode, and marked by TE_m.

The transverse magnetic mode can also be derived by the following methods. The characteristics equations of TM mode are expressed in the following two equations:

$$k_x d = \tan^{-1} \frac{a_2 {n_1}^2}{k^x {n_2}^2} + \tan^{-1} \frac{a_3 {n_1}^2}{k_x {n_3}^2} + m\pi \tag{2.20-1}$$

$$\phi = \frac{1}{2} \tan^{-1} \frac{a_2 n_1^2}{k_x n_2^2} - \frac{1}{2} \tan^{-1} \frac{a_3 n_1^2}{k_x n_2^2} \tag{2.20-2}$$

where m is the same definition used above and a series of electromagnetic fields satisfying the Eqs. (2.20) are the called the transverse magnetic mode and marked by TM_m.

2.1.3 Surface plasmon polaritons and plasmonic waveguides

The introduction of surface plasmon polaritons and plasmonic waveguides are shown in this chapter. As it's widely known that metal is a good conductor and has a high electrical conductivity. So it's necessary to consider the influence of electrical conductivity and the optical properties of metal. According to the same procedure discussed in the sub-chapter 2.1.1, the wave equation of electric field can be got in the following equation when considering the electrical conductivity σ:

$$\nabla^2 \mathbf{E} = u_0 \sigma \frac{\partial \mathbf{E}}{\partial t} + \varepsilon_0 u_0 \varepsilon \frac{\partial^2 \mathbf{E}}{\partial t^2} \tag{2.21}$$

For a electromagnetic waves with a frequency of ω, $\mathbf{E} = \mathbf{E}_0 e^{(-i\omega t)}$, the equation of (2.21) can be transformed by

$$\nabla^2 \mathbf{E} + \hat{k}^2 \mathbf{E} = 0 \tag{2.22-1}$$

$$\hat{k}^2 = \frac{\omega^2}{c^2} (\varepsilon + i \frac{\sigma}{\omega \varepsilon_0}) \tag{2.22-2}$$

A new parameter of complex dielectric constant $\hat{\varepsilon}$ is then defined according to Eq. (2.22-1), which is shown as follows:

$$\hat{\varepsilon} = \varepsilon + i\frac{\sigma}{\omega\varepsilon_0} \tag{2.23}$$

The Eq. (2.22) is then the same form as used in the Helmholtz equation as introduced before, while the dielectric constant is a complex number. The propagation of waves in a conductive medium is then the same as in the dielectric medium, where the dielectric constant is a complex number and a real number in a conductive medium and in a dielectric medium, respectively.

The above analysis lead to the specially optical characteristics of the metal, which makes the surface plasmon waves propagating on the boundary of metal and dielectric medium. This kind of surface wave has different optical properties. The existing conditions of surface waves are discussed here. Fig 2.2 shows a simple boundary of two kinds of semi-infinite, isotropic medium. Assume that the surface waves propagates along the z direction and $x > 0$ is the medium 1 with a dielectric constant of $\varepsilon_1(\omega)$; $x < 0$ is the medium 2 with a dielectric constant of $\varepsilon_2(\omega)$. Both two mediums have the same magnetic permeability $\mu = \mu_0 = \mu_1$.

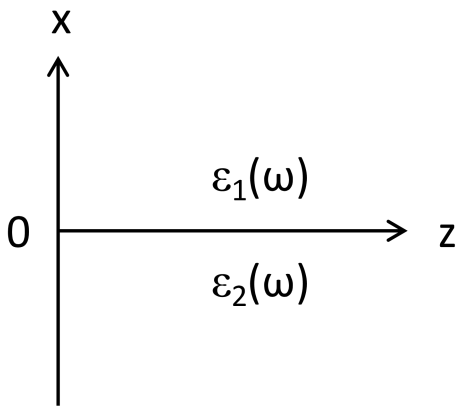

Fig. 2.2 Schematic of a boundary of dielectric and metal materials for the propagation of SPP waves

According to the Maxwell's equation and eliminating the magnetic field vector, the following three equations can be got:

$$\nabla \times \mathbf{E} = -\frac{\partial \mathbf{B}}{\partial t} \tag{2.24-1}$$

$$\nabla \times \mathbf{H} = \frac{\partial \mathbf{D}}{\partial \mathrm{t}} \tag{2.24-2}$$

$$\nabla \times (\nabla \times \mathbf{E}) + \mu_0 \frac{\partial^2 \mathbf{D}}{\partial \mathrm{t}^2} \tag{2.24-3}$$

According to the results of the surface waves, which are confined on the boundary and decay along the *x* direction, the solution could be:

$$\mathbf{E}_1(\mathbf{r},t) = \mathbf{E}_1^0 e^{-a_1 x} e^{i\beta z - i\omega t}, x > 0 \tag{2.25-1}$$

$$\mathbf{E}_2(\mathbf{r},t) = \mathbf{E}_1^0 e^{a_2 x} e^{i\beta z - i\omega t}, x > 0 \tag{2.25-2}$$

Subsisting the Eqs. (2.25) into 2.24-3, the following two equation can be got:

$$E_1(x) = (\frac{i\beta}{a_1} E_{1x}^0, E_{1y}^0, E_{1z}^0) e^{-a_1 x}, x > 0 \tag{2.26-1}$$

$$E_2(x) = (-\frac{i\beta}{a_2} E_{2x}^0, E_{2y}^0, E_{2z}^0) e^{a_2 x}, x < 0 \tag{2.26-2}$$

where a_1 and a_2 satisfy:

$$a_1^2 = \beta^2 - k_0^2 \varepsilon_1 \tag{2.27-1}$$

$$a_2^2 = \beta^2 - k_0^2 \varepsilon_2 \tag{2.27-2}$$

The magnetic field can also be got by the same way, which is not shown here. Then according to the boundary condition, it's clear to get the following conditions:

$$E_{1y}^0 = E_{2y}^0 \tag{2.28-1}$$

$$E_{1z}^0 = E_{2z}^0 \tag{2.28-2}$$

$$\frac{\varepsilon_1}{a_1} E_{1y}^0 = -\frac{\varepsilon_2}{a_2} E_{2y}^0 \tag{2.28-3}$$

$$a_1 E_{1y}^0 = -a_2 E_{2y}^0 \tag{2.28-4}$$

Since a_1 and a_2 are both real numbers, according to Eq. (2.28-3, -4),

$$\mathrm{E}_{1y}^0 = E_{2y}^0 = 0 \tag{2.29}$$

Eq. (2.29) means the surface plasmon waves are transverse-magnetic (TM) waves. Then according to equations (2.28-1, -2), it's clear known that

$$\frac{a_1}{a_2} = -\frac{\varepsilon_1}{\varepsilon_2} \tag{2.30}$$

Eq. (2.30) means the surface plasmon waves only exist at the condition of the inverse dielectric constants of the boundary. Then according to Eqs. (2.27) and (2.30), the effective refractive index n_{eff} of a surface plasmon waves can be written as :

$$n_{eff} = \frac{\beta}{k_0} = \sqrt{\frac{\varepsilon_1 \varepsilon_2}{\varepsilon_1 + \varepsilon_2}} \tag{2.31}$$

It's clear seen that the n_{eff} is a complex number, which refers the propagation loss on the boundary of the metal and dielectric materials.

2.2 Numerical analysis methods for mode characteristics

In this chapter, the method for solving waveguide mode by finite element method (FEM) is introduced.

2.2.1 Finite Element method

The Finite Element Method (FEM) method is generally superior in the calculation of complex geometries materials with complex index distribution. The basic theoretical background of FEM is presented here. It also should note that FEM is a full-vector implementation for the calculation of both propagating and leaky waveguide modes, also including cavity modes. The derivation of the vector wave equation with a form of free source and harmonic time representation in an arbitrary, anisotropic and lossy media is shown as the following equation [56, 57]:

$$\nabla \times (\frac{1}{\overline{s}}(\nabla \times \mathbf{E})) - k_0^2 \overline{\varepsilon_r} \mathbf{E} = 0 \tag{2.32}$$

Subject to the boundary conditions at the calculation domain edges

$$\hat{n} \times \mathbf{E} = 0 \tag{2.33}$$

In the above equations, the complex diagonal tensors, s and ε, represent the coordinate extending and the space distribution of materials, respectively. s is the identity tensor in the domain with absorption boundary, then s is represented as:

$$\bar{s} = (\frac{s_y s_z}{s_x})\hat{x}\hat{x} + (\frac{s_x s_z}{s_y})\hat{y}\hat{y} + (\frac{s_x s_y}{s_z})\hat{z}\hat{z} \tag{2.34}$$

$$s_{x,y,z} = 1 - j(\frac{a-L}{L})\delta_{\max} \tag{2.35}$$

where δ_{max} is the loss parameter, α is the distance from the boundary, and L is the thickness of this absorption layer, labeled as the perfectly matched layer (PML). The tensor elements in both the PML and the end of the calculation domain are matched to generate quite small reflections at the PML interface for arbitrary frequencies and angles of incidence, which is in Eq. (2.36). Then PML is terminated at the domain edge with a perfect electrical conductor (PEC) boundary condition [58].

$$\overline{\varepsilon_2} = \varepsilon_1 \bar{s} \tag{2.36}$$

The Finite Element Method (FEM) does not give the answers of the problem in boundary directly, but uses a variational expression, or functional, constructed from the operator of the differential Eq. (2.32). The functional along the two dimensions and over a domain A, is given by [59]

$$F(\mathbf{E}) = \iint_A [(\nabla \times \mathbf{E})^* \frac{1}{s}(\nabla \times \mathbf{E}) - k_0^2 \mathbf{E}^* \bar{\varepsilon}\mathbf{E}]dA \tag{2.37}$$

For propagation and leaky modes [60], a separable field is used, $E(x,y,z) = E(x,y)exp(-j\beta z)$, where β is the propagation constant along z. The Finite Element Method does not solve the expansion of E or H fields over the whole domain A, but instead divides the domain into several elements, which are collected with each other and defined as a basis. The final solutions are the combination of the solutions of all the elements. Finally, the basis is vanished after calculation. For transverse components on the hybrid Node/Edge, they are expanded in a vector basis,

$$\mathbf{E}_T(x,y)e^{-j\beta z} = \sum_{i=1}^{n} N_i E_{Ti} = \sum_{i=1}^{n} \{U\hat{x} + V\hat{y}\}E_{Ti} \tag{2.38}$$

where the E_{Ti} are the values of the transverse electric field at each edge or node. The geometry of the element and the order of the interpolation decide the basis dimension of the element n.

2.3 Numerical analysis methods for transmission characteristics

In this chapter, the numerical methods for solving transmission of waveguides by beam propagation method (BPM) and finite-difference time-domain method (FDTD) are introduced.

2.3.1 Beam propagation method

Beam Propagation Method (BPM) is the most widely used propagation technique for modeling integrated photonic devices and fiber optics. BPM is indeed a electro-magnetic algorithm for approximating the exact monochromatic waves under the Helmholtz' equations. [61-63] The fields of waves in a monochromatic type could be written in the following equation, where ϕ are either E or H fields:

$$\frac{\partial^2 \phi}{\partial x^2} + \frac{\partial^2 \phi}{\partial y^2} + \frac{\partial^2 \phi}{\partial z^2} + k(x,y,z)^2 \phi = 0 \tag{2.39}$$

The scalar electric field is used here and has been written as $E(x,y,z,t) = \phi(x,y,z)e^{(-j\omega t)}$ and the notation $k(x,y,z) = k_0 n(x,y,z)$ means the wavenumber in x, y and z directions, where $k_0 = 2\pi/\lambda$ is the free space wavenumber. The solution of Eq. (2.39) entirely depends on the refractive index distribution $n(x,y,z)$.

In guided-waves, the most rapid variation of the field is the phase variation due to the propagation along the waveguides, in which is predominantly along the z direction. Thus, the field ϕ could be represent in Eq. (2.40) without considering the factor of time variation.

$$\phi(x,y,z) = u(x,y,z)e^{i\bar{k}z} \tag{2.40}$$

The k-bar used here represents the average phase variation, which is referred to the reference wavenumber. By substituting Eq. (2.40) into Eq. (2.39), the slowly varied field of ϕ could be represent in the Eq. (2.41):

$$\frac{\partial^2 u}{\partial z^2} + 2i\bar{k}\frac{\partial u}{\partial z} + \frac{\partial^2 \phi}{\partial x^2} + \frac{\partial^2 \phi}{\partial y^2} + (k^2 - \bar{k}^2)u = 0 \tag{2.41}$$

It's should note that the Eq. (2.41) gives the same meaning as the exact Helmholtz equation in the previous sub-chapter of 2.1, except that this equation uses *u* to represent the field. By assuming the sufficient slow variation of the field *u* and propagation length *z*, the first term of $\partial^2 u/\partial z^2$ could be neglected with respect the other terms of Eq. (2.41). Under this condition and assumption, the Eq. (2.41) could be rearranged as：

$$\frac{\partial u}{\partial z} = \frac{i}{2\bar{k}}\left(\frac{\partial^2 u}{\partial x^2} + \frac{\partial^2 u}{\partial y^2} + (k^2 - \bar{k}^2)u\right) \tag{2.42}$$

The Eq. (2.42) represents the basic propagation equation of the beam propagation method in 3D; Simply, the 2D expression of Eq. (2.42) could be got by negelecting the dependence on the y direction, which is simplification to two dimensions (2D) is obtained by omitting any dependence on *y*, which is $\partial u/\partial y=0$. For the incidence of *u(x,y,z = 0)*, the 2D expression could be represented in Eq. (2.43) for the field in the space of $z>0$.

$$\frac{\partial u}{\partial z} = \frac{i}{2\bar{k}}\left(\frac{\partial^2 u}{\partial x^2} + (k^2 - \bar{k}^2)u\right) \tag{2.43}$$

It's should note that the following approximation gives both merits and demerits. First, the slowly varying field on the longitudinal grid (along the propagation direction of *z*) is represent by the factoring of the rapid variation of phase. This allows the this is much coarser than the wavelength, which is contributed to the fast efficiency of this method. Second, Eq. (2.42) and (2.43) are both equations with only the first derivative term by eliminating the second derivative term along the *z* direction, which contributes a single integration for solving those equations. The third, which is the most important contribution on efficiency, is the time factor is reduced to as least of the order of Nz (number of grids along the *z* direction) compared with the full vector solution of the Helmholtz equation.

However, the above benefits come accompanying with some price. The

approximation of the slowly varying field limits the consideration of fields that only propagate along the *z* axis. Meanwhile, for some devices which are sensitive to the complicated phase variation, such as multi-mode interference, the beam propagation method is not precise enough to depict the phase variation. In addition, the elimination of the second derivative gives no solution of backward propagated waves. Such devices with reflection could not be modeled accurately.

2.3.2 Finite-difference time-domain method

The finite-difference time-domain (FDTD) method is a rigorous solution of the Maxwell's equations without any approximations and theoretical restrictions. Comparing with other methods calculating the Maxwell's equations in frequency domain, such as methods of moments (MoM), the FDTD method can save much computational resources and time, since the frequency can be derived from the time-domain results after Fourier transform (FT), where the fast Fourier transform (FFT) is mostly used in the field of computational electromagnetic (CEM).

FDTD method is widely used as a propagation solution technique in integrated optics or propagation of waves in arbitrary geometries, especially in situations where the complex geometries are applied and solutions obtained through other methods such as BPM cannot associate with the complex structure geometry or are not adequate solutions. Since FDTD is a direct solution of Maxwell's curl equations, it therefore includes many more effects than other approximate methods and can provide solutions cover a wide frequency range with simple running of calculation.

Since the FDTD belongs to a general class of grid-based differential numerical calculation methods, the time-dependent Maxwell's equations are solved using central-difference approximations of the space domain and time partial derivatives. The components of electric field vector in space are solved at a given node of the space in time. Then, the magnetic fields are calculated through the Maxwell's equations.

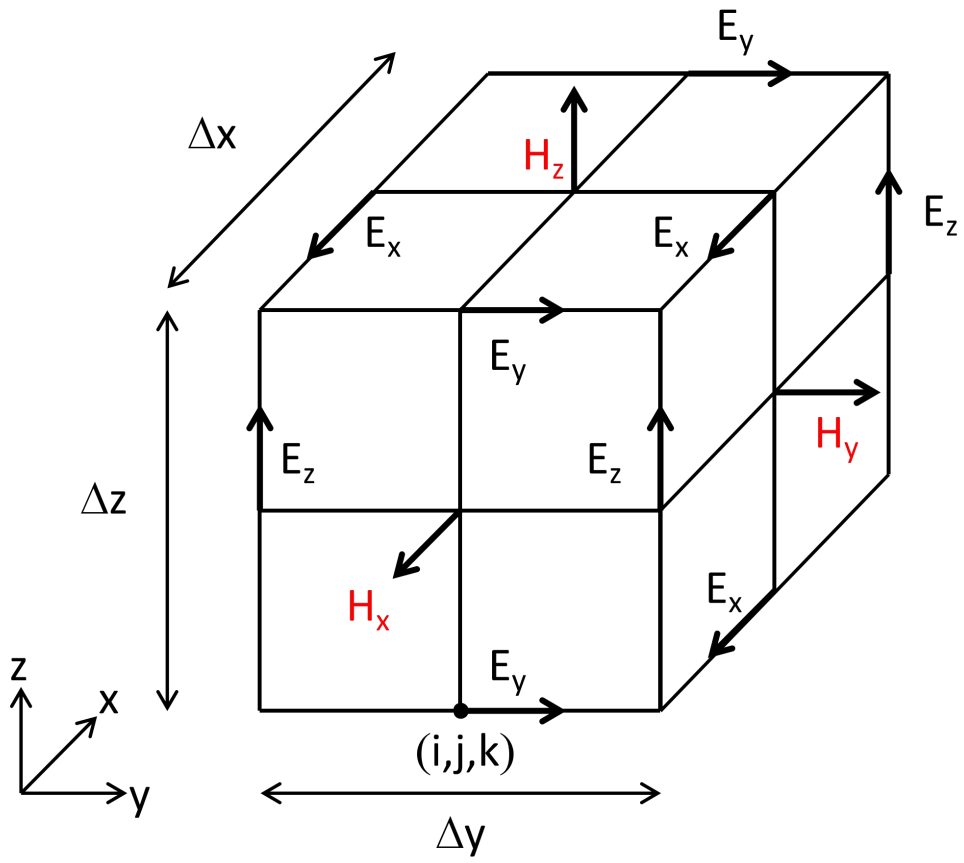

Fig. 2.3 Schematic of the mesh of Yee's FDTD algorithm

Imagine a free space without any flowing currents and isolated charges, in which Maxwell's equations can be written in six scalar equations as shown in sub-chapter of 2.1. Two examples are:

$$\frac{\partial H_x}{\partial t} = -\frac{1}{\mu}\left(\frac{\partial E_y}{\partial z} - \frac{\partial E_z}{\partial y}\right) \tag{2.46-1}$$

$$\frac{\partial E_y}{\partial t} = -\frac{1}{\varepsilon}\left(\frac{\partial H_x}{\partial z} - \frac{\partial H_z}{\partial x}\right) \tag{2.46-2}$$

The other four are symmetric equivalents of the presenting two by cyclically exchanging the subscripts of x, y and z and the derivatives, which are not shown here.

Yee presents the square mesh to solve these equations, which is the most popular method used in the world. [64-65] In his work, the computation of the E and H fields are given at points on a grid with grid space defined as Δx, Δy and Δz apart, which is shown in Fig. 2.3. The E and the H field components are calculated from each other

with the broken up of discrete time steps of Δt. The E field components are then computed at times $t = n\Delta t$ and the H fields at times $t = (n+1/2)\Delta t$, where n is an integer representing the compute step. For example, the E field at a time $t = nt_0$ is equal to the E field at $t = (n-1)\Delta t$ plus an additional term computed from the spatial variation, or curl, of the H field at time t. It should note that the space grid size should be chosen smaller enough to make sure the slowly variation of electromagnetic field or not changing significantly for calculation accuracy. This means that the chosen of space grid size must be a fraction of the wavelength.

This method results in six equations that can be used to compute the field at a given mesh point, denoted by integers i, j, k. For example, two of the six are:

$$H_{x(i,j,k)}^{n+1/2} = H_{x(i,j,k)}^{n-1/2} + \frac{\Delta t}{\mu \Delta z}(E_{y(i,j,k)}^{n} - E_{y(i,j,k-1)}^{n}) - \frac{\Delta t}{\mu \Delta y}(E_{z(i,j,k)}^{n} - E_{z(i,j-1,k)}^{n}) \qquad (2.47\text{-}1)$$

$$E_{x(i,j,k)}^{n+1} = E_{x(i,j,k)}^{n} + \frac{\Delta t}{\varepsilon \Delta y}(H_{z(i,j+1,k)}^{n+1/2} - H_{z(i,j,k)}^{n+1/2}) - \frac{\Delta t}{\varepsilon \Delta z}(H_{z(i,j,k+1)}^{n+1/2} - H_{z(i,j,k-1)}^{n+1/2}) \qquad (2.47\text{-}2)$$

These equations are literately solved in a leapfrog manner, alternating between computing the E and H fields at subsequent $\Delta t/2$ intervals. For stable computation, the time step Δt should obey the following relation of the space step:

$$\sqrt{(\Delta x)^2 + (\Delta y)^2 + (\Delta z)^2} > c\Delta t = \sqrt{\frac{1}{\varepsilon \mu}}\Delta t \qquad (2.48)$$

2.3 Summary

In summary, the basic theories of guided waves, including dielectric and plasmonic waveguides and numerical methods of mode and transmission analysis are introduced. First, the waveguide theory is introduced, including the wave equations and Helmholtz equation. The dielectric slab waveguides and plasmonic waveguides are then introduced based on the above basic knowledge. Then, the numerical analysis methods for mode characteristics, FEM, is introduced. The numerical analysis methods for waveguide transmission characteristics, BPM and FDTD are introduced. These basic equations provide foundation of the following calculation results.

Chapter 3 Plasmonic waveguide coupler

In this chapter, a type of compact, highly efficient optical coupler for dielectric slot waveguides and hybrid plasmonic waveguides based on transition layers (air slot grooves) is investigated. This part serves as the interconnection of silicon waveguides and plasmonic waveguides for I/O ports. The high efficient interconnection is desired with characteristics of broad band.

Section 3.1 introduces the basic background of the proposed waveguide coupler along with the device structure and research background. Section 3.2 discusses the transmission characteristics of the basic direct coupler. Section 3.3 discusses the matching conditions of effect mode area of two waveguides and reflectivity, which supports the highly efficient coupler design. Section 3.4 discusses the improved coupler design, for which the transmittance and reflectivity are improved. Besides, the effect of the funnel effect is also discussed. Section 3.5 gives the summary of the research work.

3.1 Research background and device structure

In recent years, research on high-density photonic (optical) integrated circuits (PICs) has attracted much interest. Optical waveguides, which serves as channels for the transmission of optical signals, in such circuits could be simply classified into two types according to their functions. One set of them is a simple wiring waveguide and is generally composed of a wire of Si or other materials with high refractive index contrast. The other set is a functional waveguide, such as the slot or plasmonic waveguide. Both of them play fundamental roles in the composition of various functional sections of PICs with their ability to concentrate and confine intense fields at sub-wavelength scales.

Plasmonic waveguides, in which modes are formed by the effect of surface plasmon polaritons (SPPs) on the metal/dielectric interface, can achieve

nanometre-scale field confinement than traditional silicon wire [43, 66]. Various type of devices utilizing the superior characteristic have been proposed [67–72]. For the core/clad geometry, plasmonic waveguides are divided into different types, including metal-insulator-metal (MIM) and metal-dielectric-metal (MDM) [67–69] structures, as well as hybrid plasmonic structures, which give better performance than MIM and MDM plasmonic waveguides [70–72]. The simple review of SPPs mode in plasmonic waveguide is given here, as the basic theory of the plasmonic waveguide was introduced in chapter 2. In the first two structures, MIM and MDM type, the waveguide is established by sandwiching a dielectric or air material as a core by a pair of metal materials. SPPs are induced on both sides of the dielectric core layer and confined in the central dielectric medium. Conversely, in the hybrid plasmonic waveguides (HP-WGs), another high index contrast dielectric material is inserted in the central of the first core region, which has slightly low refractive index. Thus, part of the mode field is more confined in the central dielectric than the simple MIM or MDM plasmonic waveguides, which helps to reduce the propagation loss slightly. Based on these characteristics, HP-WGs have been found many potential applications [73–77]. However, due to the basic guiding mechanism, the plasmonic waveguides cannot avoid from the large propagation losses, which is compared to the conventional dielectric waveguides. Thus, plasmonic waveguides are usually studied as a core functional part of integrated circuits.

Dielectric slot waveguides (DS-WGs) are another functional waveguide that can achieve sub-wavelength field confinement and relatively low propagation loss. The large index difference between the core and cladding leads to a large discontinuity of electric field. A large amount of basic theoretical research [78–81] and application proposals [82, 83] have been reported and established. Because of the low propagation loss, DS-WGs can be used both as a simple connection part and functional part. In addition, the coupling to the Si wire is easier than plasmonic waveguides. Based on the above background, in future complex integrated circuits, a situation where plasmonic and slot waveguides are used together to fully make use of the individual characteristics could be imagined. In such circuits, it is important to

achieve an efficient coupling between the slot and plasmonic waveguides.

To date, the highly efficiency couplers between Si waveguide and MIM waveguide have been widely reported and experimental certificated [84-87]. The adiabatic nano-focusing taper between two waveguides functions as a mode converter to achieve smoothly mode conversion from Si waveguide to MIM waveguide, as the two modes are much similar. However, firstly, the taper length is still a neglected factor which greatly influence the coupling efficiency (e.g. 600 nm taper length in [85]); secondly, to our knowledge, the coupling between two waveguides with large mode difference (e.g. DS-WG and HP-WG) has not been clarified, yet. Thus, to design a taper between these waveguides is difficult, and other coupling mechanism need to be investigated.

In this chapter, the coupling characteristics between DS-WGs and HP-WGs through 2D electromagnetic simulations are investigated. For the simply evaluation of slot to slot coupling, without considering the mode conversion, the 2D simulation has been proved more time efficiency and mature research methods in [88,89]. First, the performance of the direct connection without the coupler structure was studied. Then, the 50 nm transition coupler structures were studied. The basic concept of the structure is the insertion of air grooves into the waveguide interface as a transition region. In the design of actual structure, it's referred to previous research [88] on the direct coupling characteristics between slot and MDM waveguides.

The materials of Si and Ag are selected, as the dielectric and metallic materials, with dielectric constants of 12.38 + i0 and –103.71 + i8.23 at wavelength of 1550nm, respectively [68]. From the material constant point of view, Ag is one of the most advantageous and common material. Therefore, many of former theoretical research used Ag [68, 69], instead of practical useful materials, such as Au and Cu [85, 86]. For both types of waveguides, a fundamental TM mode was assumed, which had been confirmed as a better choice in 2D simulation [82, 87]. Furthermore, the computational domain of a uniform orthogonal 2D mesh was used. The ends of the domain were terminated by perfectly matched layers (PMLs). The grid size was set to 1nm for both directions. The transmittance is defined as the ratio of transmitted power

and launched power, similar to reflectivity. The metal absorption loss and waveguide propagation loss are also reduced in both calculated transmittance and reflectivity for higher accuracy.

3.2 Transmission characteristics of the direct coupler

A schematic of the 3D and 2D DS-WG studied here is shown in Fig. 3.1(a) and (b), respectively. The central air gap (n_L = 1) of width d_L serves as a core and is sandwiched by a pair of symmetric Si cladding (n_H = 3.52) of width d_H. The space outside the Si is filled with air. The structure extends infinitely toward the y and z directions. Guided modes are assumed to propagate along the z direction. The field profile of the fundamental TM mode, composed of E_x, E_z and H_y components, for d_H = 200 nm and d_L = 50 nm is presented in Fig. 3.1 (c) (E_x distribution). The profile has a flat-top single rectangular peak near the centre. In addition, in the Si and air claddings, there is non-negligible amplitude, which is approximately 1/5–1/6th of the peak.

It's clear known that from the above analysis, the field is enhanced and mainly confined in the central air slot region. However, it also should note that the power in the central air slot are not so high. That comes from the nano-meter range. The total power come from the integral of intensity in the central region. The small region limits the amount of power.

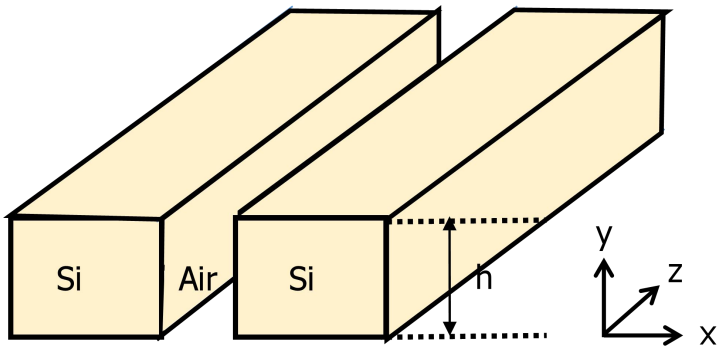

a

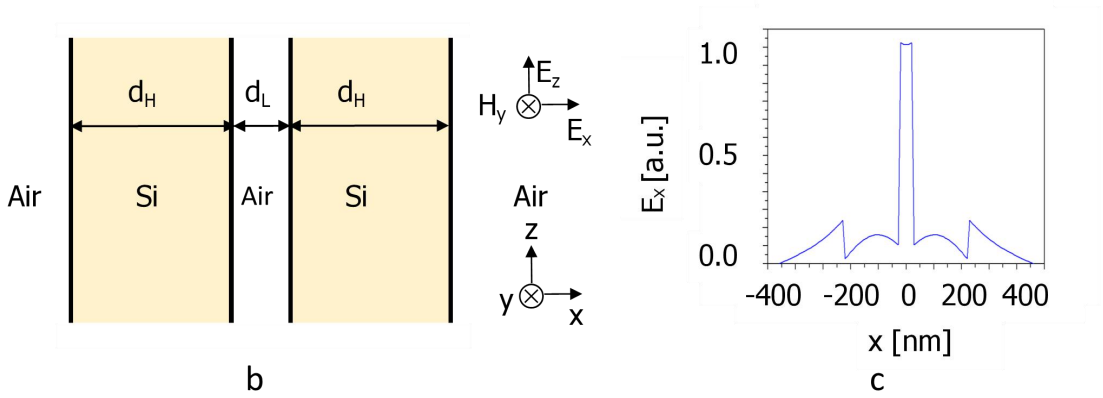

Fig. 3.1 Schematic of (a) 3D and (b) 2D structure of the dielectric slot waveguide; and (c) the E_x components for h = ∞ for TM polarization.

A schematic of an example of 3D and 2D HP-WG studied here is shown in Fig. 2(a) and (b), respectively. The Si centre core (width: d_S) is embedded in the air gap between a pair of Ag claddings. The Ag claddings were assumed to semi-infinitely extend toward the outside of the waveguide. The spacing between the Ag and Si is denoted by d_R. It's used d_S = 200 nm and d_R = 50 nm. The calculated field distribution of E_x is shown in Fig. 3.2 (c). This mode exhibits double peaks at the air regions. In addition, the field amplitude almost decreases to zero in the Ag claddings and the amplitude of the central Si core is approximately 1/7 of the peak amplitude.

In the parameters of the d_S and d_R, those two parameters represent different meanings in the trade-off of propagation length and field confinement ability. It's clear known that the propagation of hybrid of modes contain the silicon mode as well as the surface plasmon mode at the two metal/dielectric interfaces. For a large d_S, the silicon mode will occupy the main position, which implies the longer propagation length and low field confinement in two air slots. For a smaller d_S, the surface plasmon mode occupy the main position (silicon mode vanishes for d_S = 0) and a shorter propagation length is predicted as well as high field confinement ability. The trade-off of the propagation length and field confinement has been analyzed in other hybrid plasmonic waveguides, which would not be discussed in the thesis.

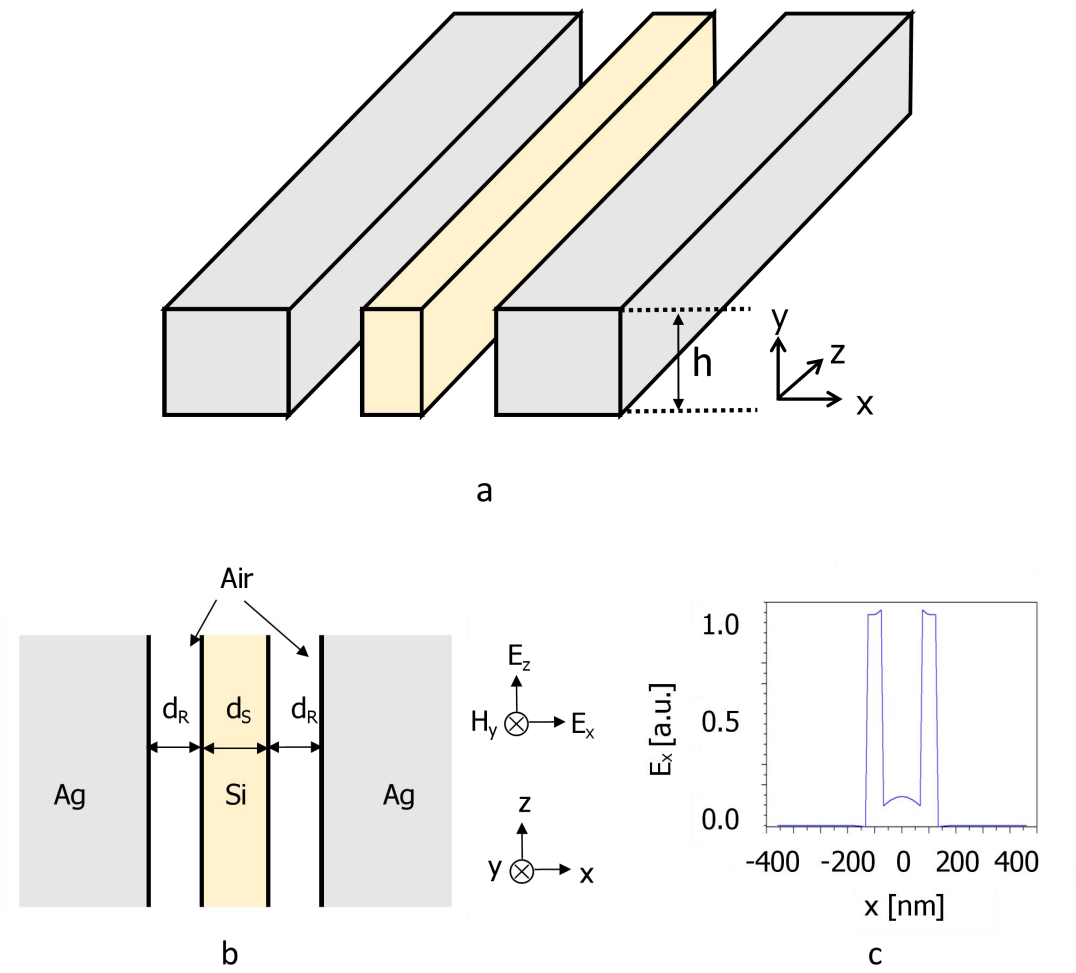

Fig. 3.2 Schematic of (a) a 2D hybrid plasmonic waveguide and (c) the E_x components

The above results regarding the basic mode profiles imply that it will be crucial to the structure design to determine how to couple the main peak and the side lobes of the DS-WG to the double peaks of the HP-WG.

First, the direct connecting performance of a DS-WG and HP-WG is studied. Fig. 3.3 shows a schematic of the analyzed junction. The structural parameters of the HP-WG were set to d_R = 50 nm and d_S = 200 nm, which are the typical values used in some of the literature [72, 77]. The transmission and reflection characteristics are calculated by changing the parameters of the slot waveguide (d_H and d_L). The fundamental mode of the DS-WG was launched from the bottom of the figure, and the Poynting vector (discussed later) was measured in the dotted square.

Fig. 3.4 (a) shows the transmitted mode power of the HP-WG as a function of d_H and d_L (width of Si and air gap of DS-WG, respectively). Fig. 3.4 (b) shows the power of the reflected mode at the DS-WG. The remaining input power was lost through radiation. The variation of transmission efficiency and reflectivity is relatively small when d_H less than 200 nm; however, they both vary rapidly above d_H larger than 200 nm. The maximum transmission (~75%) is achieved at their boundary: $d_H \sim 200$ nm. In addition, a larger d_L results in a smaller transmittance and larger reflection. To understand the transmission peak and reflection minima at $d_H \sim 200$ nm, the following explanation was considered.

For the tunable parameters of d_S and d_R, the results are not shown in graph but simple discussed here. For the same fixed value of d_R, a larger d_S represents the coupling from silicon slot mode to silicon mode become dominant. Since the two modes used in the thesis are both the lowest propagation mode, the coupling efficiency would graduate increased with the increasing of d_S. However, as it was mentioned in the previous chapter, a larger d_S represented a lower field confinement ability. Thus, another silicon taper should be applied to decrease the width of the central silicon waveguide, which would bring extra cost.

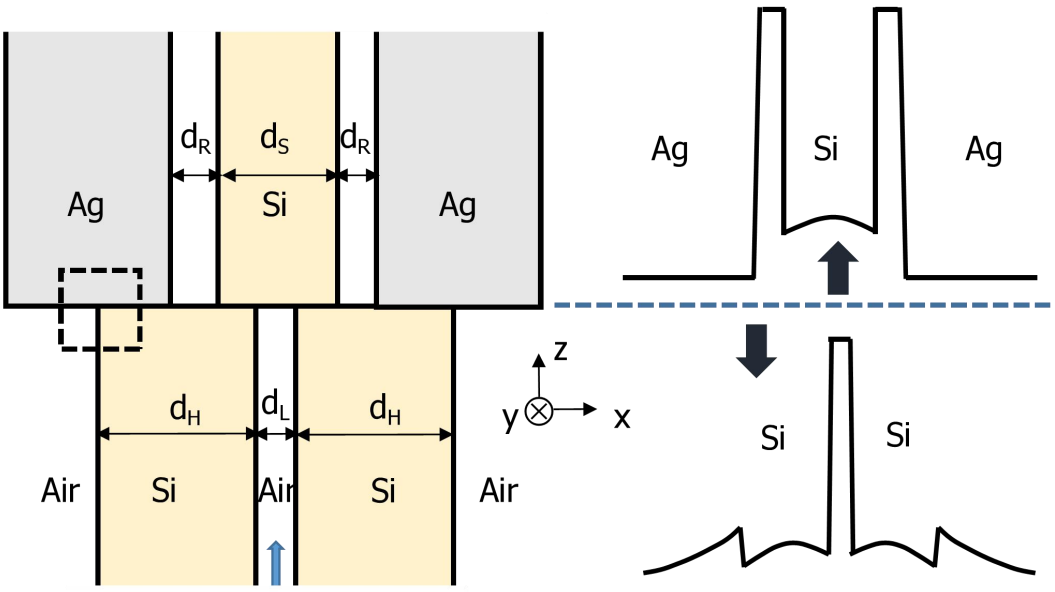

Fig. 3.3 Schematic the direct coupler of the DS-WG and the HP-WG, where the dashed black block refers the calculation region of the Poynting vector in the sub-chapter 3.4.2. The right inserted figures shows the mode coupling from the single slot to double slots.

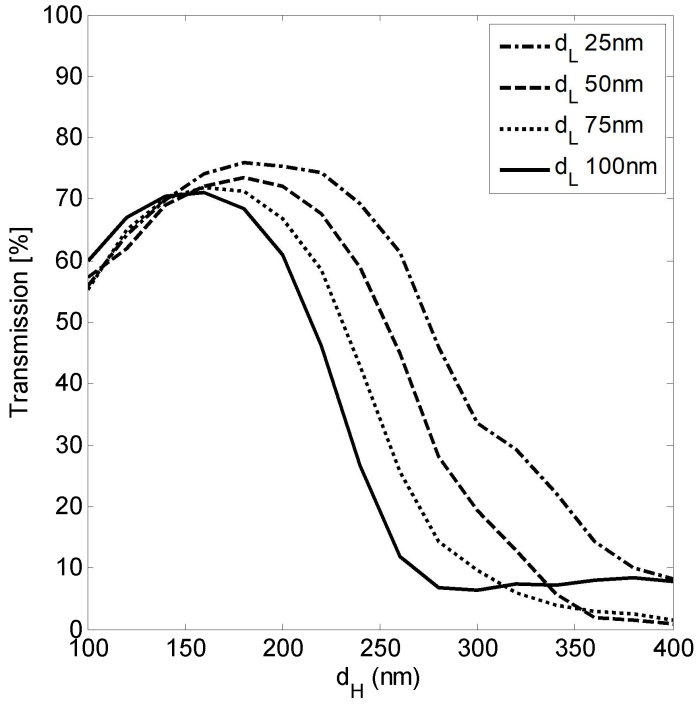

a

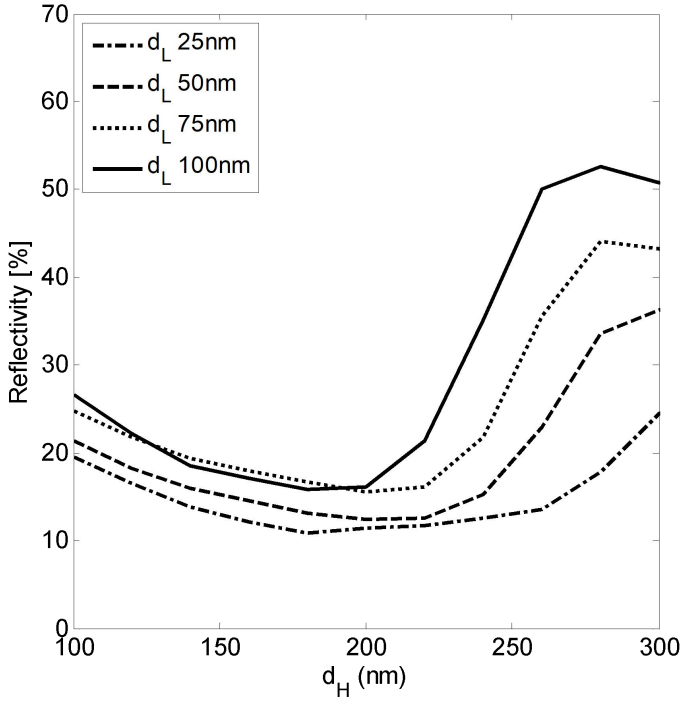

b

Fig. 3.4 Calculation results of the (a) transmittance and (b) reflectivity in Fig. 3.3.

3.3 Matching conditions

3.3.1 Effective mode area matching

The mechanism of the transmittance peak at d_H = 200 nm is explained in view of the effective mode area (W_{eff}) of each waveguide. Note that this d_H also yielded the minimal radiation loss. It's assumed that if the W_{eff} of the two waveguides were of the same order, the coupling performance would be improved. It's varied the structural parameters of the DS-WG and plotted the transmittance as a function of its W_{eff}, while keeping the parameters of HP-WG fixed. The following definition was used for W_{eff} in the 2D situation [90].

$$W_{eff} = \frac{\left(\int_{-\infty}^{+\infty} |E(x)| dx\right)^2}{\int_{-d}^{+d} |E(x)|^2 dx} \tag{3.1}$$

where $d = d_H + d_L/2$. The transmittance is plotted along with W_{eff} in Fig. 3.5 as a function of DS-WG Si width (d_H). The smallest W_{eff} clearly occurs around d_H = 180–200 nm for various d_L, which coincides with the maximum transmittance region. This result proves that the matching of effective mode area could be critical for achieving a good connection performance, even though their mode field profiles are quite different.

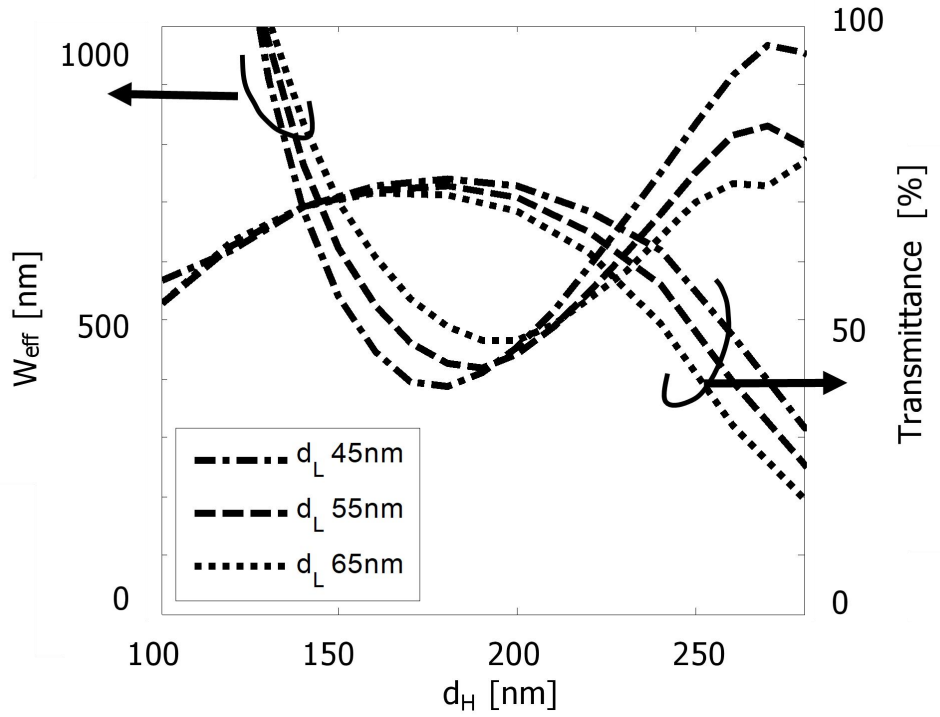

Fig. 3.5 Calculation results of W_{eff} of the DS-WG and transmittance of the direct coupler as a function of d_H for different values of d_L.

3.3.2 Reflectivity matching

Next, to further understand the coupling mechanism, it's tried to check the reflection characteristics. For this purpose, the 'local' reflectivity $\Gamma(x)$ and its average value Γ are defined over the whole waveguide cross section by the following equations:

$$\Gamma(x) = \frac{Z_{DS}(x) - Z_{HP}(x)}{Z_{DS}(x) + Z_{HP}(x)} \tag{3.2}$$

$$\Gamma = \frac{1}{2w}\sqrt{\int_{-w}^{+w} |\Gamma(x)|^2 \, dx} \tag{3.3}$$

where w represents half of the calculated region, and $Z_{DS}(x)$ and $Z_{HP}(x)$ represent the 'local' wave impedance of DS-WG and HP-WG as $Z(x) = E_x(x)/H_y(x)$, respectively. The effective mode width discussed in the previous section does not necessarily consider the point-to-point field matching, but does consider the global extent of the fields. In contrast, Γ here considers the field mismatch at all points on the waveguide

cross section. Thus, it is capable of checking a more detailed field difference.

The calculated average reflectivity (Γ) is displayed in Fig. 3.6. Reflection minima again appears at d_H = 160 nm–180 nm for various d_L. This is consistent with the results in the previous section. As a result, the matching of both effective mode area and average reflectivity (they will give us an almost identical optimal design) is critical to realizing a highly efficient coupling.

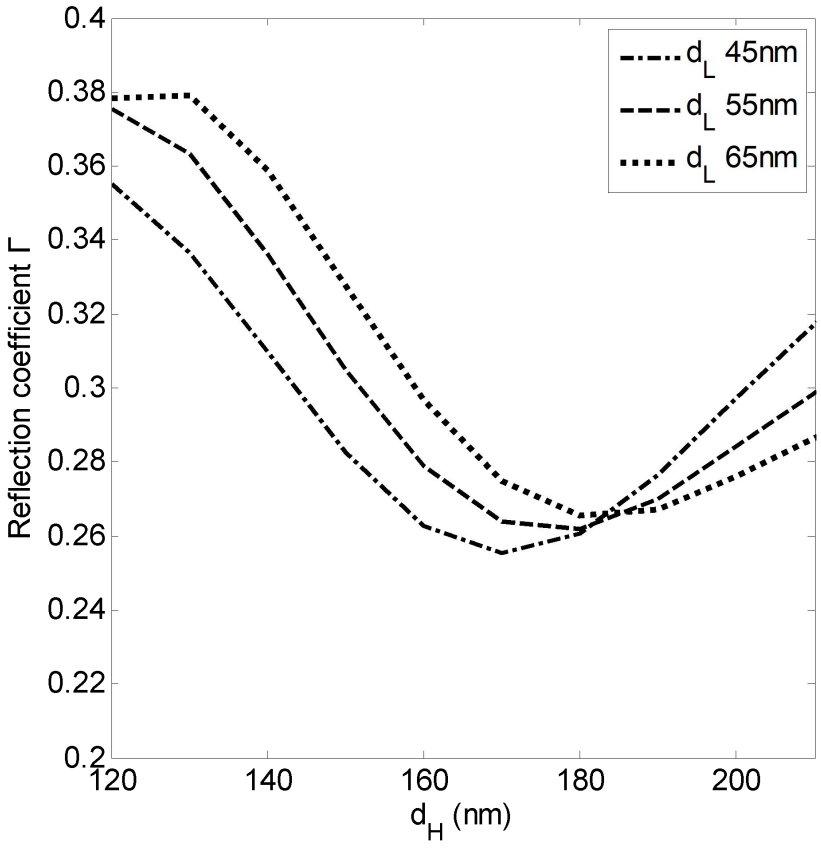

Fig. 3.6 Calculation results of the reflection coefficient Γ as a function of d_H for different values of d_L.

3.4 Improved structure design

3.4.1 Transmittance analysis

Research work on the direct coupler provides us with hints on how improve the performance. In plasmonic couplers, it has been well-known that the 'funnel effect'

phenomenon plays an important role in efficient light transmission. With the help of this effect, sub-wavelength MDM waveguides can collect light from an area significantly larger than that of its cross-section [87]. The central idea is to insert narrow air grooves into the end of the metal cladding part of the MDM waveguide and to make it function as a transition layer. The incoming electromagnetic field from the other waveguide excites the SPP waves, which creep along the surface of the grooves and finally become a part of the guided mode of the MDM. Because our HP-WG has a similar structure to that of a traditional MDM waveguide, the same performance could be expected. Based on this concept, an improved coupler is designed using air grooves as transition layers.

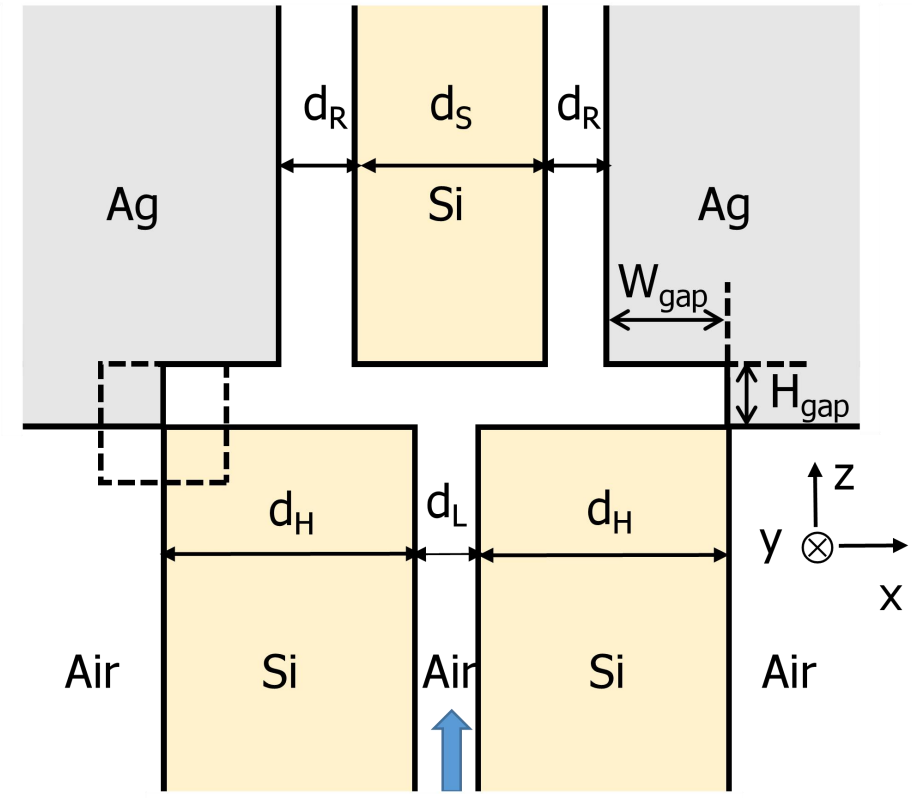

Fig. 3.7 Schematic of the improved coupler with air slots, where the dashed black block refers the calculation region of the Poynting vector in the sub-chapter 3.4.2.

Fig. 3.7 shows a schematic of the proposed coupler structure. Air grooves are inserted into the overlapped section of Ag and Si. The dotted lines denote the monitoring sections for the Poynting vector (described later).The width and height of

the air grooves are given by W_{gap} and H_{gap}, respectively. In the FDTD simulations, it's varied of d_H for a given W_{gap} and H_{gap}, and measured the transmission efficiency and reflectivity. Fig. 3.8 (a) and (b) display the transmission efficiency and reflectivity for d_L = 50 nm. For W_{gap} = 120 nm, the peak transmittance improves by approximately 25% at d_H ~ 300 nm, whereas the reflectivity reduces by approximately 25% compared to the direct coupling structure. The maximum transmission efficiency reaches more than 90% and then slowly decreases compared with the direct coupler.

As it's introduced the enhanced funnel effect caused by the weight of air grooves of the transition layers, it's believed that the optimal design of the height of those layers with optimal power fluxes from the DS-WG to HP-WG can also achieve an optimal transmittance and reflectivity. Figures 7(a) and 7(b) present the results corresponding to the variation of W_{gap} and H_{gap}. In this special design, d_H and d_L were kept constant at 200nm and 50nm, respectively. The highest transmittance is approximately about 90% when H_{gap} = 60 nm and W_{gap} = 100 nm, while the reflectivity decreases to less than 6%. The relative dimensions of each part of the improved coupler correspond to the proposed design in [85], which supports the validity of our design concept.

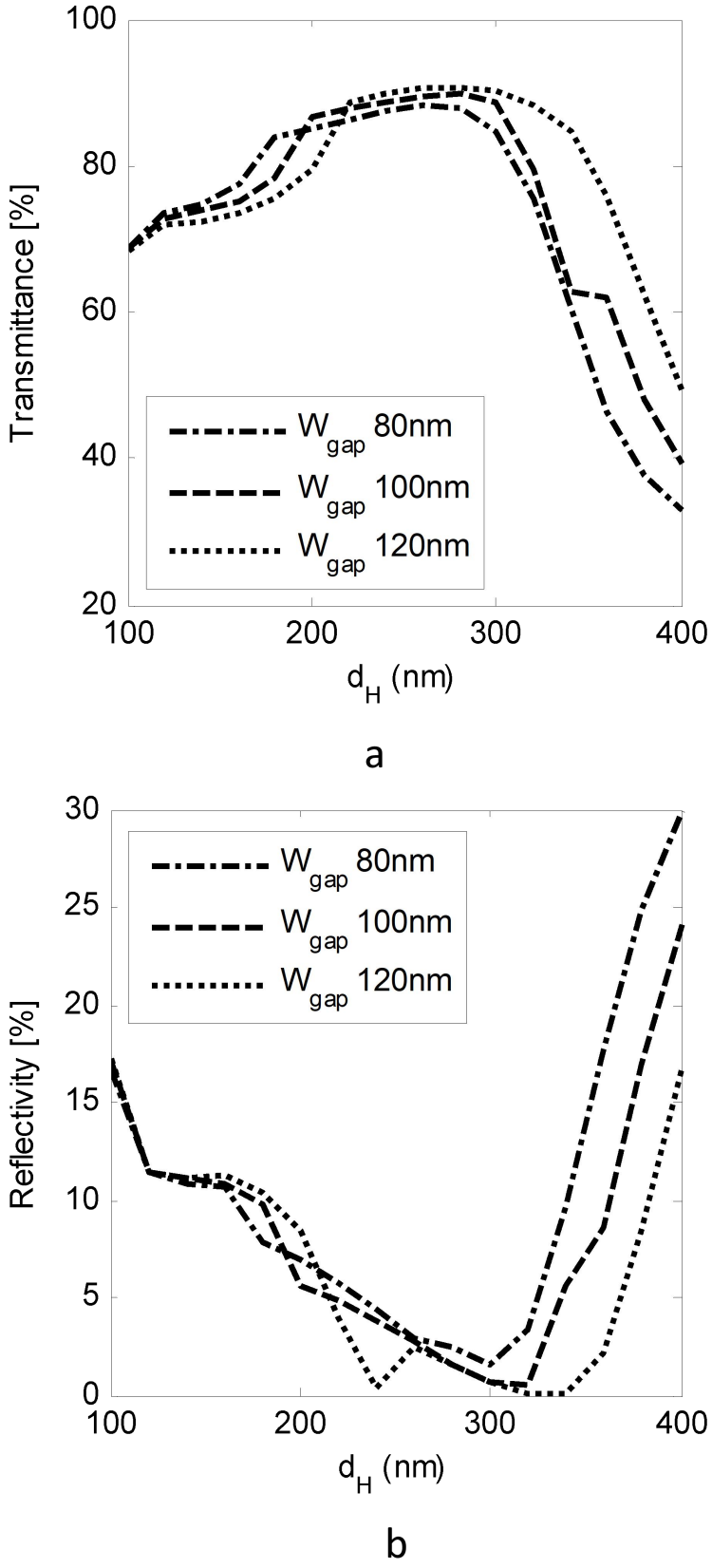

Fig. 3.8 Calculation results of the improved coupler of the (a) transmittance and (b) reflectivity shown in Fig. 3.7.

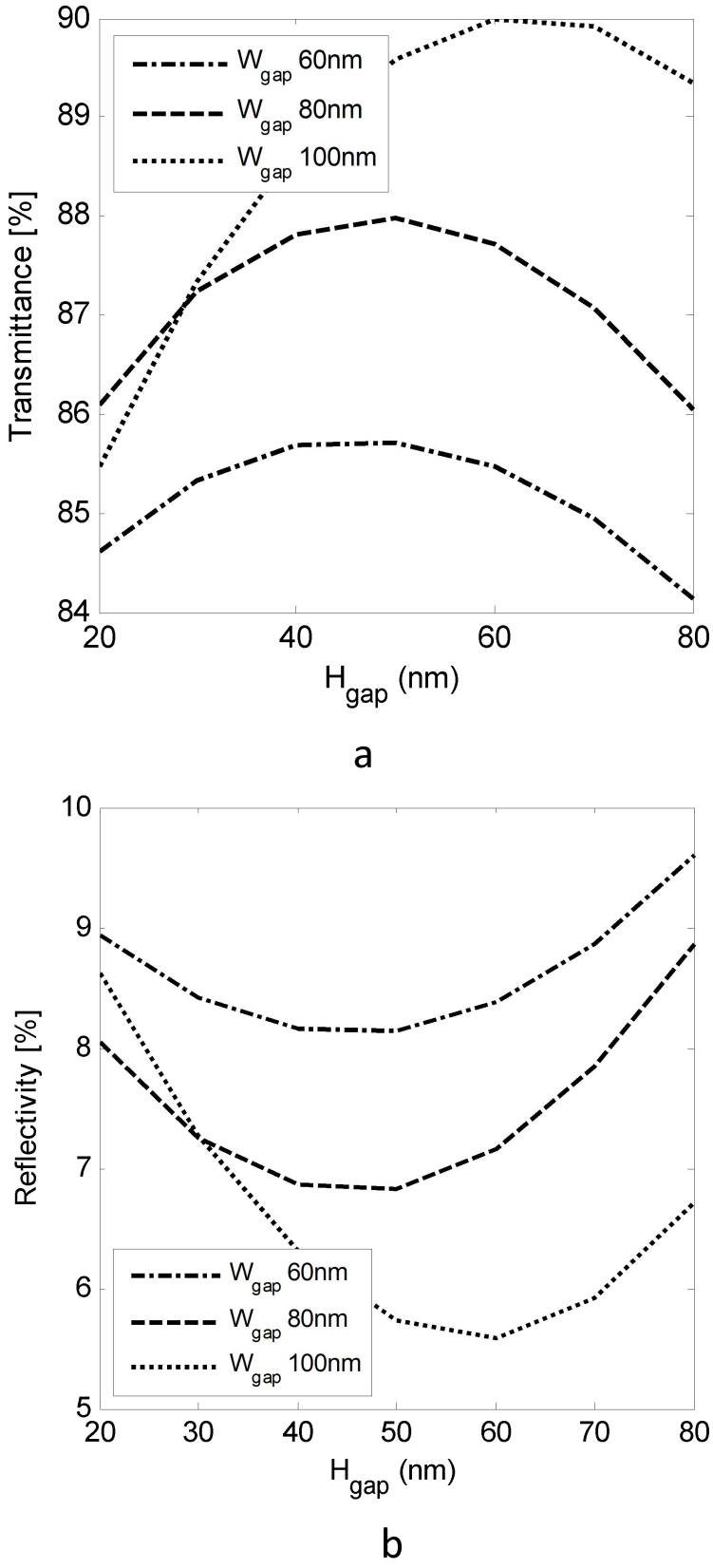

Fig. 3.9 Calculation results of the (a) transmittance and (b) reflectivity as a function of H_{gap} for different values of W_{gap}

3.4.2 Discussion of the funnel effect

To further check the appearance of the funnel effect caused by the transition layers, the time-averaged Poynting vectors without and with transition layers were visualized. The Poynting vector can record the spatial output of both the amplitude and individual components in visualization at specific times. Results are presented in Fig. 3.10 (a) and (b). The parameters are d_H = 200 nm, d_L = 50 nm, H_{gap} = 50 nm, W_{gap} = 100 nm. In the direct coupler, almost all power in the air region outside the Si waveguide and a part of the power inside the Si are reflected back (as shown in Fig. 3(c)) or radiated out of the coupler. Meanwhile, in the improved coupler, even some parts of the power in the air region (evanescent waves) can be coupled to air grooves. The enlarge of the transition region provides more fields groove into the HP-WG. With the same field distribution of slot waveguides in two couplers, a higher transmittance could be predicted because of the enhanced optical flows in the improved model.

The calculation of the Poynting vector is based on the following procedures. First, the spatial electro-magnetic field in the dashed black region of the direct coupler and the improved coupler are calculated individually via FDTD programs. The Poynting vector can be expressed by the following equation, where **E** and **H** are electric and magnetic fields at the specific time of t_s, and **r** is the spatial coordinate.

$$\mathbf{S}(\mathbf{r},t_s) = \mathbf{E}(\mathbf{r},t_s) \times \mathbf{H}(\mathbf{r},t_s) \tag{3.4}$$

Then, the amplitude can be computed as:

$$S(\mathbf{r},t_s) = \sqrt{\mathrm{Re}[S_x]^2 + \mathrm{Re}[S_y]^2 + \mathrm{Re}[S_z]^2} \tag{3.5}$$

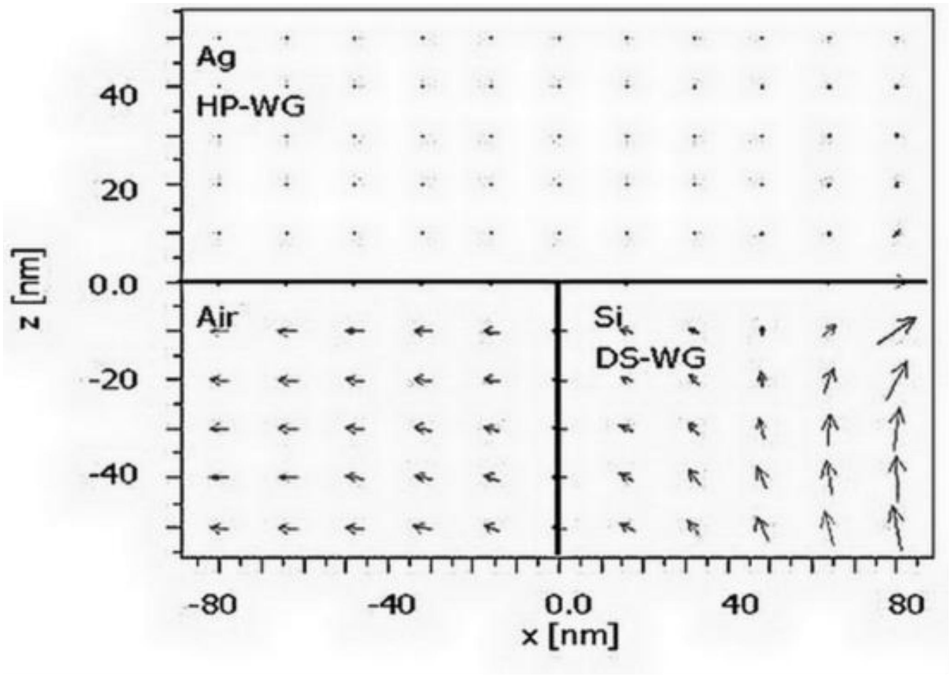

a

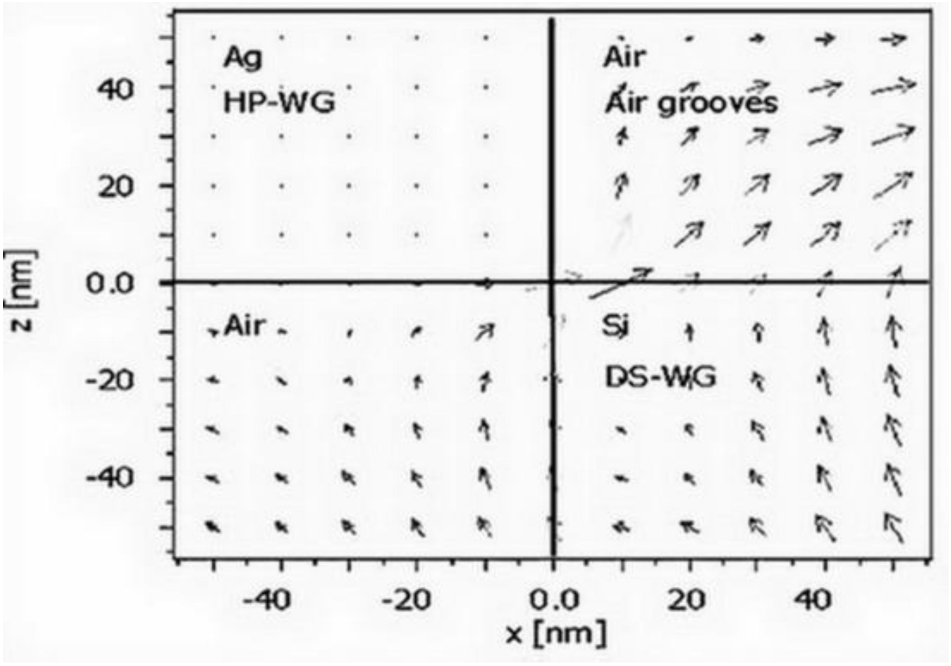

b

Fig. 3.10 Calculation results of the Poynting vector of the dashed black region in (a) Fig. 3.3 and (b) Fig. 3.7.

The broad band spectrum response could also be achieved by our coupler design. To show that, it's carefully selected the central wavelength of light source to proper value and changed the excitation type from continuous wave (CW) to pulse. Then in our FDTD program, the Fast Fourier Transform (FFT) is applied on the received time-domain wave signals. By doing so, the spectrum results were got. Figure 9 shows the spectrum response of the structures in Fig. 3(a) and 6(a). It's clearly seen that the improved coupler design shows superiority than direct coupler design in a wide wavelength range. The two design both appear low transmittance at longer wavelength region. The transmittance is measured close to the interface leading to weak wavelength dependent caused by metal.

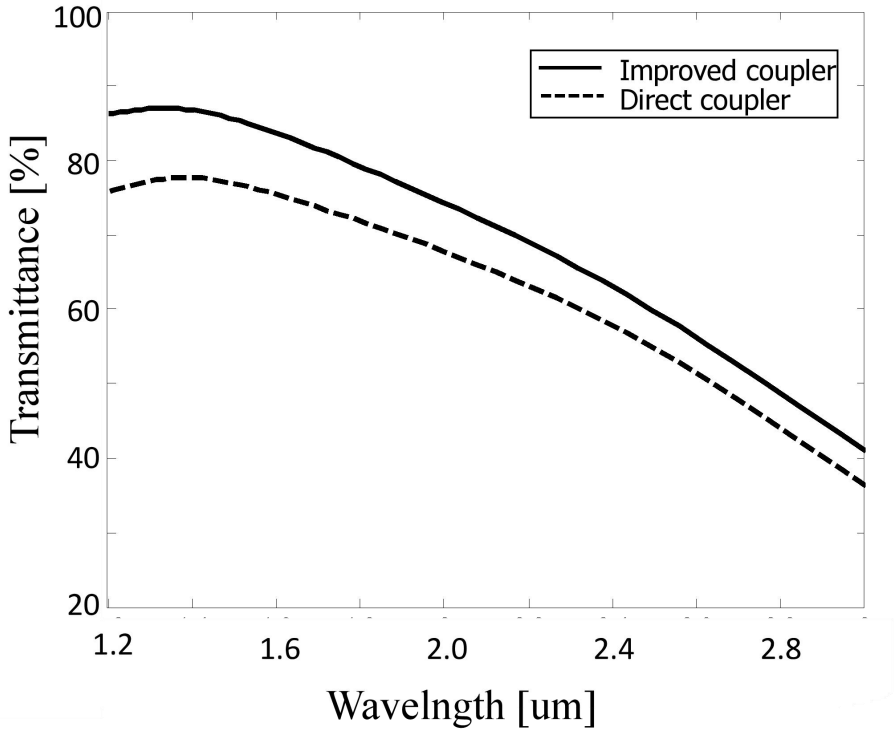

Fig. 3.11 Spectrum analysis of the improved and direct coupler

3.5 Summary

In this chapter, analyzed the factors of mode mismatch and reflectivity of a direct DS-WG/HP-WG coupler are analyzed and clarified that the matching of the effective mode area (W_{eff}) of both waveguides was important to realize highly efficient couplers. It's demonstrated that, at the optimal coupler dimension, the average local reflectance Γ(x) over the waveguide cross section became a minimum. Then, an improved high efficiency coupler is proposed using air gaps as a transition region at the DS-WG/HP-WG junction. Compared with the direct coupler, it was confirmed that the transmittance improved from 75% to 90% by the insertion of 50 nanometre transition layers instead of a several hundreds nanometre adiabatic taper. The proposed structure can enhance the transmission efficiency of optical signals between DS-WGs and HP-WGs. With this simple design and achievement, the coupler with transition layers has potential applications in modern highly integrated nano-photonic devices. Detailed physical theories behind the funnel effect and optimal design of transition layers will be studied in future work.

Chapter 4 Side-coupled Fabry-Perot filter

In this chapter, a compact side-coupled plasmonic Fabry–Perot (FP) waveguide filter is modeled using a combination of several fundamental waveguide parts, and compared its characteristics with those obtained using finite-difference time-domain (FDTD) simulations. The equivalent model of the proposed filter was regarded as three cascaded resonators, two symmetric overlapping regions as two directional couplers (DCs), and one side-coupled cavity as an FP resonator. A scattering matrix (S-matrix) analysis was employed to reveal the origin of the spectral responses. The obtained characteristics, such as different peak transmittance (mainly influenced by the DCs' overlapping length) and wide free spectral range (FSR) between two resonance modes, showed a good agreement with those obtained using FDTD simulations. By suppressing the neighboring resonance mode, through an adjustment of the DCs' overlapping length, a potential design of a 1×2 ultra-wide-FSR wavelength demultiplexing filter is demonstrated.

In section 4.1, the research background and structure of design are introduced. The structure of side-coupled filter is regarded as three cascaded resonators, where there are two symmetric overlapping regions and one side-coupled cavity. In section 4.2, the transmission model is established according to the coupled mode theory (CMT) and theories of scattering matrix. In section 4.3, the characteristics of the direct coupler and Fabry-Perot cavity are analyzed according to the above analysis. In section 4.4, a new schematic of dual-output and the characteristics of ultra-wide free spectral range are proposed. In section 4.5, a total summary is given.

4.1 Research background and device structure

The field of surface plasmon polaritons (SPPs) has been rapidly developing in recent years owing to their outstanding performance of guiding and manipulating light at the deep-subwavelength scale [91, 43]. Among the various plasmonic structures, metal-dielectric-metal (MDM) (or metal-insulator-metal (MIM)) [67, 68] structures

are particularly promising owing to their superior functionalities while maintaining propagation efficiency, simple fabrication, and low bending loss [92]. Various optical devices based on a plasmonic MDM waveguide platform, such as waveguide combiners [88, 89, 93], filters [49, 94], and sensors [95–98] have been designed and investigated. Recent years, the graphene-supported MDM waveguides have been successfully reported, which shows a new approach to control and modulate SPPs waves [99]. Owing to the remarkable properties of MDM plasmonic waveguides, they are very promising for applications in next-generation optical integrated circuits.

Wavelength selection (filtering) is one of the key technologies in optical communications. Various wavelength-selective structures based on MDM waveguides have been developed. Side-coupled ring [100], stub [101-103], and cavity-type [104, 105] two-dimensional (2D) MDM-based resonant filters have been investigated. Temporal coupled-mode theory (CMT) has been employed for the analysis of MDM filters with a side-coupled ring cavity [106], slot cavity [107], and cascaded double cavities [108].

In this chapter, a scattering-parameter model [109] of the side-coupled cavity-type plasmonic waveguide filters is presented. the whole structure is divided into three cascaded resonators, two directional couplers (DCs) and a Fabry–Perot (FP) cavity. The overlapping regions of the former resonators also act as a mirror for the FP resonator. The S-parameters of each section is obtained using the finite-difference time-domain (FDTD) simulation results. The consistency between the above semi-analytical model and FDTD simulations results validates the feasibility of the proposed method. In the FDTD simulations, the computational domain of a uniform orthogonal 2D mesh was used. The grid size was 2nm for both directions. The ends of the domain were terminated by Berenger's perfectly matched layers (PMLs). The thicknesses of the PMLs are 20 layers for each boundary.

The side-coupled plasmonic FP waveguide filter is illustrated in Fig. 4.1 (a). This structure is composed of three MDM waveguides, denoted as segments 1, 2, and 3. Segments 1 and 3 are used as the input and output waveguides, respectively, while segment 2 is used as the FP cavity. Segments 1 and 2, and 2 and 3 are connected by

directional coupling. The waveguides have equal widths. The coupling gap between the segments 2 and 1 (or 3), length of the segment 2, and overlapping length between the segments 2 and 1 (or 3), are denoted as W_{gap}, L_1, and L, respectively. The insulator medium is assumed to be air with a refractive index of 1, while the metal medium is assumed to be Ag. The frequency-dependent relative permittivity of Ag can be obtained using the Drude model [110–112]:

$$\varepsilon(\omega) = \varepsilon_\infty - \frac{\omega_p^2}{\omega(j\gamma + \omega)} \tag{4.1}$$

where ω is the angular frequency of the incident light, ε_∞ = 3.7 is the dielectric constant at infinite angular frequency, ω_p = 9.1 eV and γ = 0.018 eV are the bulk plasma frequency and damping frequency of the oscillations, respectively, and j is the imaginary unit.

In practical devices, the core height is finite. However, in this study, in order to simplify the analysis of the main operation mechanisms, a 2D approximation is employed, i.e., the structure in Fig. 4.1 (a) was assumed to extend infinitely into the direction normal to the plane of the figure.

Then, the device is divided into three building blocks, as shown in Fig. 4.1 (b). The building blocks consist of two DCs and one FP cavity (consisted of a simple MDM waveguide). The two DCs couple the device to the external waveguide, and act as a pair of mirrors for the FP cavity. The DC is modeled by Fig. 4.1 (c), where four ports are defined and marked with numbers from 1 to 4. The straight forward waves from the launched port are represented by SFW, while the power and of the crosstalk in the neighboring waveguide are represented by COW.

Since the definition of the FP cavity and DC are finished, therefore, the equivalent model can be treated as an FP- type cavity (side-coupled MDM waveguide) and two reflectors (DCs). The *S*-parameters of each block were obtained from the FDTD simulation results. The filter characteristics were expressed by combining the *S*-parameters.

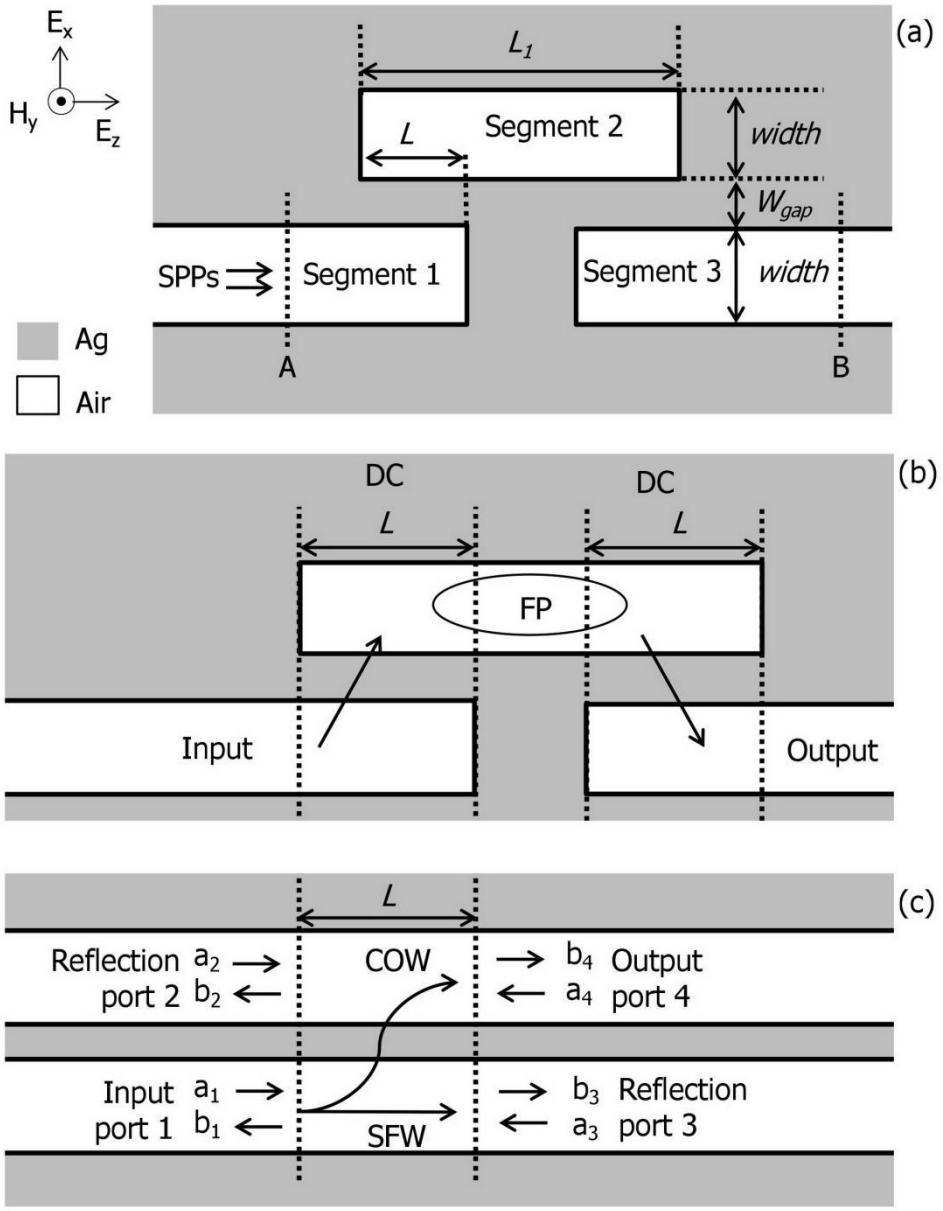

Fig. 4.1 Schematic and equivalent model of a side-coupled plasmonic coupler FP waveguide filter. (a) Schematic of the waveguide filter. The guided mode is assumed to propagate along the *z*-axis. The wide-band transverse-magnetic (TM) polarized SPPs emerge from the left side of the segment 1. (b) Equivalent model of the proposed filter. (c) Definition of the ports in the two parallel MDM waveguides. The SFW and COW represent the straight forward waves and the cross-over waves in the original and neighboring waveguides, respectively.

4.2 Structure analysis

The study of the directional plasmonic coupler is presented in this sub-chapter. The schematic of a plasmonic directional coupler is listed on Fig. 4.2 (a), where two parallel plasmonic waveguides are set and four ports are defined and marked as numbers of 1-4. The *x* direction is labeled for the propagation. The waveguide width and gap between two waveguides are set ass 50 nm and 20 nm, respectively.

The fundamental TM polarized SPP wave is launched from port 1 along the *x*-direction. The transmitted waves in port 3 and cross coupled waves in port 4 are represented by S_{31} and S_{41}, respectively, where the square values represent the power of them.

As it's known, the propagation mode in plasmonic owns much propagation loss (α), which are not considered in the dielectric directional coupler. Thus, the power will decrease with the propagation.

The calculation of parameters of S-matrix as a function waveguide length *x* is shown on Fig. 4.2 (b), where the SPP waves are launched from port 1 and port 3 and port 4 are the transmission port and crosstalk port, respectively. It's clear seen from the figure that the power exchange from two waveguides periodically with the propagation direction *x*. The coupling length is marked by L_c, which relates with the wavelength (currently launched free space wavelength λ_0 = 900 nm). The L_c is also related with the geometry structure of the two waveguides, which are not discussed here. Meanwhile, the envelop of the S_{31} and S_{41}, i.e. total power in each channel, decrease as wished. The calculation of the directional coupler between two plasmonic waveguides gives the fundamental background.

The field distribution of the directional coupler composed by two parallel plasmonic waveguides is also plotted in Fig. 4.3. It's clear seen the field distribution decays along with propagation direction, which confirmed the basic theory mentioned in chapter 2.

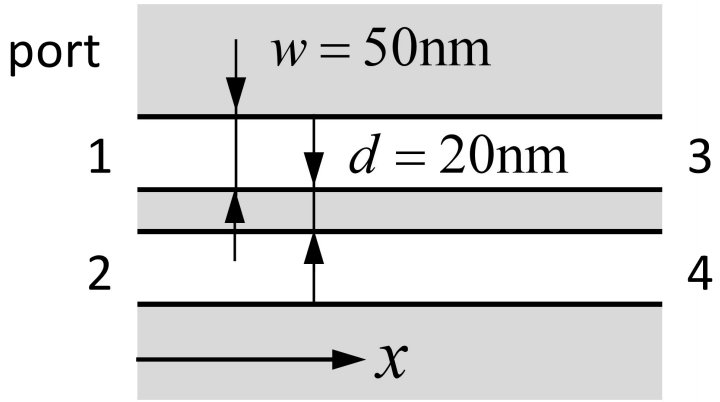

a

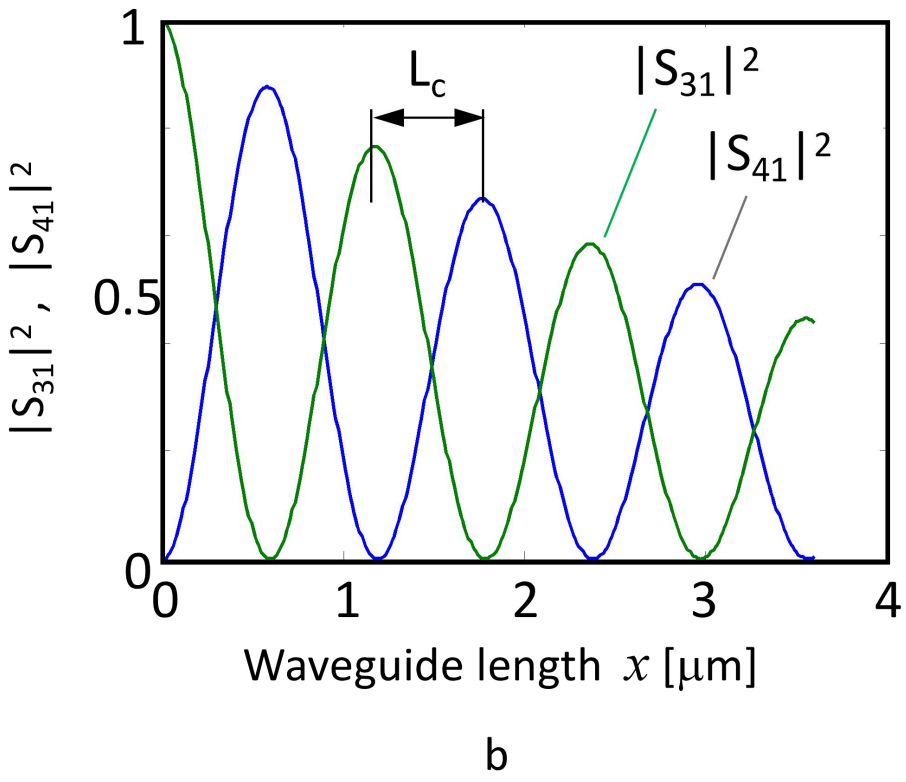

b

Fig. 4.2 (a) Model of parallel placement of two plasmonic waveguides. (b) Calculation results of the S_{31} and S_{41} in ports 3 and 3,respectively.

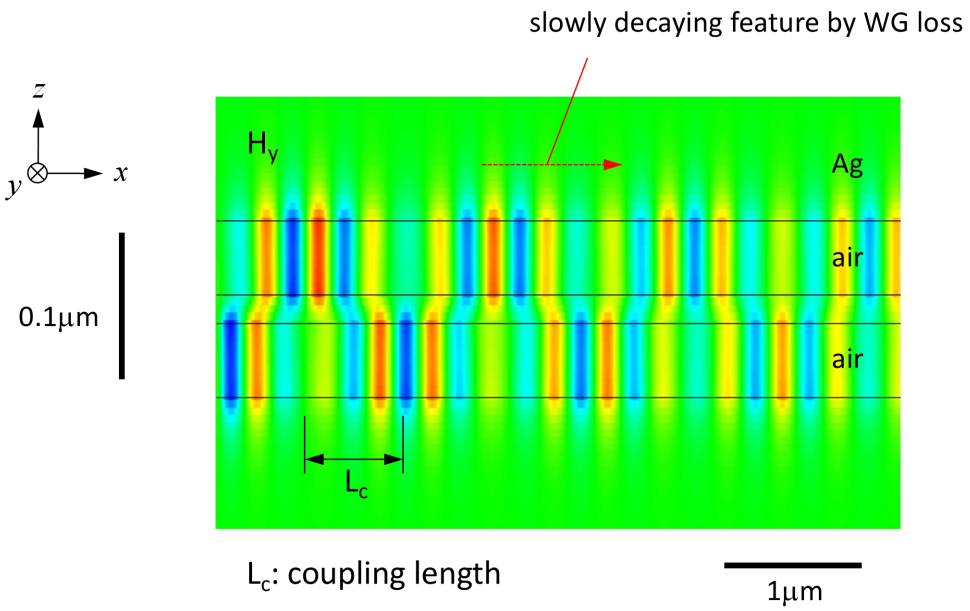

Fig. 4.3 Field distribution of H_y component of the directional coupler of two plasmonic waveguides.

The propagation loss and propagation results of a straight plasmonic waveguide is investigated detail via FDTD calculations. The calculation model is showed in Fig. 4.4 (a), where the launched SPP mode is propagated from left to right. The propagation constant β and loss parameter α are then calculated along with the field distribution. The calculation of the dispersion relation of the fundamental SPP mode as a function of wavelength is shown on Fig. 4.4(b). The data of the propagation constant and loss are used in the following semi-analysis model.

It's should note that the fundamental theory of the propagation of a SPP mode in a plasmonic waveguide could also be established on the following equation theoretically, where w is the width of the plasmonic waveguide, ε_m and ε_d are the dielectric constants of the metal cladding and the bus waveguide, $k_0 = 2\pi/\lambda$ is the wave vector of incident light in vacuum, and $n_{eff} = \beta_{spp}/k_0$ is the effective index (ERI) of SPP mode.

$$\varepsilon_m \sqrt{n_{eff}^2 - \varepsilon_d} \tanh\left(\frac{w k_0 \sqrt{n_{eff}^2 - \varepsilon_d}}{2}\right) + \varepsilon_d \sqrt{n_{eff}^2 - \varepsilon_m} = 0 \qquad (4.2)$$

By solving Eq. (4-2), the propagation constant can be got. The simple FDTD calculation is applied for the results. The field distribution of H_y component of the directional coupler of two plasmonic waveguides is shown in Fig. 4.4, where the slow decaying feature by waveguide loss can be confirmed.

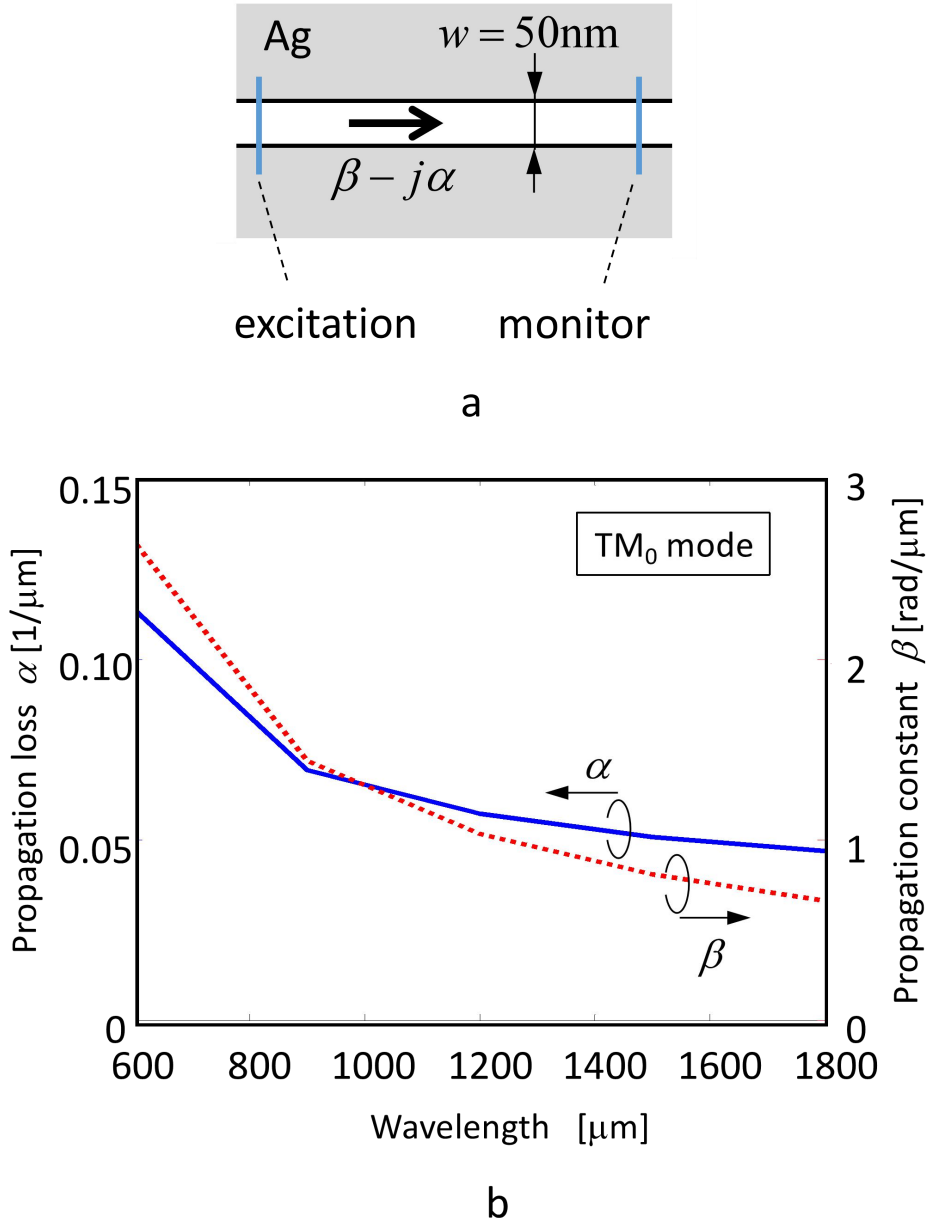

Fig. 4.4 (a) Model and (b) calculation results of a straight plasmonic waveguide for the parameters of propagation constant β and loss α.

Then, the input–output characteristics of the DCs is studied using CMT and S-matrix analysis. The DCs are approximated as two parallel infinitely long coupled MDM waveguides with a pair of cross-ports terminated as shown in Fig. 4.1(c). We defined one input port (port 1), one output port (port 4), and two reflection ports (ports 2 and 3), where a_m and b_m (m is in the range of 1–4) represented the amplitude of waves directly incident on the port and directly away from the port, respectively. Through the definition of each port, they can be classified as two external ports (port 1, 4) and two internal ports (port 2, 3), which indicates that only $a_{1,4}$ and $b_{1,4}$ are input and output waves.

By considering the operation of a conventional DC, we approximated the *S*-matrix representation of the two parallel finitely long MDM waveguides as:

$$\begin{bmatrix} b_1 \\ b_2 \\ b_3 \\ b_4 \end{bmatrix} = \begin{bmatrix} 0 & 0 & c & s \\ 0 & 0 & s & c \\ c & s & 0 & 0 \\ s & c & 0 & 0 \end{bmatrix} \begin{bmatrix} a_1 \\ a_2 \\ a_3 \\ a_4 \end{bmatrix} \tag{4.3}$$

$$\begin{cases} c = e^{-\alpha L} \cos \kappa L e^{j\theta} \\ s = j \cdot e^{-\alpha L} \sin \kappa L e^{j\theta} \end{cases} \tag{4.4}$$

where c and s represent the crossover wave (COW) and straight-forward wave (SFW) labeled in Fig. 4.1(b), respectively; α, κ, L, and θ represent the propagation loss (metal absorption), coupling constant, coupling length (DC's overlapping length), and phase retardation after passing a length of L, respectively. The parameters α and κ were obtained using the decaying oscillatory field distributions of the waveguides, obtained by the FDTD simulations. Assuming that the input signal is only entering to the port 1 and not to the port 4 (port 4 emits the outgoing wave only), the vector of input waves is the then represented as $[a_1, a_2, a_3, 0]^T$. Here, the incoming waves to the two internal reflection ports (a_2 and a_3) are generated by the a_1 by the termination of the coupler; e.g., $a_2 = f(a_1)$, and $a_3 = g(a_1)$, where f and g are different functions. Based on these analysis, the transmission and reflection coefficients of the whole coupler can be expressed as the forward transmitted and backward reflected waves normalized by the input waves, i.e., S_{41} $(t) = b_4/a_1$, and S_{11} $(r) = b_1/a_1$.

The operation of an MDM DC with a finite length (two reflection ports) can be revealed by terminating the pair of cross-ports with metallic mirrors. For example, the output from one port is again input to the same port with a finite fraction. This can be represented as:

$$\begin{cases} a_2 = r_{mirror} b_2 \\ a_3 = r_{mirror} b_3 \end{cases} \tag{4.5}$$

where r is the complex reflection coefficient at the waveguide's end.

The total transmission and reflection characteristics of a DC with a finite length can be obtained by considering the multiple reflections at the terminated ends. Assuming an ideal-mirror type of reflection ($r_{mirror} \approx -1$), they can be expressed as:

$$t = b_4 / a_1 = s + \frac{c^2 s e^{j\Delta\theta}}{1 - s^2 e^{j\Delta\theta}} \tag{4.6}$$

$$r = b_1 / a_1 = \frac{c^2}{1 - s^2 e^{j\Delta\theta}} \tag{4.7}$$

where $\Delta\theta$ (= 2θ) is the phase shift per a round-trip propagation in the coupler. The transmittance and reflectivity of the two DCs are defined as $T = |t|^2$ and $R = |r|^2$, respectively. According to Eq. (4-3), a rough derivation process is shown as follows: $b_1 = c*a_3 = c*g(a_1)$, and $b_4 = s*a_1 + c*a_2 = s*a_1 + c*f(a_1)$.

Therefore, the total transmitted and reflected waves of the equivalent model with three cascaded segments can be expressed with the coefficients:

$$t_{all} = t^2 \frac{e^{-j\beta L_1}}{1 - r^2 e^{-2j\beta L_1}} \tag{4.8}$$

$$r_{all} = r + rt^2 \frac{e^{-2j\beta L_1}}{1 - t^2 e^{-2j\beta L_1}} \tag{4.9}$$

where t and r are the transmission and reflection coefficients of the DC (Eqs. (4-6) and (4-7)), respectively; $\beta = 2\pi n_{eff}/\lambda$ and L_1 denote the propagation constant and FP cavity's length, respectively. In the same way, the transmittance and reflectivity of the equivalent model are defined as $T_{all} = |t_{all}|^2$ and $R_{all} = |r_{all}|^2$, respectively.

4.3 Filtering characteristics

4.3.1 Characteristics of the direct coupler

Fig. 4.5 (a) shows the transmittance of the DC as a function of the overlapping length L at a fixed wavelength of 600 nm. The width and W_{gap} were set to 50 nm and 20 nm, respectively. The solid and dashed curves represent the DC's transmittance obtained using the proposed equivalent model and FDTD simulation, respectively. The dotted curve represents the power of the COW (1st output wave), employed in the analysis. Fig. 4.5 (a) shows that the solid and dashed lines highly coincide, which implies that the theoretical results are in good agreement with the FDTD simulations. In addition, their envelopes match with the dotted curve. For a further analysis of the multiple wave interference (dips and peaks), we plotted the 1st- and 2nd-order transmitted waves in Figs. 4.5 (b) and (c), respectively. The 1st-order transmitted wave represents the directly cross coupling of incident waves from port 1 to port 4 (COW in Fig. 4.1 (c)). The situation of the 2nd-order transmitted wave is a little complex. Considering the incident waves split into two beams, one is 1st-COW (1st-order transmitted wave), and the other is 1st-SFW. To extract the 2nd-order transmitted wave needs three stages:

1) When the 1st-SFW reaches the reflection port 3, it will be reflected back.

2) The reflected 1st-SFW will once again split into two beams. One is the 2nd-SFW and the other is the 2nd-COW. On the one hand, the 2nd-SFW will directly output at port 1 as the 1st-order reflected wave. On the other hand, once the 2nd-COW reaches port 2, it will be reflected back in the same way.

3) The reflected 2nd-COW also splits into two beams, a 3rd-SFW and a 3rd-COW. The 3rd-SFW composes the 2nd-order transmitted wave. The 3rd-COW will generate the 3rd-order transmitted wave through the same two reflections.

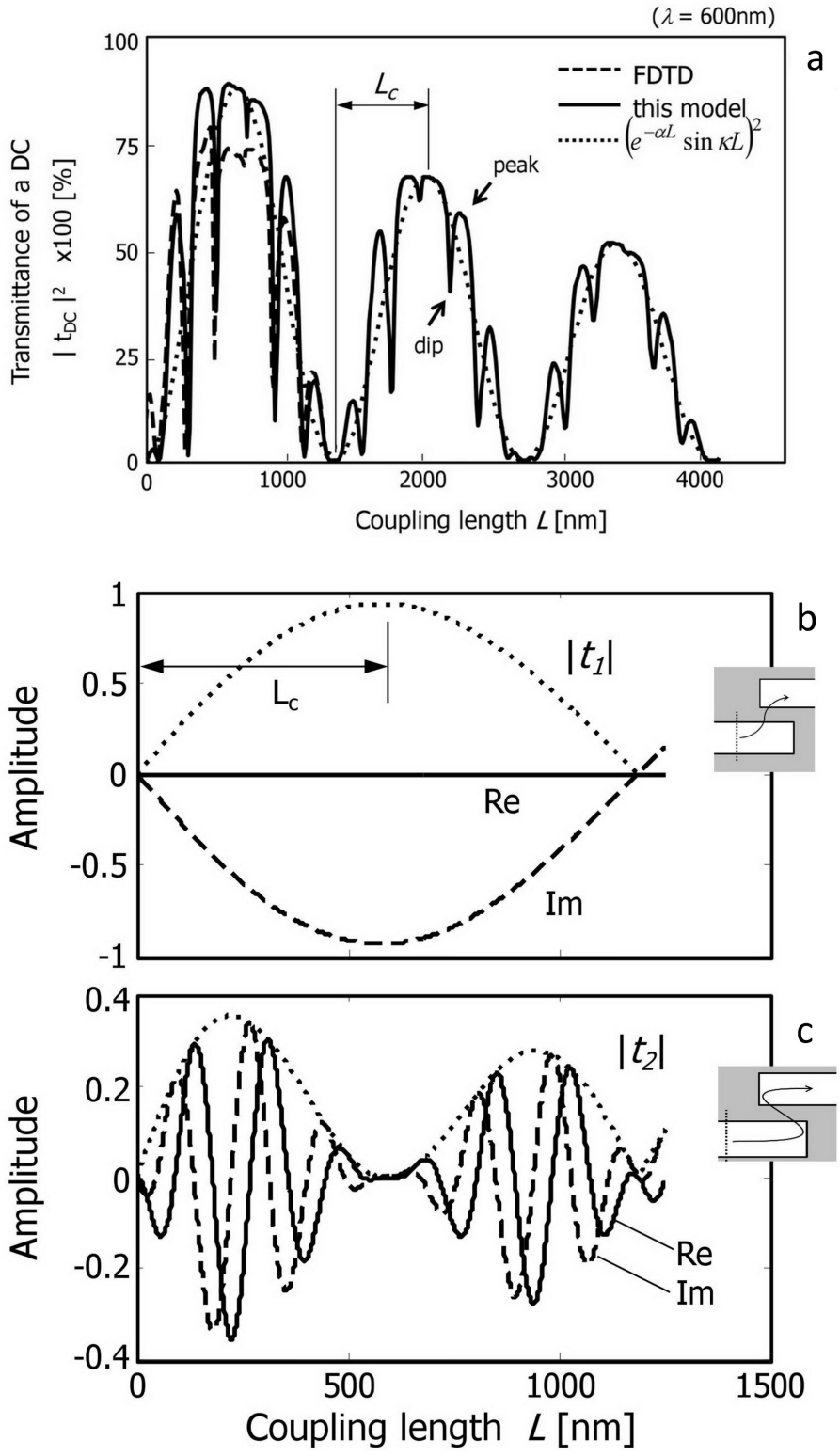

Fig. 4.5 Basic input-output characteristics of the DC. (a) Transmittance of the DC at a fixed wavelength of 600 nm, for different overlapping length L. (b) 1st-order output wave component of the result shown in (a). The inset shows the form of the 1st-order output wave. The 2nd-order output wave component of the result in (a). The

inset shows the form of the 2nd-order output wave.

From these steps, we can clear view that the phase delay (phase shift per round-trip in the coupler) between each neighboring order transmitted wave is the same, which maintains the interference stable. The insets in Figs. 4.5 (b) and (c) show the physical propagation directions of the 1st- and 2nd-order waves, respectively. Figs. 4.5 (b) and (c) reveal that in one period of the 1st-order wave, the 2nd-order wave exhibits a fixed number of periods, which verifies the stability of the interference effect over a large overlapping length. The sharp dips and peaks in Fig. 4.5 (a) can be attributed to the superposition of the 1st- and 2nd-order output waves. Other higher-order output waves also participate in the interference; however, the 1st- and 2nd-order waves are dominant. For example, the calculations showed that the amplitude of the envelope of the 3rd-order output wave is smaller than 0.1. The discrepancies between our model (solid curve) and FDTD simulation (dashed curve) results in Fig. 4.5 (a) could be attributed to the directional coupling at the waveguide's end, from segment 1 to segment 2, which is not considered in our model.

In order to reveal further insights in the frequency range, we plotted the transmittance and reflectivity using the proposed analytical model as a function of the wavelength, for two overlapping lengths of 300 nm and 400 nm, as shown in Fig. 4.6. Both transmittance and reflectivity exhibit large variations in the wavelength range of 800–1,500 nm, for the two overlapping lengths.

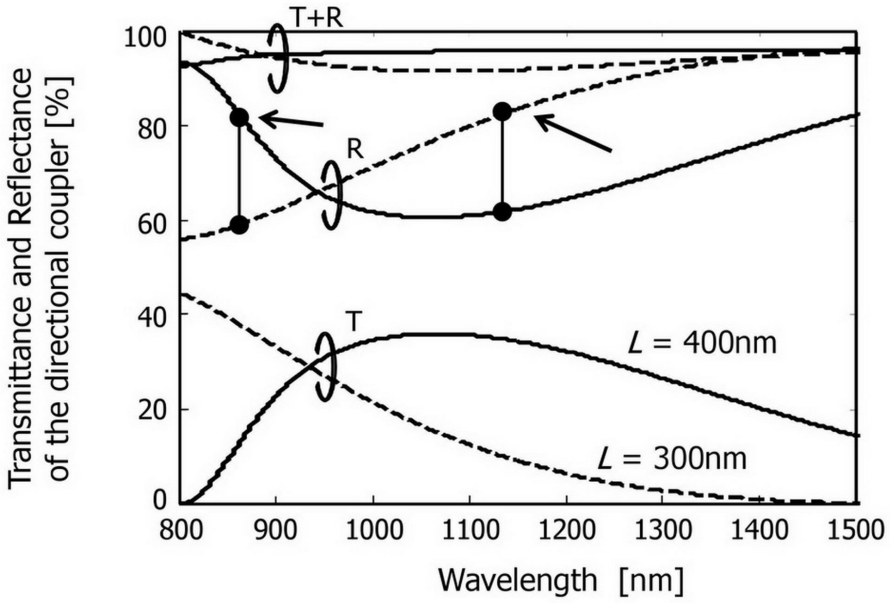

Fig. 4.6 Transmittance and reflectivity of the DC as a function of the wavelength, for overlapping length of 300 and 400 nm.

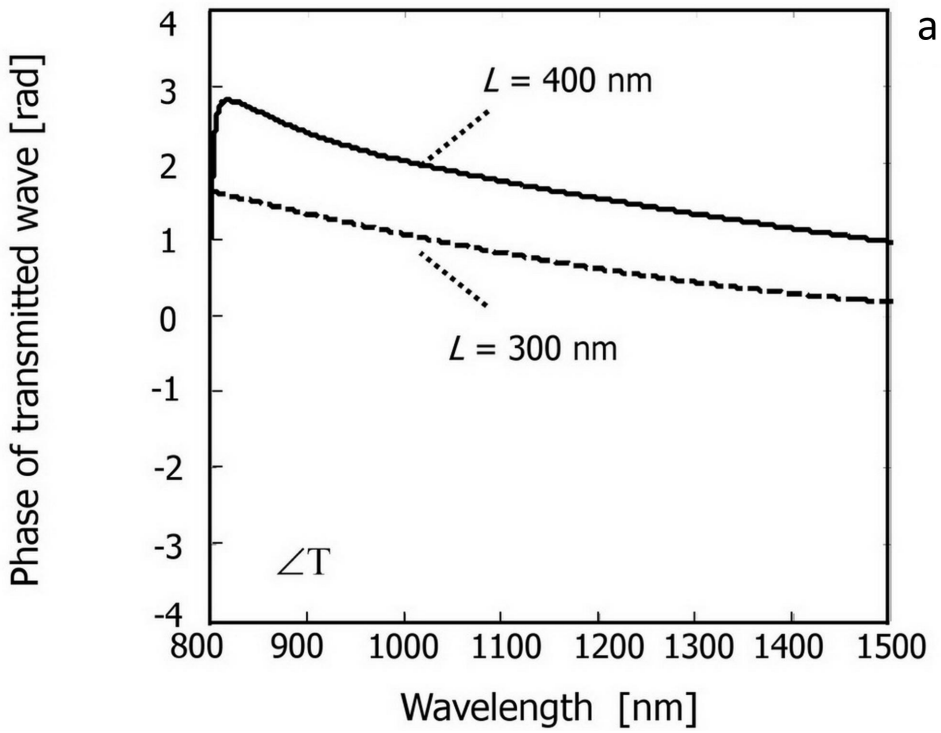

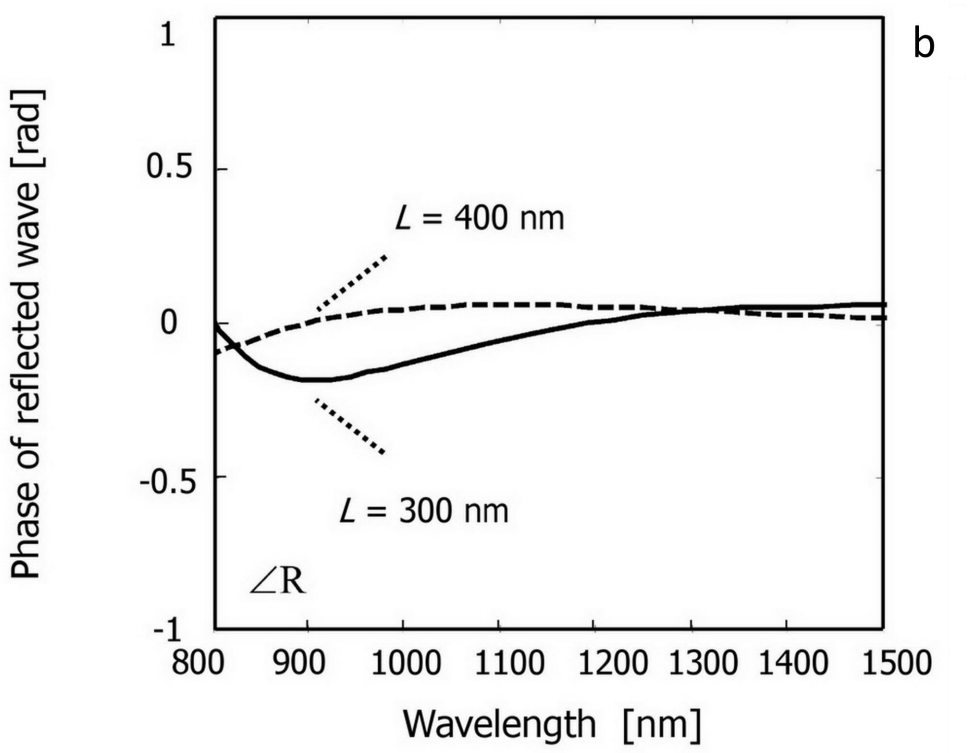

Fig. 4.7 Phase variations of the (a) transmitted waves and (b) reflected waves.

The total sum of the transmittance and reflectivity is slightly smaller than 100%, owing to the metal absorption loss. These results are related with our previous discussion on the multiple-wave interference in the overlapping region. Owing to the interference, the transmittance and reflectivity could change the “mirror reflectors” behavior, and could exhibit new characteristics in the FP cavity, as discussed in the next section.

Figs. 4.7 (a) and (b) show the spectral phases of the transmitted and reflected waves, respectively, for both overlapping lengths. The reflected phases for both lengths are almost constant in the analyzed wavelength range.

4.3.2 Characteristics of the Fabry-Perot filter

We investigated the basic characteristics of the DCs, and analyzed the core FP resonator, where the FP interference mainly occurs. The guided wave exhibits a phase retardation ($\Delta\varphi$) and loss as it passes through this part. Therefore, the *S*-matrix becomes diagonal. As the total phase delay per a round-trip propagation in the cavity satisfies the resonant condition, the resonant wavelength λ_m is [101]:

$$\lambda_m = \frac{2n_{eff}L_1}{m - \varphi_r/\pi} \tag{4.10}$$

where n_{eff}, L_1, m, and φ_r denote the real part of the effective index of the waveguide, length of the cavity, number of antinodes of the standing SPP waves, and phase shift upon reflection at the interface between segments 1 and 2, respectively. It's clear seen that the resonant wavelength is a nearly linear relation with cavity length.

The cavity length L_1 was set to 1200 nm, while all other parameters had the same values as above. Fig. 4.8 (a) shows the transmittance for an ideal lossless ($\alpha = 0$) FP interference, obtained using the reflectivity calculated above. Two wave peaks with a transmittance of 100% appear at around 850 nm and 1120 nm for both overlapping lengths. These two intrinsic wavelength peaks are consistent with Eq. (4-10) with an approximation of Re(n_{eff}) = 1.4, $\varphi_r \approx 0$, and m = 3 and 4. We should note that, compared with FDTD simulations, the slightly mismatch of resonant wavelength calculated by Eq. (4-10) comes from the dispersion of the SPP mode and $\varphi_r \neq 0$.

The full-width-at-half-maximum (FWHM) values of each peak can be correlated with the variations in the reflectivity; a larger R leads to a wider FWHM and vice versa. We plotted the results of the theoretical calculations of the transmittance using Eqs. (4-8) and (4-9), respectively, along with the FDTD simulation results in a lossy ($\alpha \neq 0$) case, as shown in Fig. 4.8 (b). The comparison with the FDTD simulation further confirms the validity of our equivalent model. In Fig. 4.8 (b), two peaks appear at almost the same wavelengths as in Fig. 4.8 (a), but with different transmittance values.

The peak transmittance values for the overlapping length of 300 nm are 75% at 850 nm and 20% at 1120 nm; an opposite behavior is observed for the overlapping length of 400 nm. Using the above analysis, we can conclude that the total transmission loss is mainly attributed to metal absorption losses, and that the large transmittance differences of each resonant mode can be easily controlled by modifying the overlapping length.

These results show that an optimization could almost vanish the useless intrinsic resonant peak in the FP-type plasmonic filter in order to achieve an ultra-high free spectral range (FSR).

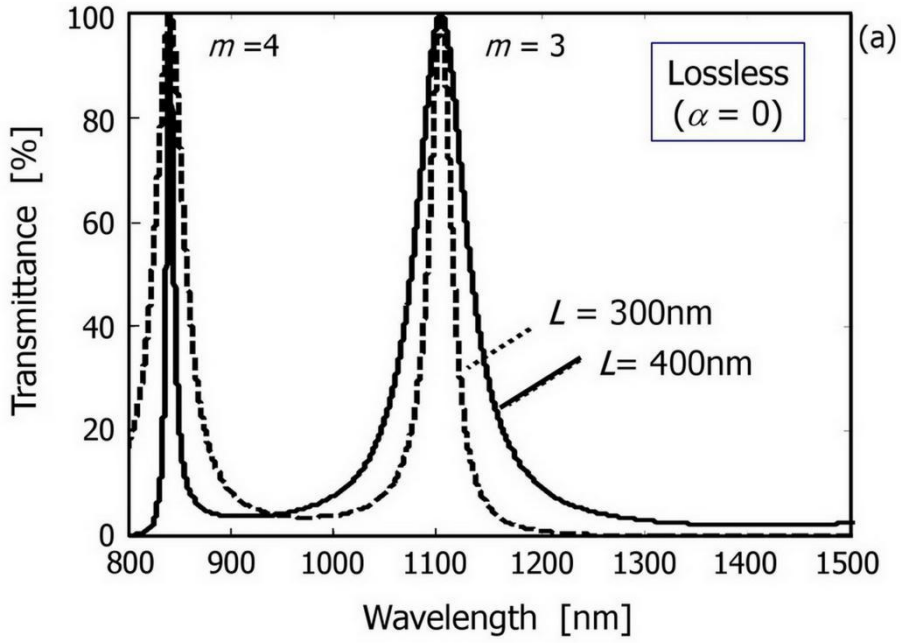

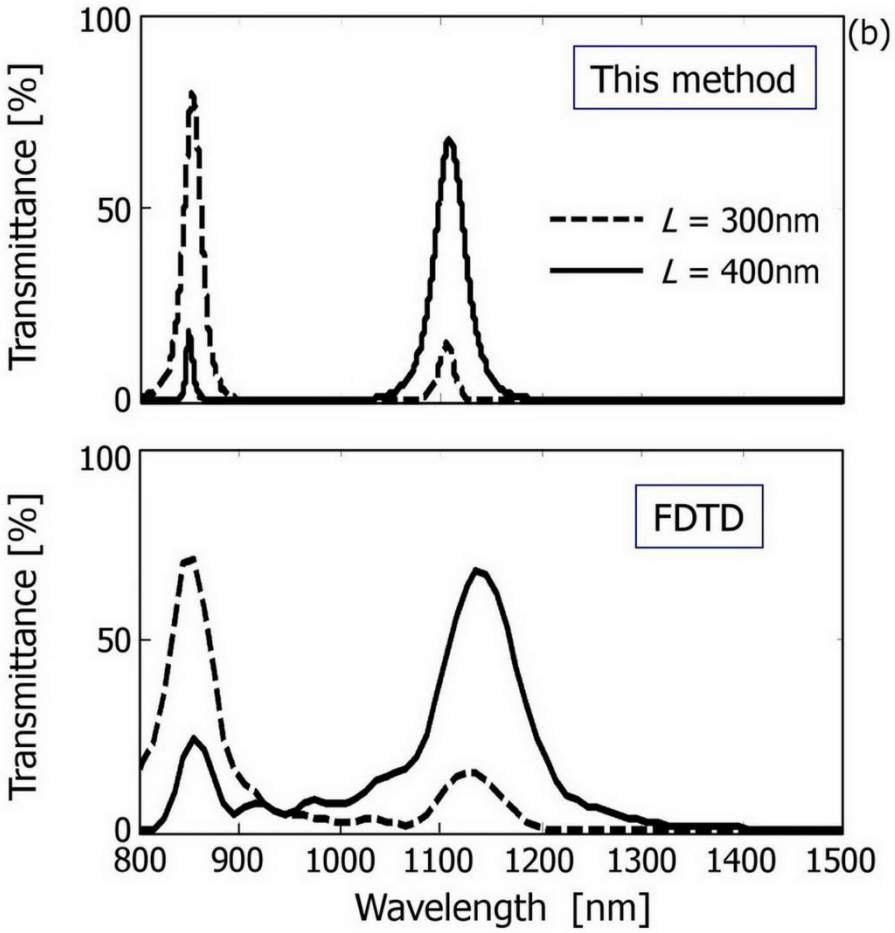

Fig. 4.8 Basic input-output characteristics of the FP resonance cavity. (a) Spectral response of an ideal FP interferometer without loss ($\alpha = 0$). (b) Spectral responses with loss ($\alpha \neq 0$), obtained using the proposed model and FDTD calculations.

4.4 Application of a dual-output filter

4.4.1 Dual-output design

Fig. 4.9 (a) shows a schematic of 1×2 wavelength demultiplexing structures based on MDM side-coupled cavities. The wavelength demultiplexing structure consists of two air cavities with different lengths, which act as resonant spaces to select at most two different wavelengths. The lengths of the two side-coupled air cavities, denoted as L_2 and L_3 are set to 1,150 nm and 1,200 nm, respectively; L represents the overlapping length between MDM waveguides and air cavities. All of the overlapping lengths are identical; the other parameters are the same as above. Port 1 is the input port, while ports 2 and 3 are the output ports. The FDTD method (section 3) is employed to obtain the transmission spectra.

Fig. 4.9 (b) shows the transmission spectra at the two output ports for L = 400 nm. The dashed and solid curves represent $|S_{21}|^2$ and $|S_{31}|^2$ of the ports 2 and 3, respectively. The two major peaks at 1,153 nm and 1,205 nm, and two minor peaks around 900 nm showed the possibility of wavelength tunability. The difference in the propagation loss of the main resonant peaks at the wavelengths of approximately 1,200 nm can be attributed to the different lengths of the air cavities.

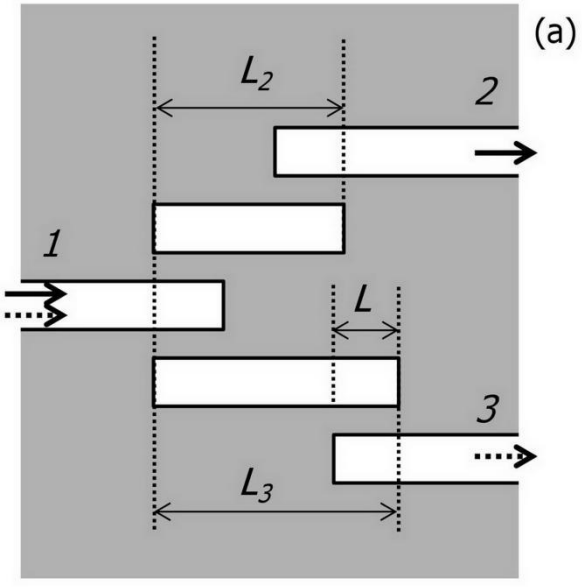

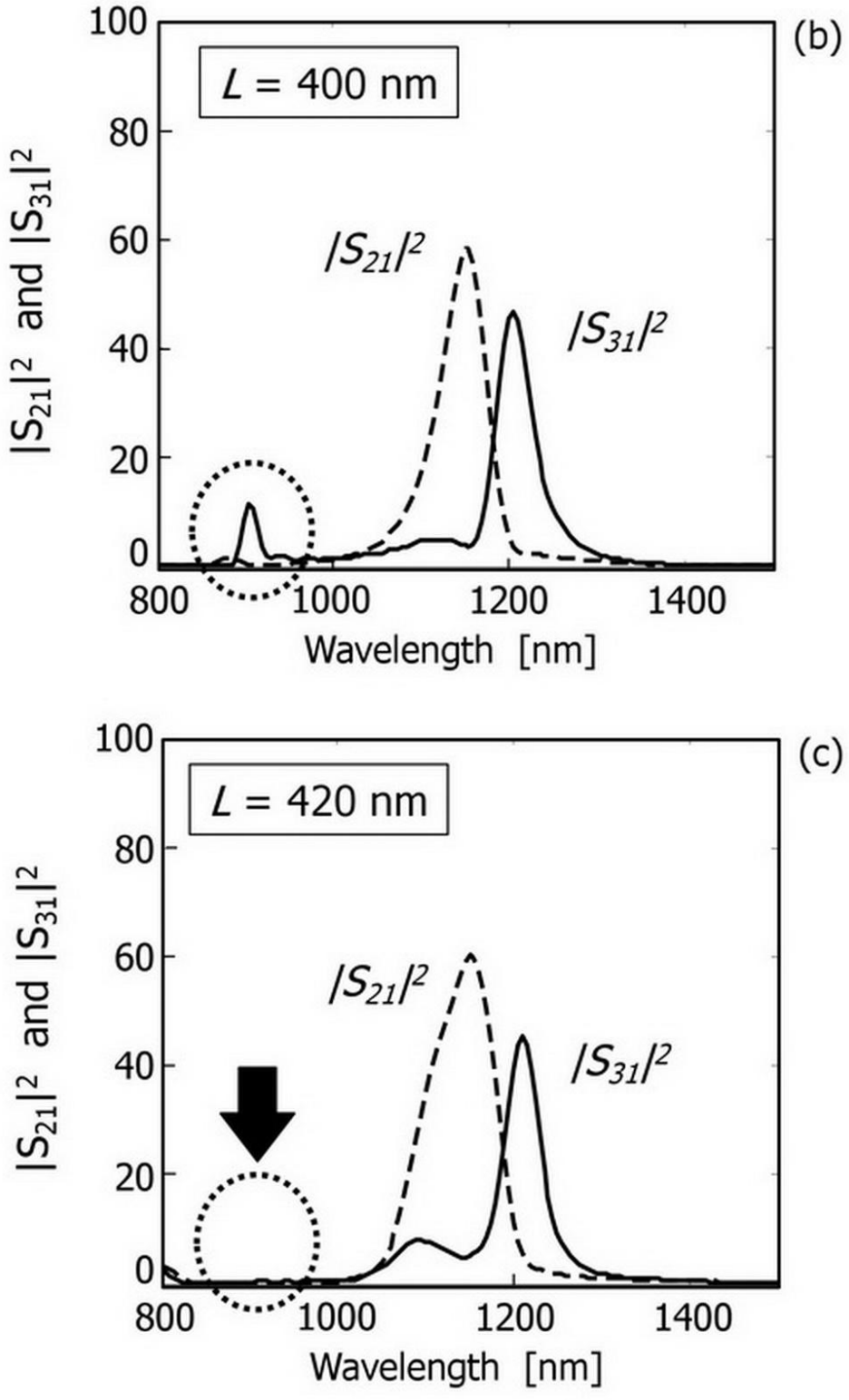

Fig. 4.9 Schematic and spectral response of the novel 1x2 wavelength demultiplexer. (a) Schematic of the demultiplexer. Calculation results of the spectral responses for (b) L = 400 nm and (c) L = 420 nm.

4.4.2 Characteristics of ultra-wide free spectral range

In order to achieve a wide-band filter design, the neighboring minor resonance mode need to be suppressed. Fig. 4.9 (c) shows the optimized results by adjusting the DC's overlapping length L to 420 nm. The neighboring resonance mode around 900 nm vanished. This optimization method is consistent with the conclusions in the previous chapter, and can be also employed in other target wavelength regions by adjusting the overlapping length.

4.5 Summary

We proposed an analytical model for an ultra-compact plasmonic filter using a side-coupled cavity as a resonator. The spatial and spectral responses obtained by the proposed model showed a good agreement with the FDTD simulations. Both theoretical analysis and numerical calculations demonstrated the ability to reduce or vanish the intrinsic transmittance peak of the FP cavity by varying the overlapping length. The control of the length of the air cavities enables to develop a tunable-wavelength filter design, while that of the DCs enables to suppress the neighboring resonance mode and achieve an ultra-high FSR at the target wavelength region. These results could be useful in analyses of other similar plasmonic filter designs with side-coupled structures, and demonstrate the potentials for applications in future optical integrated wavelength selectors or filters with an ultra-wide FSR.

Chapter 5 Slab space optics

In this chapter, the results of slab space optics are introduced. The following three contents are introduced, which are a kind of 2D planar chiral meta-materials, grating couplers for vertical fiber-chip coupling, and curved silica in slab space optics. The first research is an independent results from this thesis, while shows interesting results. The optical activity based 2D chiral meta-materials can be works as optical filters and be potential components of near infrared optical imaging systems. The second part, grating couplers, sever as the flow of the thesis. The grating coupler can be used for non-touched and flexible interconnection components of fibers and silicon or plasmonic chip, i.e. I/O. The third sub-chapter studies the basic characteristics of slab space optics in an example of curved silica mirrors. A kind of waveguide crossing parts is studied. An potential usage of inter-connectors between integrated lasers diodes and silicon waveguides is also studied.

The outline of this chapter is introduced as follows. In chapter 5.1, the 2D planar chiral meta-materials is introduced. The basic results of optical activity and filtering characteristics based on OA is introduced. The analysis methods of 3D-FDTD and eigen-vectors of Jones matrix is then introduced. The results show that the tuneable of filtering characteristics come from the guided-mode resonances and Fabry-Perot resonances. The results of different subscript materials are also investigated. In chapter 5.2, a kind of dual-layer grating coupler is analyzed for vertical coupling between fibers and silicon waveguides. Due to the structures of dual-layer design and phase matching conditions of diffracted waves by gratings and guided waves in silicon waveguides, coupling of dual-polarization states and dual-optical bands are achieved at the first time. The two-layers Fabry-Perot resonances are also investigated for high coupling efficiency. In chapter 5.3, silicon slab space optics is investigated using curved silica mirrors. A king of waveguide crossing coupler is the studied with high transmission loss (i.e. low insertion loss), low crosstalk, and broad bandwidth. The results of radiation modes of terminated slab waveguides and Goos-Hanchen shift

are discussed. In chapter 5.4, a kind of laser-waveguide inter-connector is discussed. Applying the ABCD's law, the reflected Gaussian beams are reformed and re-located. The coupling of reflected beams with adiabatic taper is also introduced. In chapter 5.5, the summary is given based on the above analysis.

5.1 2D planar meta-material

The potential application of planar chiral metamaterials (PCMs) are investigated for near infrared wavelength (wavelength from 1000nm) imaging systems. The application could be used for multispectral measurement based on arrayed PCMs (i.e. planar chiral nano gratings, PCNG). The optical activity of PCMs is investigated first. The optical activity generated by guided mode resonance (GMR) and Fabry-Perot resonance are clear by the analysis methods of 3D-FDTD and calculation of eigenvectors of Jones matrix. The wavelength filtering characteristics are analyzed with different bandwidths and verified for different underclad materials, like Si_3N_4, Al_2O_3, and Si.

5.1.1 Optical activity

The introduction of optical activity is shown first in this sub-chapter. Optical activity (OA), is also known as optical rotation, which refers the rotation of optical beams or alter the polarization state of beams. The research of optical activity comes from the rotation of beams passing through sucrose solutions and other stones, which have molecular chirality. Chirality means the structure of a molecule is not identical to its mirror image. Such materials have the characteristics of circular dichroism (CD), which is also known as circular birefringence. Corresponding concept, such as linear birefringence, is quite familiar for researchers. Circular birefringence means that the response of the molecular are different for two eigenvectors of left-handed circular polarization state and right-handed circular polarization state. The basic theory of optical activity is introduced as follows.

The refractive index n of a material refers the phase velocity of light in the

medium for the understanding of linear polarized waves. It's quite known that the linear polarized waves can be superposited by a set of left- and right-handed circular polarized waves in equal proportion. The phase difference of two circular polarized waves are independent and determines the direction of the composed linear polarized waves. The equation is shown as follows:

$$E_{linear,\theta_0} = \frac{\sqrt{2}}{2}(e^{-i\theta_0}E_{RHC} + e^{i\theta_0}E_{LHC}) \tag{5.1}$$

where E_{linear} and E_{RHC} and E_{LHC} are the representation of linear polarized waves and left- and right-handed polarized waves, respectively. The E_{RHC} and E_{LHC} can be written in the terms of the *x* and *y* components as follows:

$$E_{RHC} = \frac{\sqrt{2}}{2}(\hat{x} + i\hat{y}) \tag{5.2a}$$

$$E_{LHC} = \frac{\sqrt{2}}{2}(\hat{x} - i\hat{y}) \tag{5.2b}$$

where x and y are unit vectors and *i* is the imaginary unit.

Substituting these equations into E_{RHC} and E_{LHC} for E_{linear}, the following equation can be obtained.

$$E_{\theta 0} = \frac{\sqrt{2}}{2}(e^{-i\theta_0}E_{RHC} + e^{i\theta_0}E_{LHC}) = \hat{x}\cos(\theta_0) + \hat{y}\sin(\theta_0) \tag{5.3}$$

Using the same equations, the following equation can be found:

$$E_{\theta 0} = \hat{x}\cos(\theta_0 + \Delta\theta) + \hat{y}\sin(\theta_0 + \Delta\theta) \tag{5.4}$$

This equation represents the for an incoming linear polarized wave with an angle of θ_0, it will be rotated by an angle of $\Delta\theta$ after passing through the medium.

Generally, the optical activity is weak and dependent on wavelength. In most case, optical activity is limited in a small wavelength range where the rotation angle of optical beams can become 90 degree. Thus, the usage of such limited OA peak for the application of polarization interferometer, a kind of band pass filter (BPF) can be realized. The research of artificial planar chiral mete-materials is first reported with giant circular birefringence, i.e. optical activity (OA) and is soon be optimized for larger birefringence. However, the application of PCM is not mentioned yet. In this research, the aim is to propose the multi-spectral imaging system based on modified planar chiral mete-materials.

5.1.2 Analysis methods

The schematic geometry of the PCM based imaging system is shown in Fig. 5.1, where the multi-patterened PCMs are sandwiched by two orthogonal linear polarizer.

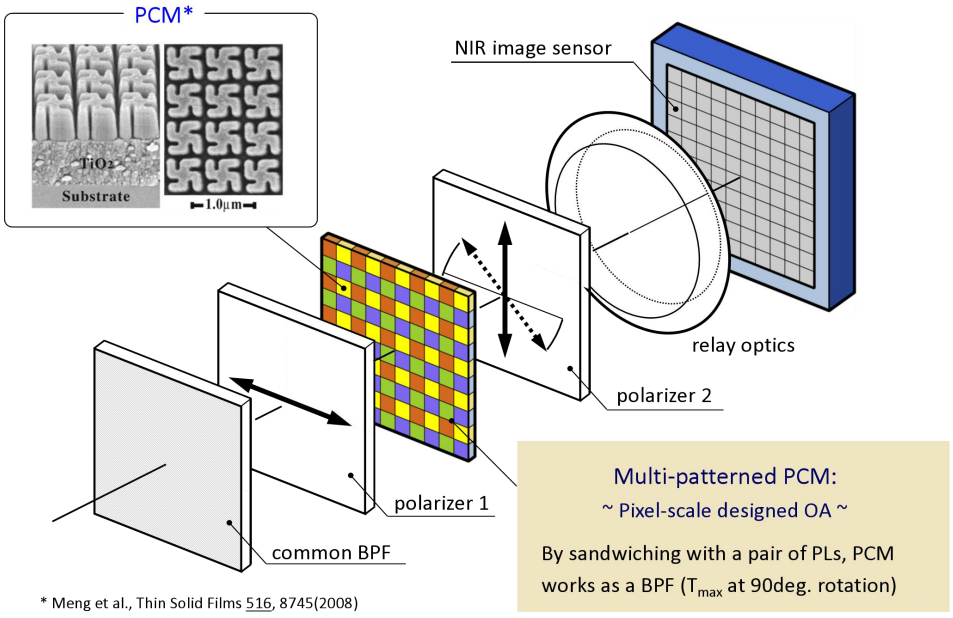

Fig. 5.1 Schematic of a multispectral imaging system using the polarization interference type band-pass filter array.

In the following sections, the basic structure and the method of numerical calculation are first explained. Then, the optical characteristics of various layer material and grating periods will be presented. In Ref. [113], it is shown that the optical activity is helped to be widen the band width with underclad layer having intermediate refractive index. Following their lines, the effect of such underclad are investigated to search practically useful BPF constructions.

A schematic view from top of the PCM is shown in Fig. 5.2 (a) along with the view from the cross-section in Fig 5.2 (b). A Silicon (Si) chiral layer (parameters of which are defined with thickness d_{chiral} and refractive index n = 3.5) and an underclad layer (parameters are the thickness d_{clad} and refractive index n_{clad}) are formed on a silica substrate with a refractive index of 1.444. An array of the proposed gammadion pattern is assumed to be formed on both bi-directions on the Si layer. The pattern is

arranged with a geometry of square lattice in the *x* and *y* directions with a pitch period of Λ. The width and the spacing range of the gammadion arms, represented by w_a and w_s, were both set as Λ/6, respectively. Only the convex pattern is dealt (emboss gammadion shape), as the concave one is calculated to behave only narrow OA peaks according to the previous study [114]. The materials are assumed to be lossless and non-dispersive for the reduction of complexity of calculation. Light of plane wave is assumed to be launched normally (parallel to the z axis) on the substrate from air.

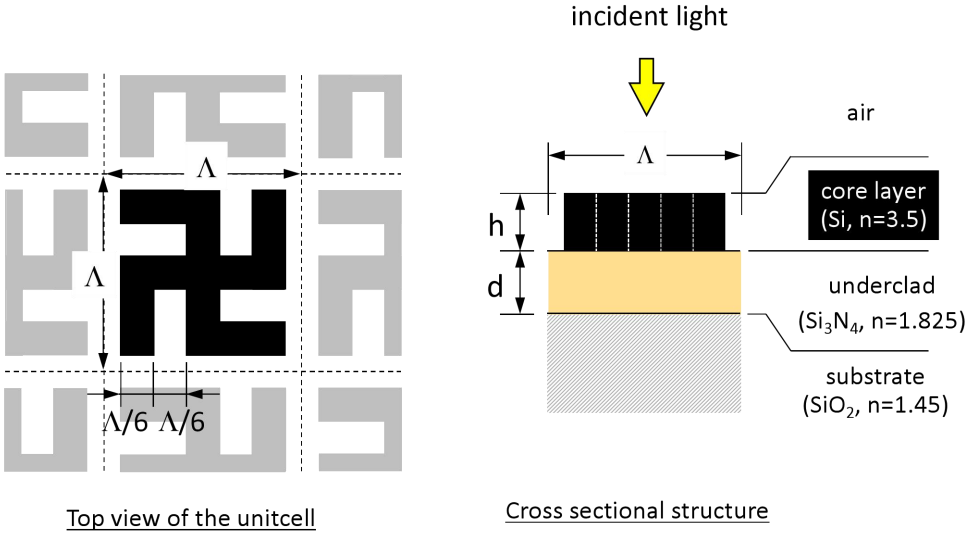

Fig. 5.2 Schematic view of the planar-chiral meta-materials from the view of (a) top and (b) cross section.

The results of Jones matrix of are calculated from the transmission spectrum of both the x, y-polarization incidence, details are listed in [114], which is not shown here. In a conclusion, the waveform of the 0^{th}-order spatial component of the transmitted waves, which are calculated by the 3D-FDTD simulation, are monitored. The simulation domain only contains one grating period with the continuous periodic boundary conditions on the *xz* and *yz* plane for simplification the calculation time. The ends of the *z* direction are set to the perfect matched layer (PML) for non-reflection [117]. The monitored time-domain waveform is then calculated by Fourier transformation to get the complex vector $[a(\lambda), b(\lambda)]^T$ (T denotes transpose). The y-polarized vector could be obtained as $[-b(\lambda), a(\lambda)]^T$, since the PCM gives a

four-fold rotational (C4) symmetry. Then, the Jones matrix (G) is obtained as follows.

$$G = \begin{pmatrix} a & -b \\ b & a \end{pmatrix} \tag{5.5}$$

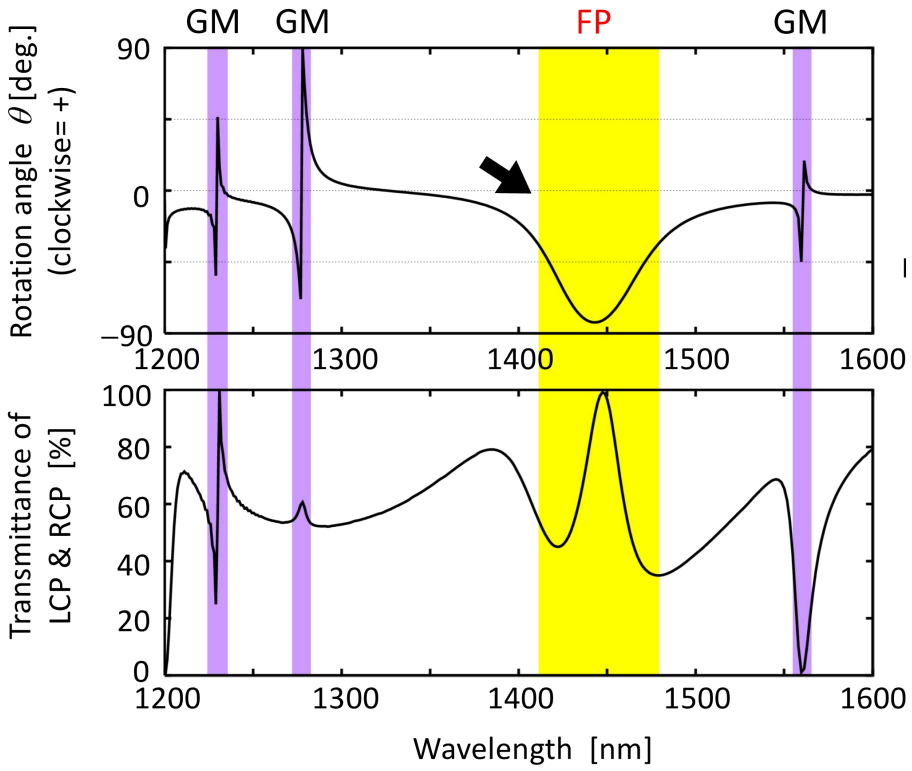

Fig. 5.3 Calculation results of the (a) rotation angle and (b) transmittance of LCP and RCP of the planar-chiral meta-materials as a function of wavelength.

For the region of the long wavelength ($\lambda > \Lambda/n_{clad}$), where the 1st-order diffracted waves are cutoff, the eigen-states of polarization of PCM are left- (LCP) and right-handed circular polarizations (RCP) [117]. Thus, the amplitude and the phase of the eigenvalues are related to the transmission coefficient and the phase retardation, respectively. Then the rotation angle for a linearly polarized incident light could be calculated by half of the difference of the phase of two polarized transmitted waves.

The spectrum response of the transmittance and rotation angle of PCM are shown in Fig. 5.3 (a) and (b), respectively. Two kinds of resonance phenomena are listed in the figures, which are guided-mode resonance (GMR) (comes from the lateral waves [118]) and Fabry-Perot resonance. The optical activity appears with the appearance of the two resonances. The principle of resonance of PCM is still unclear, which would

not be discussed here. The bandwidth of transmittance of FP resonance is quite wider than that of GMR, which is prefer in the usage of imaging system.

5.1.3 Results of multi-patterened PCM as BPF

The transmission spectrum of the multi-patterened PCM for different underclad are examined. Figs. 5.4(a) and (b) show the results of Si_3N_4 and Al_2O_3 as the underclad, where the depth of each underclad layer are 550 nm and 900 nm, respectively. The silicon chiral layer with gammadion shapes are both set to 500 nm. The wavelength range is focused from 1100 nm to 1800 nm. It's clear seen that the peak wavelength shifts with the linear relation as the increasing of the pitch period. There are two kinds of wavelength peaks appeared on the figures, marked by GMR and FP, which are explained in the previous chapter. As it's mentioned before, the resonance peak with principle of FP resonance gives a wider bandwidth, thus the results of GMR are not discussed here. The wavelength shifting coverage of the underclad of Si_3N_4 could be larger than 550 nm. The bandwidth of FP resonance are in a range of 21 and 32 nm. The peak transmittance could be from 76% to 93%, which are enough high values. It's clear that the characteristic of double peaks are not advantaged in the realistic application, for which the wavelength peak of GMR may give unwanted noise, however it's still proved to be useful [119].

On the other hand, the results of Al_2O_3 as the underclad are also concluded here, which is shown in Fig. 5.4 (b). Here, a slightly lower-index underclad of Al_2O_3 (n = 1.61) is used instead of Si_3N_4 (n = 1.9). There is also a double peak spectra, however, the peak of GMR could be negligible at the longer wavelength range. The bandwidths of the FP peak for different values of pitch period are located from 14 nm to 19 nm, which are narrower than the previous results. The peak transmittance are varied from 48% to 84% according to different pitch period. Both the two different underclad could be used to meet the demands of realistic usage.

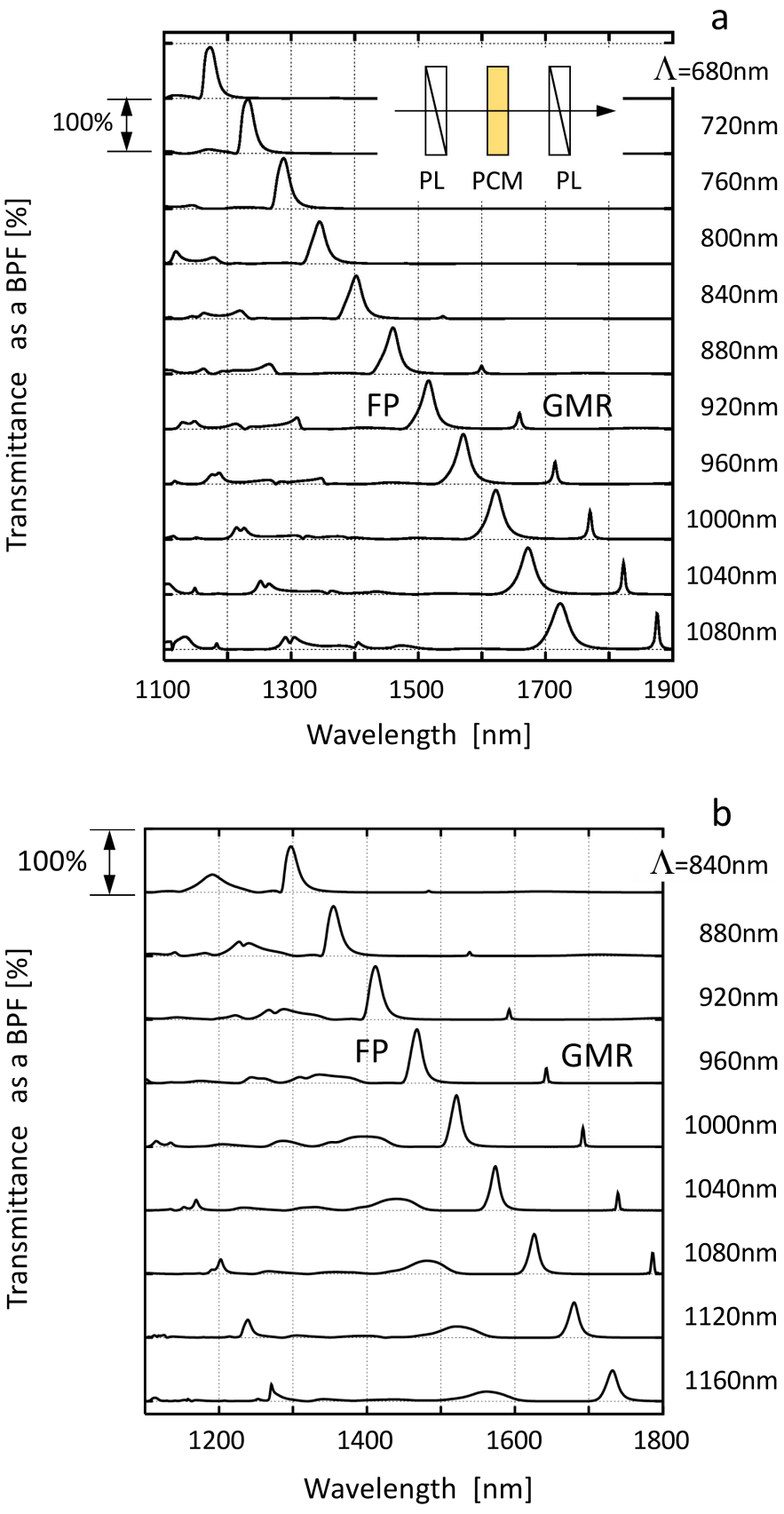

Fig. 5.4 Calculation filtering results of the multi-patterened PCMs as a function of wavelength for different pitch size using (a) Si_3N_4 and (b) Al_2O_3 as the substrates.

5.2 Grating coupler for vertical fiber-chip coupling

Grating couplers (GCs) serves as the interconnection of fibers and silicon waveguides for their huge geometry difference. Besides, grating couplers, inverse tapers are another choice for the connection between fibers and waveguides. However, grating couplers own merits in many parts, for example, easy assembly with fibers, none touch etc. The grating theories are first introduced, including grating equations and diffracted waves by gratings. Then a dual-layer grating coupler is designed and optimized. The phase matching conditions of diffracted waves by gratings and guided waves in waveguides are studied for effectively coupling. The transmission characteristics are studied. Results show that the design work as a dual-polarization state and dual-optical bands at the first. A dual-layer Fabry-Perot resonance is also investigated for high transmission efficiency.

5.2.1 Grating theory

Gratings, which are known as the periodic structures of series of identical units with the same rules of arrangements and orientation. One dimensional (1D) multi-slit grating is the simplest case as shown in Fig. 5.5, where different orders of waves are diffracted to different locations on the right monitor with different diffraction intensity.

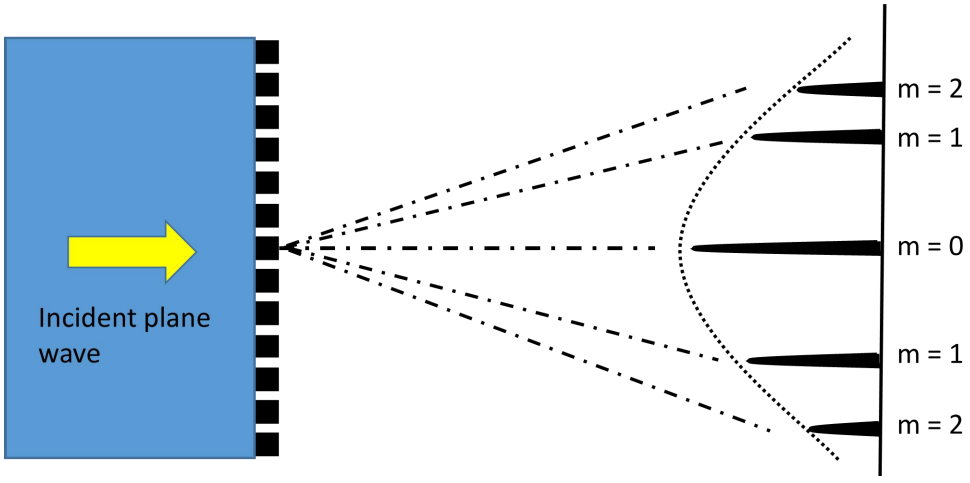

Fig. 5.5 Diffraction model of the one-dimensional grating.

The dielectric function of a sinusoidal grating is shown as the Eq. (5-6):

$$\varepsilon_r(\vec{r}) = \varepsilon_{r,avg} + \Delta\varepsilon\cos(\vec{K} \bullet \vec{r}) \tag{5.6}$$

A wave propagation through the grating makes on the same symmetry.

$$E(\vec{r}) = A(\vec{r})e^{-j\vec{k}\bullet\vec{r}} = A\varepsilon_{r,avg}e^{-j\vec{k}\bullet\vec{r}} + A\frac{\Delta\varepsilon}{2}e^{-j(\vec{k}_{inc}-\vec{K})\bullet\vec{r}} + A\varepsilon e^{-j(\vec{k}_{inc}+\vec{K})\bullet\vec{r}} + \ldots \tag{5.7}$$

The first part is known as the zeroth order of diffracted waves. The same order is applied on the following parts, which are known as the first and second order of diffracted waves. In Fig. 5.6, it shows that the applied waves split into three waves. Each of those splits into three waves as well. And each of these splits follows the same rules.

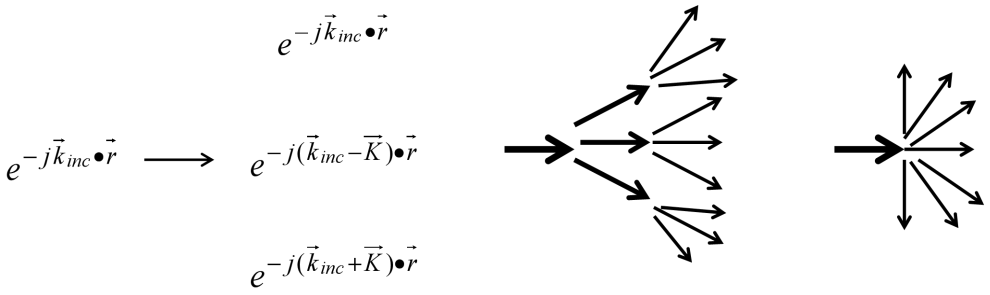

Fig. 5.6 Diffracted order of waves.

The total set of allowed diffraction orders is described in the Eq. (5.8).

$$\vec{k}(m) = \vec{k}_{inc} - \vec{K} \tag{5.8}$$

The boundary conditions require the tangential component of the wave vector be continuous. The wave is entering a grating, so the phase matching condition is:

$$k_x(m) = k_{x,inc} - mK_x \tag{5.9}$$

The longitudinal vector component is calculated from the dispersion relation.

$$k_z^2(m) = (k_0 n_{avg})^2 - k_x^2(m) \tag{5.10}$$

For large *m*, $k_z(m)$ can actually become imaginary. This indicates that the highest diffraction-orders are evanescent, which will be discussed in later. Thus, the grating equation is obtained by the following equation.

$$n_{avg}\sin[\theta(m)] = n_{inc}\sin(\theta_{inc}) - m\frac{\lambda}{\Lambda} \tag{5.11}$$

where Λ is the pitch of grating periods. The image of diffraction by gratings with substrate is shown in the following figure.

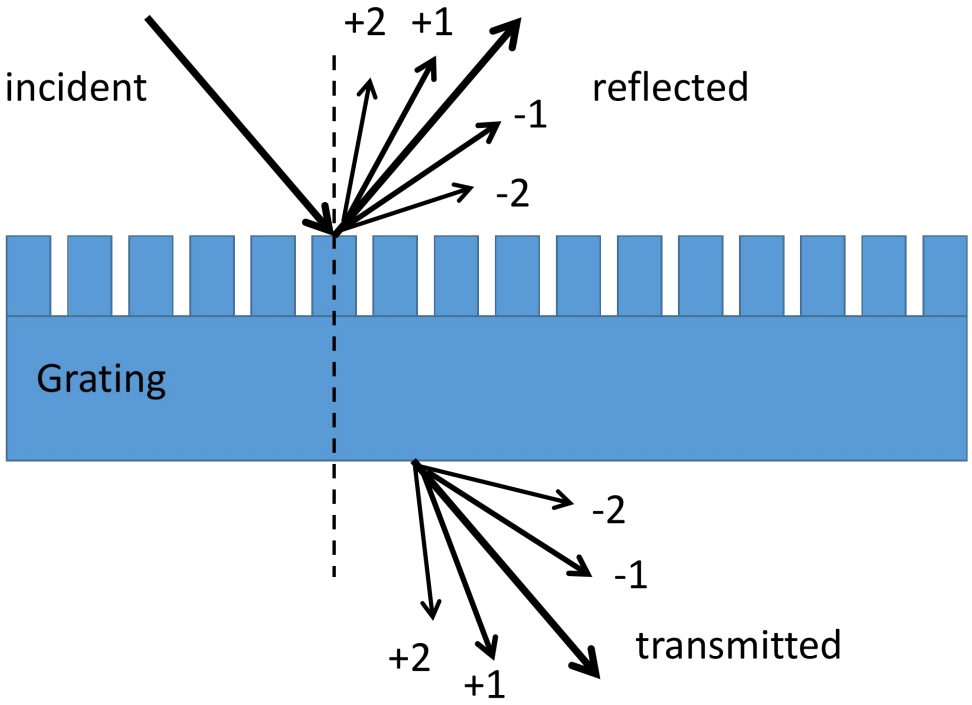

Fig. 5.7 Diffraction of grating with substrate.

5.2.2 Grating couplers for fiber-waveguide coupling

The research background of grating couplers for fiber-waveguide coupling is first introduced. As it's introduced in the previous chapter, photonic integrated chips (PICs) with a submicrometer size based on a silicon-on-insulator (SOI) platform attracted much attention at the beginning of this century to meet the growing demands of data rate. [120-121] Various active and passive devices have been developed on the platform, such as optical switches, [122-123] modulators, [25, 124] lasers, [125-126] and polarization splitters. [127] Integrated photonic waveguides have also proved to be potential techniques for photonic quantum information experiments, such as entangled photon sources and buffers. [128-129] Although high integration benefits from the small size, connecting PICs with single-mode fibers (approximate core size of 10 μm) is still a problem.

Generally, there are two ways to achieve data transmission between PICs and

fibers: inverse tapers and grating couplers (GCs). The former group, which relies on adiabatically expanding silicon waveguide modes through a taper to match with a fiber, provides total communication; however, a perfect connection between the cross sections of the taper end and fiber is necessary. In addition, an taper length (several hundreds of micrometers) is needed to adiabatically convert fiber modes to waveguide modes. [130-131] GC, with out-of-plane coupling, is another popular device for efficient coupling between fibers and waveguides. Considering one-dimensional (1D) gratings with high wavelength and polarization sensitivities, several kinds of GCs are demonstrated at the specific wavelength and polarization state. [132-136] To achieve polarization diversity, two-dimensional (2D) gratings are a promising solution, studied in both theory and experiments. [137-140] However, 2D gratings couple orthogonal polarization states of a single mode fiber to the same waveguide mode; moreover, the optimization and fabrication of 2D gratings are also a complex work.

Tilted incidence, instead of normal incidence, is a popular choice to avoid the polarization and wavelength sensitivities. With a proper design of grating parameters and fiber tilted angles, phase-matching conditions can be satisfied between the propagation modes of waveguides and fibers. Tang et al. developed a polarization separation GC for transverse-electric (TE) and transverse-magnetic (TM) polarization at 1.55 μm. [141] Streshinsky et al. designed a 2D biwavelength polarization-splitting GC. [142] Nambiar et al. have recently reported a dual-band unidirectional GC for TE polarization based on a SiN platform. [143] However, in these cases, coupling efficiency is quite sensitive to the tilted angle, which leads to extra cost of the mounting of fibers and GCs. Instead of tilted fibers, Wang et al. reported a tilted grating. [144] However, the fabrication complexity makes it difficult to apply in the commercial packaging. To ensure vertical coupling, gratings with asymmetric trapezoidal holes and dual-etched types have also been investigated. [145-148] Although perfect vertical coupling, high efficiency, and broadband have been achieved, the coupling was limited at a specific wavelength and polarization. To balance the vertical coupling, polarization and wavelength diversity are still the main problems in recent research.

In this work, a dual-layer GC consisting of two 1D gratings was proposed for perfect vertical fiber–chip coupling with both wavelength and polarization diversity. The first grating was designed with a long period and deep-etch depth to function as a beam splitter, which could efficiently convert vertical incident fiber waves into tilted diffracted waves. The second grating was designed with a short period and shadow-etch depth to diffract the tilted waves a second time. By properly designing the parameters of two gratings and silicon waveguides, phase-matching conditions for normal incident waves and waveguide modes can be satisfied. A dual-layer grating equation accompanied by finite-difference time-domain (FDTD) simulations was applied to verify the correctness of the design. Results show that for TM-polarized waves at 1.32 μm, both TE- and TM-polarized waves at approximately 1.55 μm were effectively coupled from a single-mode fiber to waveguides through vertical incidence. To the best of the authors' knowledge, this research is the first report of a vertical incidence GC with characteristics of polarization and wavelength diversity.

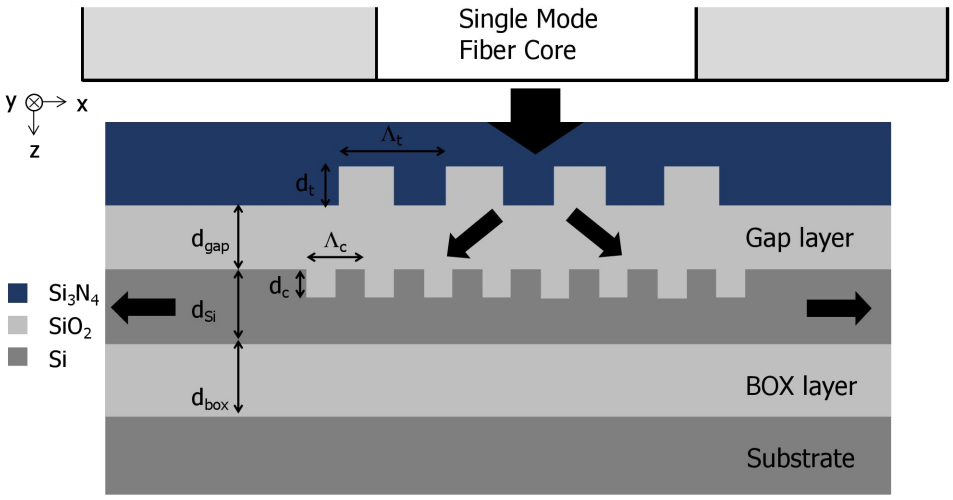

Fig. 5.8 Schematic of a dual-layer grating coupler for vertical coupling with a single-mode fiber and silicon slab waveguide.

Fig. 5.8 shows the schematic of the proposed dual-layer GC for vertical coupling with a single-mode fiber. The first top-grating, which functions as a beam splitter, was designed with a long period and deep-etch depth. Low-index difference materials of

Si_3N_4 (n_{Si3N4} = 2) and SiO_2 (n_{SiO2} = 1.45) are applied in this grating for minimizing the effect of polarization and back-reflection. The pitch period and etch depth of the grating are represented by Λ_t and d_t, respectively. The second bottom-grating was designed with a short period and shadow-etch depth for splitting the beam again. This is done to satisfy the phase-matching conditions of silicon waveguides (with a height of d_{si}). The pitch period and etch depth of the grating are represented by Λ_c and d_c, respectively. The two gratings are separated by a SiO_2 gap layer with a height of d_{gap}. For simplification, both gratings were designed with duty cycles of 0.5. Si_3N_4 and SiO_2 were used as the top and bottom cladding layers. The whole device was established on a silicon substrate.

The working principle of the dual-layer GC is as follows. Incident beams with TE (electric field lies strictly along the *y* direction) and TM (magnetic field lies strictly along the *y* direction) polarization states from a single-mode fiber are diffracted in directions after they pass through the first grating. Then, when those tilted waves pass through the second grating, they are diffracted again to satisfy the propagation modes of silicon waveguides. Eqs. (5.12-1) and (5.12-2) represent the diffraction equations for the first and second grating, respectively.

$$k_0 * N_{eff\_t} = k_0 * n_{Si_3N_4} * \sin(\theta) - (\pm i)\frac{2\pi}{\Lambda_t} \tag{5.12-1}$$

$$k_0 * N_{eff\_c} = k_0 * N_{eff\_t} - (\pm i)\frac{2\pi}{\Lambda_c} \tag{5.12-2}$$

where $k_0 = 2\pi/\lambda$ is the free space wave number, N_{eff_t} and N_{eff_c} are the effective refractive indices of the diffracted waves by the first and second layer grating, respectively, n_{Si3N4} is the refractive index of silicon nitrite, θ is the incident angle of the single-mode fiber (θ = 0 for vertical incidence), i is the integer of diffraction order (usually i = 1), and Λ_t and Λ_c are grating periods of the first- and second-layer grating, respectively. By substituting θ = 0, i = 1, eliminating k_0 and medium variable N_{eff_t}, Eq. (5.13) is obtained for representing the dual-layer grating equation.

$$N_{eff\_c} = (\pm 1)\frac{\lambda}{\Lambda_t} + (\pm 1)\frac{\lambda}{\Lambda_c} \tag{5.13}$$

To perform effective coupling with diffracted waves and waveguides, N_{eff_c} from Eq. (5.13) should be satisfied with the propagation modes of waveguides. In a typical

silicon slab waveguide, shown in Fig. 5.8, guiding conditions are only determined by waveguide height $d_{si.}$ Thus, a proper design of a group of [Λ_t Λ_c d_{si}] is key. In addition, to achieve high coupling efficiencies, high diffraction efficiencies of two gratings are necessary. However, compared with the second shadow-etched grating, the first deep-etched grating shows more space for manipulation. Thus, before the results of the phase-matching conditions are presented, the characteristics of the first grating (beam splitter) are explained.

5.2.3 Transmission of dual-polarization state and dual-band

Because diffraction occurs equally on two directions with central mirror symmetry, it is enough to consider only a single side of the first grating. Figs. 5.9(a-d) represent the 2D-FDTD results of the normalized efficiency of the first-order diffracted waves of a single side (maximum efficiency is limited by 50%) as functions of Λ_t and d_t for TE and TM polarization at 1.3 and 1.55 μm, which are the most used optical bands. From those figures, it is clear that diffraction efficiency varies greatly with d_t and slightly with Λ_t. The diffraction behaves the same for TE and TM polarization at the same wavelength. Peak efficiency larger than 35% appeared at d_t = 1.23 and d_t = 1.48 μm for wavelengths at 1.3 and 1.55 μm, respectively. Although several higher-order diffracted waves appear with the increase of Λ_t, the principle of high efficiency can still be roughly explained as the minimum of the 0^{th} transmitted waves, leading to the enhancement of first-order diffracted waves. When the phase delay difference of the 0^{th}-order waves passing through the SiO_2 and Si_3N_4 equals a half wavelength, the deconstructed interference condition is satisfied, leading to the minimum of 0^{th}-order waves. Eq. (5.14) is used for the calculation of the condition of deconstructed interference.

$$n_{Si_3N_4} * d_t - n_{SiO_2} * d_t = n * \frac{\lambda}{2} \tag{5.14}$$

where n is an integer, and n_{Si3N4} and n_{SiO2} are the refractive indices of Si_3N_4 and SiO_2, respectively. The results from Eq. (5.14) represent d_t = 1.185 and 1.41 μm for wavelengths of 1.3 and 1.55 μm, respectively, which are approximately the values

shown in Figs. 5.10 (a-d). However, d_t must be considered a fixed value in the realistic design, indicating a trade-off for high efficiency at 1.3 and 1.55 μm. Next, the diffracted angle of the first-order diffracted waves is shown in Fig. 10. Again, for simplification, only a single side is considered. It is clear from the figures that diffracted angles only vary with Λ_t. The diffracted angles also behave the same for different polarization states at the same wavelength. Eq. (5.12) could be used to calculate the angles for verification. Little diversities may come from the calculation roughness. A high-efficiency transmission grating has now been successfully designed with controllable angles.

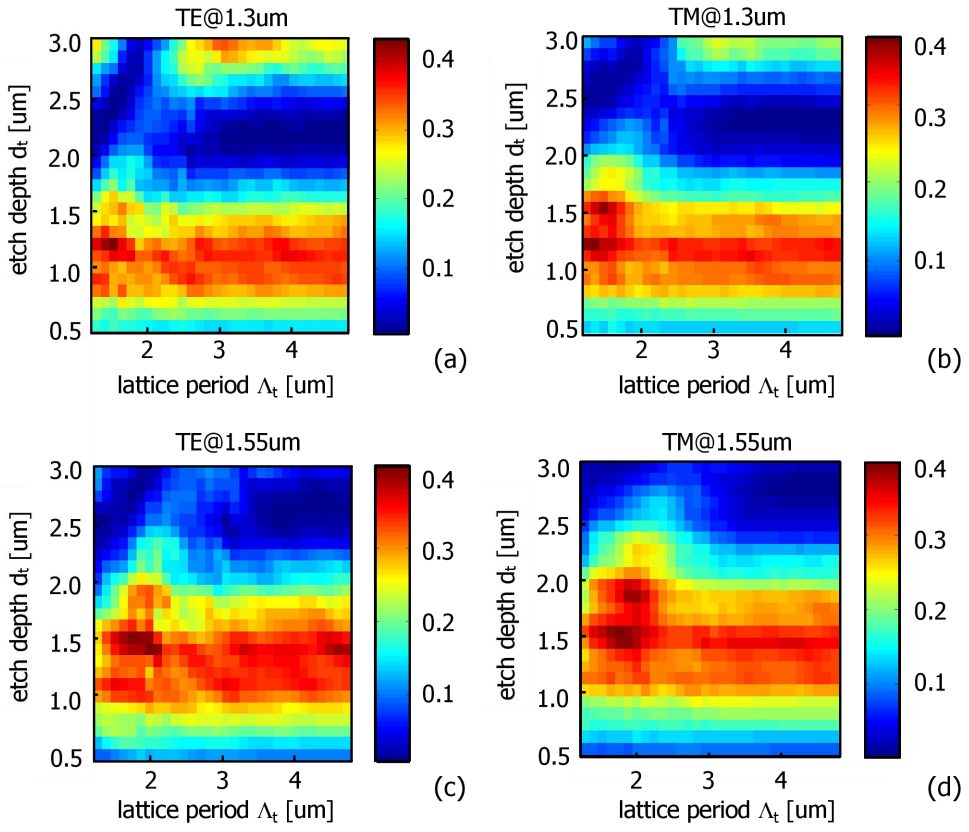

Fig. 5.9 Calculated normalized efficiencies of the 1st-order diffracted waves of the top grating as functions of Λ and d_t; (a) for TE at 1.3 um, (b) for TM at 1.3 um, and (c) for TE at 1.55 um, (d) for TM at 1.55 um. The maximum efficiency is limited by 50%.

To determine the phase-matching conditions, defined by a group of [Λ_t Λ_c d_{Si}], is the key work in this study. Fig. 5.11(a) shows one possible configuration of a

polarization separation design for one-side input (only the -1st-order diffracted waves generated by the first grating are considered). The waves diffracted by the second grating originally expect to design with the matching of waveguide modes of TM_0 and TE_1 at 1.3 and TE_0 and TM_0 at 1.55 μm. However, in further calculations, both conditions could not be satisfied simultaneously. Thus, the phase-matching condition of TE_1 at 1.3 μm is not taken into consideration in later work, because fundamental modes show more meanings. In addition, symmetric diffracted waves (+1st by the first grating) appeared on the other side. Fig. 5.11(b) shows the output characteristics for two sides' input and one port output. It is clear that TM_0 at 1.3 and TE_0 and TM_0 at 1.55 μm should output at one port. Meanwhile, the opposite port shows the same behaviors.

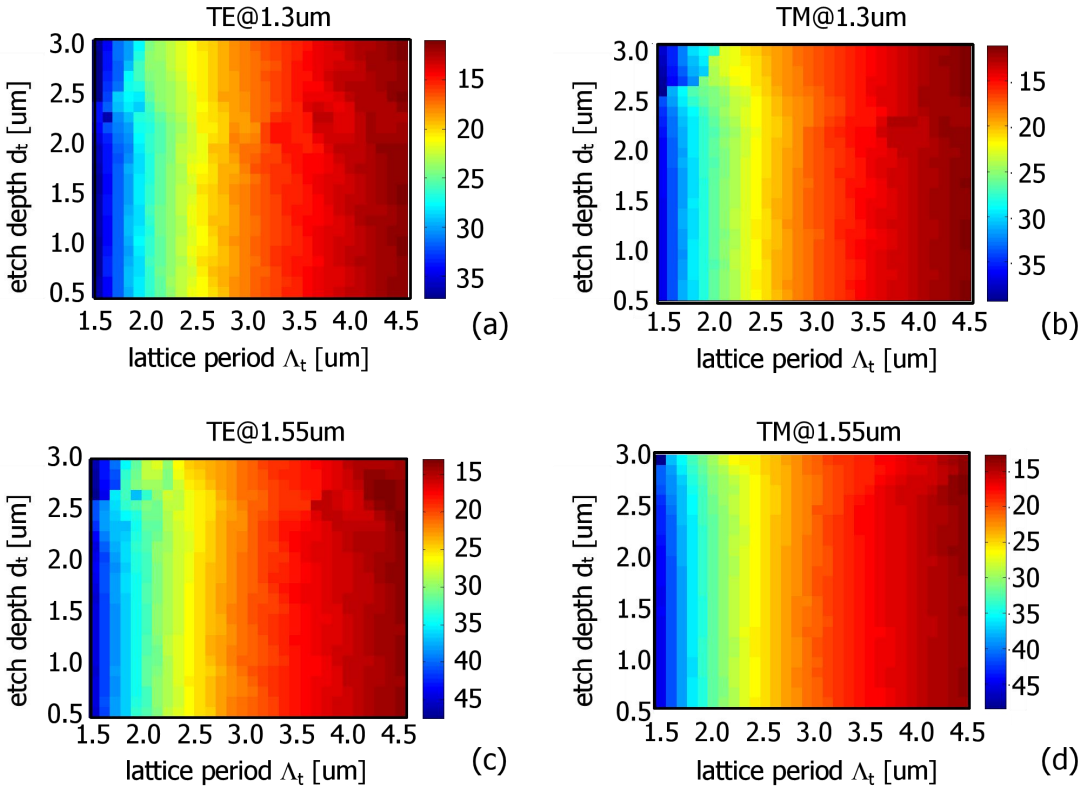

Fig. 5.10 Calculated angles (degree) of the 1st-order diffracted waves of the top grating as functions of Λ and d_t; (a) for TE at 1.3 um, (b) for TM at 1.3 um, and (c) for TE at 1.55 um, (d) for TM at 1.55 um.

According to the above analysis, the optimized values of Λ_t, Λ_c, and d_{Si} are set to 4.1, 0.63, and 0.26 μm. d_t is optimized to 1.3 μm to balance the efficiency of the first grating at both wavelengths. dc is set to 0.06 μm for a proper value.16) d_{gap} and d_{box} are both optimized with a value of 1.75 μm, as shown later. Fig. 5(a) shows the results of the phase-matching conditions described by Fig. 4(a). The results are calculated by Eq. (5-13) and dispersion relations of silicon slab waveguides with parameters mentioned above. In Fig. 5.12(a), real lines represent the effective refractive indices of $TE_{0,1}$ and $TM_{0,1}$ modes for a silicon slab waveguide. Dashed lines represent the effective refractive indices of the twice-diffracted waves shown in Fig. 5.11(a), where −1 and +1 represent the orders of −1st and +1st diffracted waves. The cross points represent the phase-matching conditions, marked by symbols A, B, C, and D. Because Point A does not match the design demand, only B, C, and D are considered. Symbol B can be described as the matching of the −1st-order waves diffracted the second time with the TM_0 guided mode at approximately 1.3 μm. The same explanation can be applied to Symbols C and D. Then, to verify the effectiveness of the design, a 2D-FDTD simulation is shown in Fig. 5.12(b). Four peaks can be observed, and they are marked in order of A to D. Each peak represents a corresponding cross-point in Fig. 5.12(a). Again, Peak A is not taken into consideration. Comparison of Figs. 5.12(a) and (b) shows that the design works as desired. Peak B represents the output of the TM_0 mode at 1.3223 μm with a normalized efficiency of 13.53% (27.06% for two ports) and a 3-dB bandwidth of 47 nm. Peaks C and D represent the output of the TE0 and TM0 modes at 1.5826 and 1.5625 μm with normalized efficiencies of 20.51% (41%) and 16.44% (32.88%) and 3-dB bandwidths of 49 and 34 nm, respectively. The distortion of the calculated wavelength and desired wavelength comes from the slight shift of phase-matching conditions (currently three) in the optimization, which would become unacceptable for four. The above results show a successful design of a dual-layer GC for the first time, giving both polarization- and wavelength-insensitive characteristics. The electric field for TE polarization and magnitude field for TM polarization give a Gaussian-field profile, indicating the fundamental modes, which are not shown here.

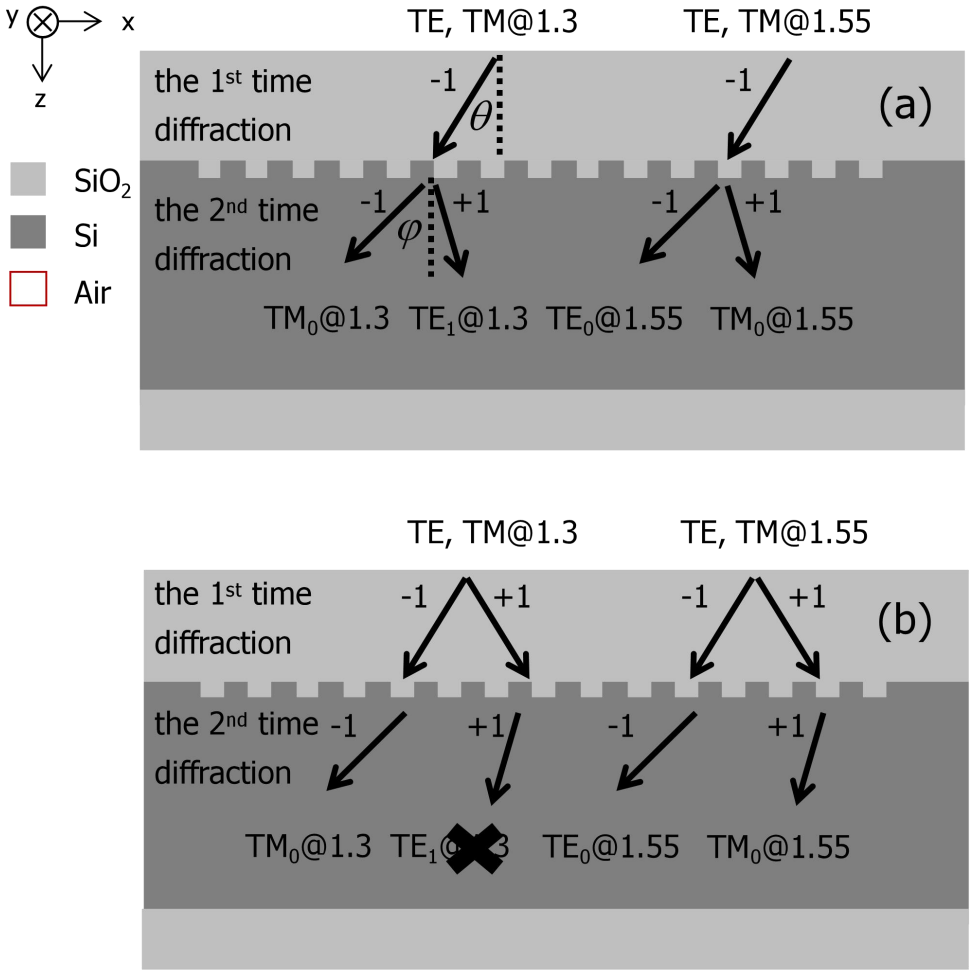

Fig. 5.11 Possible phase-matching conditions of the diffracted waves by the bottom grating and propagation modes of silicon slab waveguide; (a) for one side input and (b) for one port output. (TE_1 mode is not taken into consideration in the phase matching condition.)

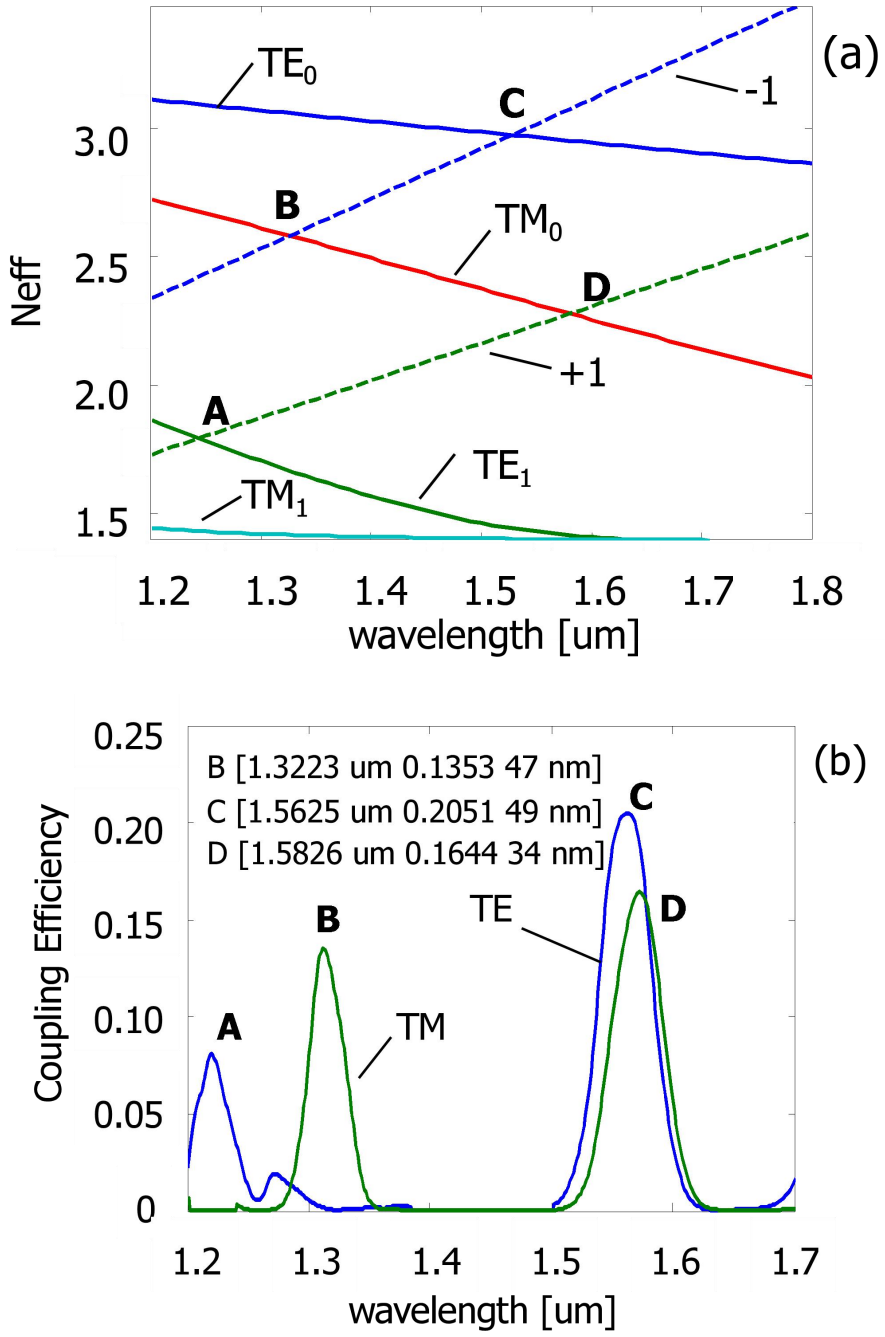

Fig. 5.12 Calculated phase-matching conditions as a function of wavelength described by Fig. 5.11; (a) theoretical results by Eq. (5-13) and dispersion relations of silicon waveguides with $[\Lambda_t\ \Lambda_c\ d_{Si}] = [4.1, 0.63, 0.26\ \text{um}]$ and (b) FDTD results.

5.2.4 Discussion of dual-layer FP resonance

We should also note that the total efficiencies of peaks B, C, and D depend on the depth of the gap layer (d_{gap}) and box layer (d_{box}). A kind of two-layer Fabry–Perot (FP)

interference is predicted at the two layers. High efficiency demands on the effective design of the depth of the two layers exist. Fig. 5.13 shows the calculated results of coupling efficiency for two ports (single port x2) for TE polarization at 1.55 μm as an example, where coupling efficiencies periodically vary with an increasing of d_{gap} and d_{box}, which confirms the hypothesis. Because the FP interference of light depends on wavelength, there is another trade-off to get high efficiency at 1.3 and 1.55 μm.

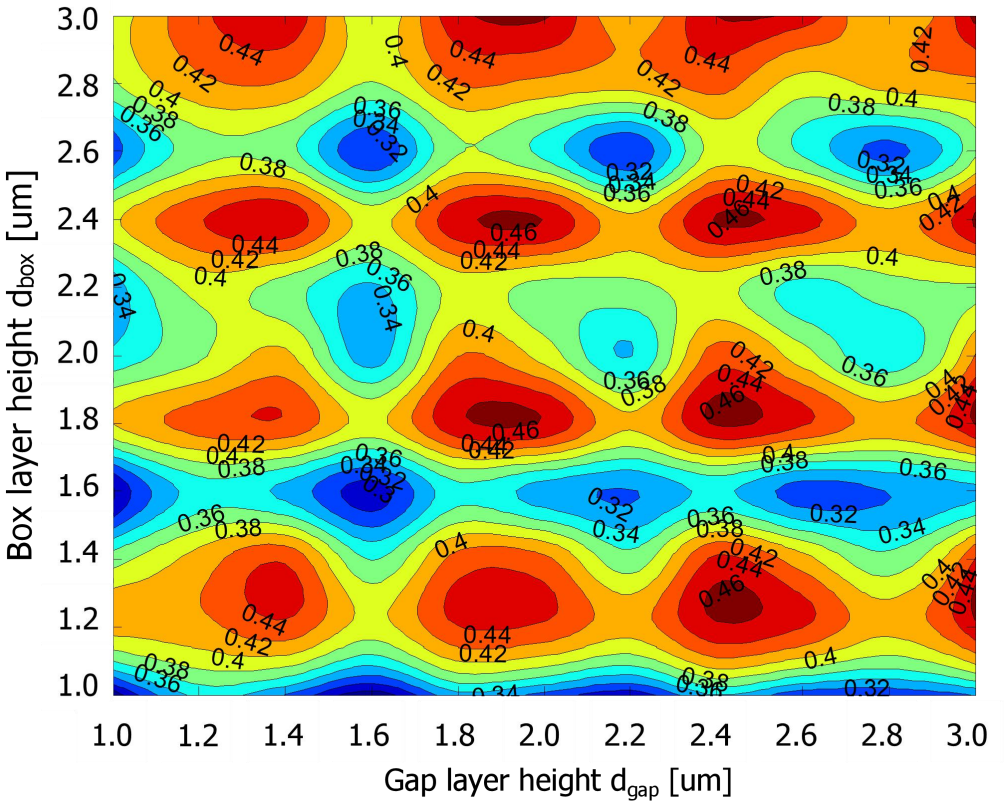

Fig. 5.13 Example of coupling efficiency (two ports) of a dual-layer Fabry-Perot resonance as functions of d_{gap} and d_{box} for TE polarization at 1.55 um.

5.2.5 Discussion of the evanescent coupling

The evanescent coupling of two gratings is roughly discussed in the sub-chapter. For effective evanescent coupling between two gratings, the following two conditions should be satisfied: (1). the period of the grating Λ is below the wavelength (subwavelength grating); (2). the distance between two grating d_{gap} is in a very close range. The two kinds of situations are shown on Fig. 5.14 for analysis, where (a) and

(b) emphasizing the transmission side of the first grating and the reflection side of the second grating, respectively. It's clear seen that evanescent waves only appear on the reflection side of the second grating. A rough derivation of Fig. 5.14 (b) is shown on Eq. (5.15), where θ is the diffraction angle, m is an integer, λ is the wavelength in medium, and Λ represents the period of two gratings.

$$\sin(\theta) = m\lambda / \Lambda \tag{5.15}$$

For λ (= 1.55 um/1.45 = 1.069 um) > Λ_c (= 0.63 um), sin(θ) > 1 and there is no real solution for θ, which indicates the evanescent waves. The complex electric field of evanescent waves is shown on Eq. (5.15) [150], where A_0 is the amplitude, b is the duty cycle of the grating (= 0.5), and k is the wave vector of the reflected waves in SiO_2.

$$\begin{aligned} E = & \\ & \frac{A_0 b}{2}\exp(-z\sqrt{((\frac{2\pi}{\Lambda_c})^2 - k^2)})\exp(-j\frac{2\pi}{\Lambda_c}x) \\ & + \frac{A_0 b}{2}\exp(-z\sqrt{((\frac{2\pi}{\Lambda_c})^2 - k^2)})\exp(j\frac{2\pi}{\Lambda_c}x) \end{aligned} \tag{5.16}$$

The first pattern and second pattern in Eq. (5.16) represent the opposite propagation directions along x. The calculated result of a single direction is shown on Fig. 5.15. It's clearly seen that the current d_{gap} (= 1.75 um) is enough for avoiding the evanescent coupling of the reflected waves. That's to say, the two gratings can be treated as separately and there is also no x-direction dependence of each grating, which enrich the freedom of fabrication.

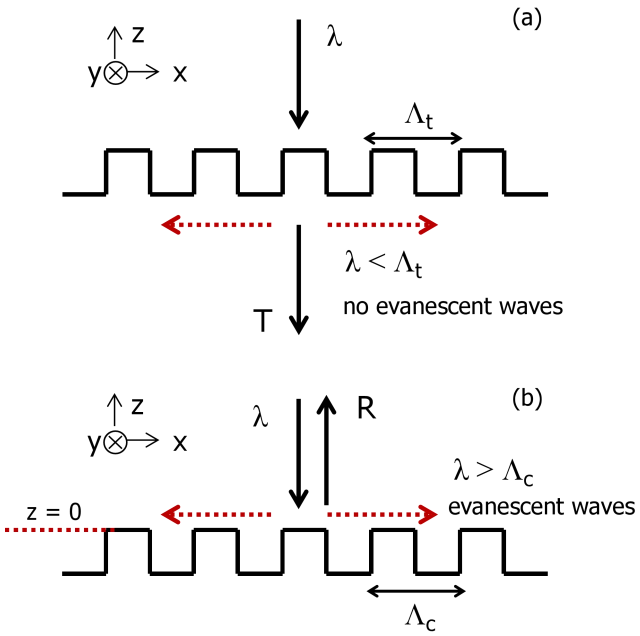

Fig. 5.14 Analytical model for evanescent waves of (a) transmission side of the first grating and (b) reflection side of the second grating.

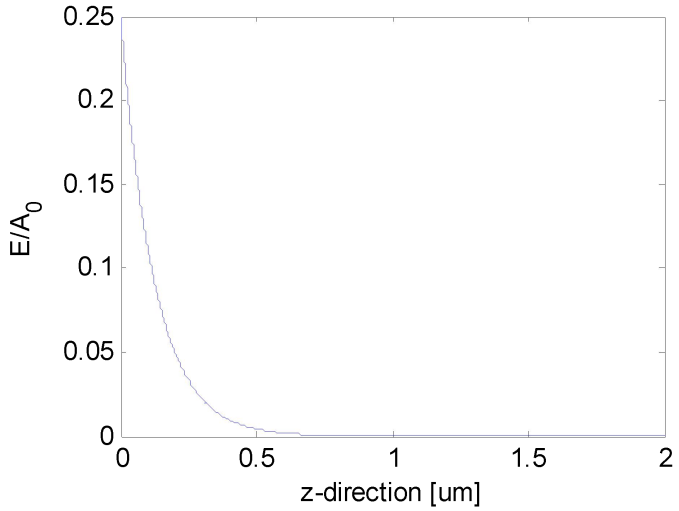

Fig. 5.15 Calculated result of decaying of evanescent waves shown in Fig. 5.14(b). z = 0 represents the top surface of the second grating.

5.3 Waveguide crossing based on curved silica-mirror

The slab space optics based waveguide crossing is introduced in the sub-chapter. The fundamental integrated optical components are studied based on waveguides for a long time. On the one hand, the chip's size is minimized; on the other hand, the

propagation loss of waveguides due to the roughness of side-walls are still occupy the position of main problems, which limits the large range application of optical devices. The concept of using silicon slab space come to overcome the demerit. The optical waves propagation in silicon space with only one direction confined and the other two directions propagated freely. In this case, the propagation loss can be reduced, while the controlling of optical waves becomes difficult. Thus, the controlling and manipulation of optical waves in silicon space is the main research work.

In this chapter, a kind of waveguide crossing is designed with the usage of curved of silica mirror. The waveguide crossing is inevitable in the designing of large scale optical integrated chips. The waveguide crossings based on MMIs and index-matched metamaterials [151-152] are studied a lot till now, which are shown in Fig. 5.16. However, the first one are strongly wavelength dependence and the second one is hard to fabricated. To reduce the insertion loss and crosstalk in a broadband wavelength range is still a problem. In this chapter, another kind of waveguide crossing based on the concept of slab space optics is introduced. In sub-chapter of 5.3.1, the structure is designed and introduced. From the sub-chapter of 5.3.2 to 5.3.4, the technical problems of the propagation of Gaussian beams, radiation of terminated slab waveguides and the effect of Goos-Hanchen shift are discussed. In sub-chapter of 5.3.5, the results are shown and discussed. Finally, in the sub-chapter of 5.3.6, the theory of the ABCD's lay is concluded.

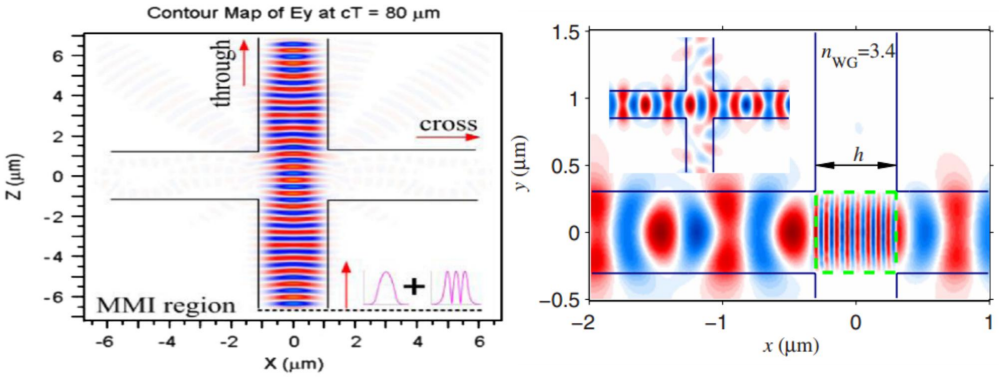

Fig. 5.16 Design of waveguide crossing based on (a) multi-mode interference and (b) high refractive index meta-materials.

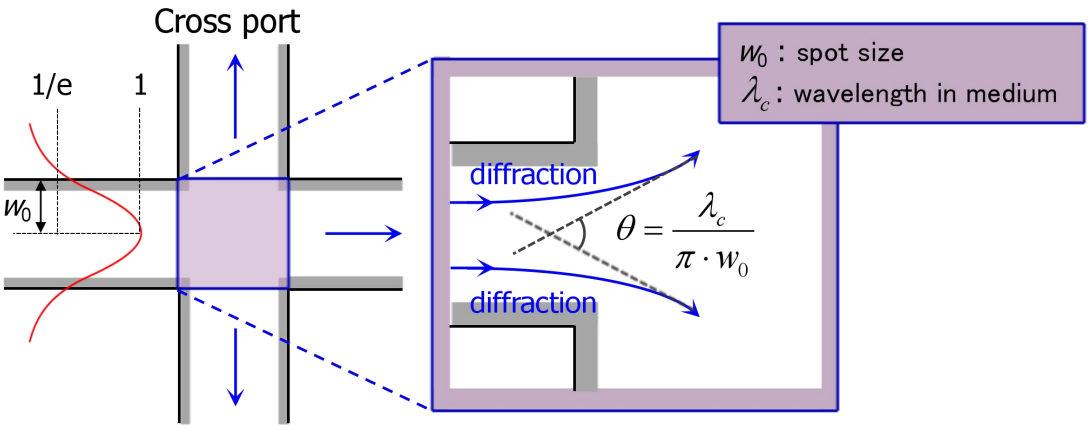

Fig. 5.17 Theoretical model of crosstalk by diffraction in waveguide crossing.

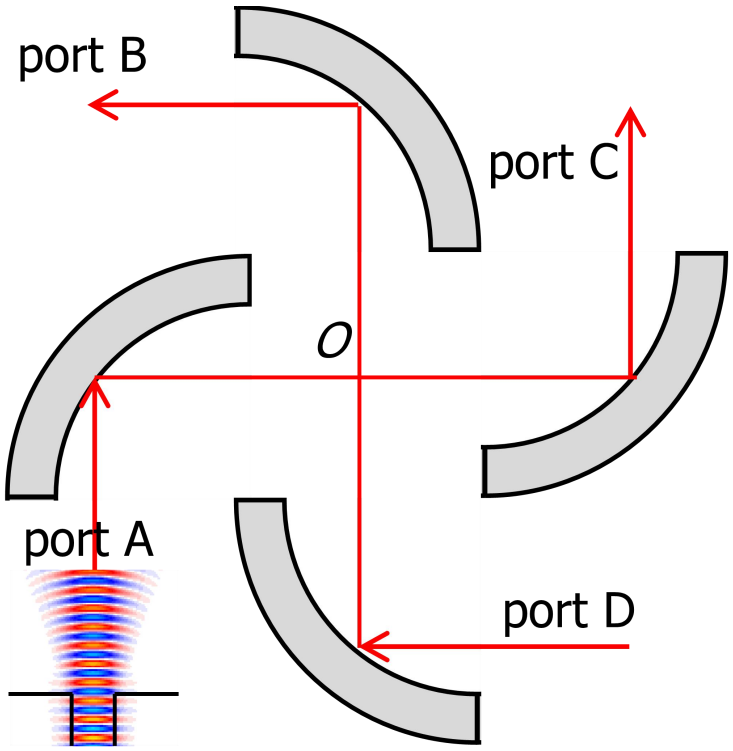

Fig. 5.18 Schematic of the 2D structures of waveguide crossing based on curved silica mirror and the concept of slab space optics.

5.3.1 Structure design

First, before presenting the results, the basic theory of the waveguide crossing is discussed and shown in Fig. 5.17. In the region of the waveguide crossing, the guiding condition of waves is destroyed, which make waves diffracted into the neighboring waveguide causing the crosstalk. The diffraction angle shows positive relation with the wavelength and negative relation with the waveguide width, which is shown in the figure. A larger diffraction angle means larger crosstalk, since the propagation is mainly towards the neighboring waveguides. Thus, to reduce the crosstalk, to reduce the wavelength in the medium or to increase the waveguide width are two possible ways.

The schematic design of the waveguide crossing is shown in the Fig. 5.18 with a 2D model. The four curved silica mirrors are arranged with the C4 rotation symmetry in a silicon space. Each silica mirror corresponds an input port, which is composed by a terminated waveguides with tapers to control the mode profile. In the following discussion, the function of taper is not discussed.

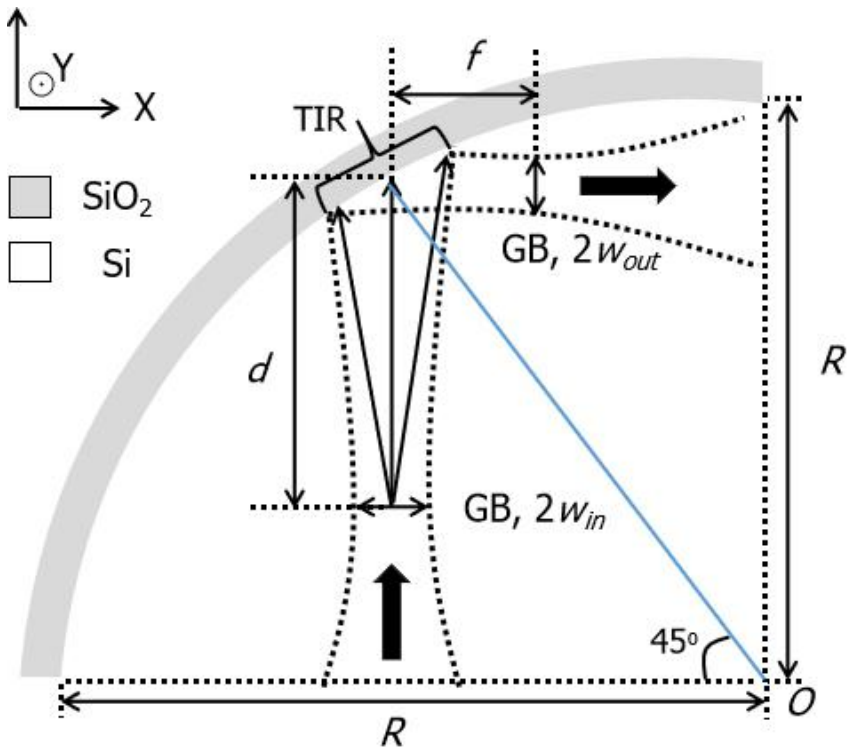

Fig. 5.19 Model of the reflection of Gaussian beams by curved silica mirrors.

The design concept can be explained in the following contexts. The optical waves propagate from the terminated waveguides into the silicon space with only one direction confined, while maintain the freedom of the direction of propagation and increase the freedom in another direction. The optical waves propagate in the silicon space and are reflected by the silica mirrors directly ahead. In our design, the input angle and reflected angle are both 45 degrees. Optical waves in the central space then become orthogonality and shown no crosstalk with each other. Those waves are reflected by another curved silica mirrors again and received by the waveguides. In this design, theoretical none crosstalk can be desired. The insertion loss can be extremely low with proper design of the positions of waveguides and mirrors. The bandwidth can also be enlarged since the reflection's law is not so sensitive comparing with the multimode interference. It's should note that the transmission and propagation of optical beams should be carefully controlled for low insertion loss and low crosstalk.

The model of the reflected waves by the curved silica mirrors is given in Fig. 5.19. The incident Gaussian beams with beam waist are launched from the bottom with an incident angle of 45 degree, which makes the reflected beams towards the $+x$ domain. The output position d_{out} and beam waist w_{out} can be represented by the d_{in} and w_{in}, which are the launch position and the beam waist of the incident Gaussian beams, respectively. The relation of them are followed by the ABCD's law, which will be discussed in the sub-chapter 5.3.6. The reflection is through the totally internal reflection.

The Fig. 5.20 displays the E_y field distribution of the simulated mirror. It's clear seen that the reflection behaves perfect as it's expected. However, due to the reflection mechanism is based on totally internal reflection, the Goos-Hanchen shift should be discussed as shown in the Fig. 5.20 (a). The propagation of the evanescent waves would influence the final performance of the device. On the other hand, the ABCD's law modifies the propagation and transformation of Gaussian beams, while they're still slightly different from the radiated waves from the waveguide ends. Thus, the two problems should be discussed before presenting the final results.

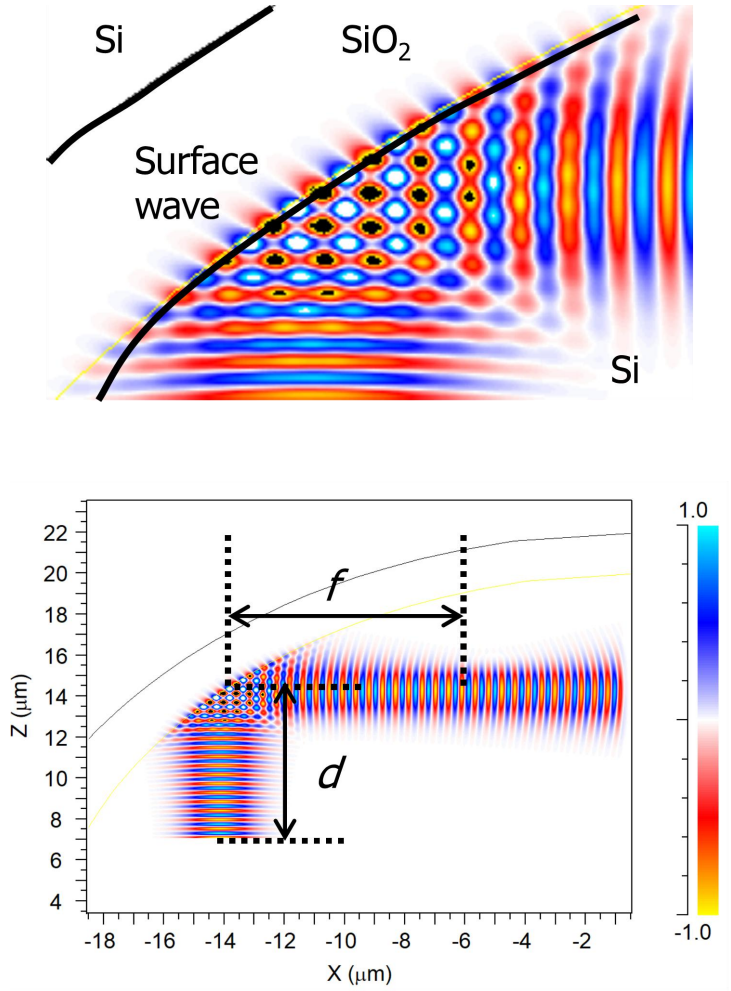

Fig. 5.20 Display of the E_y field distributions of (a) Magnified view of the propagation of evanescent waves on the Si and SiO_2 boundary and (b) overall view of the reflection, where the design satisfies $d = f$.

5.3.2 Radiation modes of terminated slab waveguides

The characteristics of transmission and reflection of optical beams is the main part in this research. Strictly speaking, the optical waves from the terminated slab waveguides are not the Gaussian beams, but more like the expanded sinusoidal function in free-space. Before strict interpretation, the overlap of optical waves from terminated waveguides and from Gaussian profile is calculated as an example. The overlap equation is shown as follow.

$$\eta = \frac{(\int f(x)g(x)dx)^2}{\int f(x)^2 \int g(x)^2 dx} \tag{5.17}$$

where *f(x)* and *g(x)* represent the electrical fields of optical waves with Gaussian profile and from terminated slab waveguides. In this calculation, the beam waist of input Gaussian beam is set to 2.085 um, while the slab width is a variable. The results that, after the same propagation distance, the maximum overlap value is larger than 99% at the width of slab waveguides of about 4.5 um. The results show that the mismatch of two waves are not so much and the using of Gaussian waves in the later calculation is possible and efficient. However, the strictly results of the terminated slab waveguides should be clearly. The problem can be simplified in the Fig. 5.23.

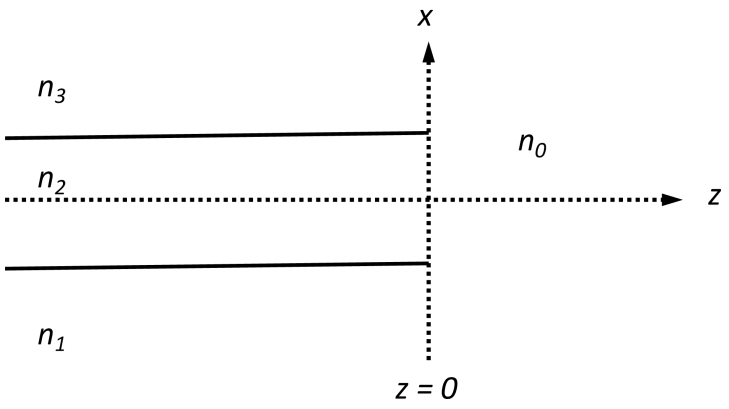

Fig. 5.23 Structure of an abruptly terminated asymmetrical slab waveguide.

In this figure, a three layer asymmetrical slab waveguide is shown in the zone of $z < 0$ and radiates in the homogeneous semi-infinite area of $z > 0$. The refractive index of the slab waveguide are consumed as n_1, n_2, and n_3, which obey the following rules $n_2 > n_1 > n_3$ for satisfying the total internal reflection in the waveguide. The semi-infinite homogeneous media is considered with a refractive index of n_0. It's clear that if $n_1 = n_3$, the slab waveguide is reduced into a symmetry case, which is discussed in the chapter 2. The electrical field in $z < 0$ (waveguide) region can be written as:

$$\Phi_1(x,z) = U_0(x)e^{-j\beta_0 x} + U_0 R_0 e^{j\beta_0 z} + \sum_{m=1}^{2} \int_{\rho_m}^{+\infty} R_m(\rho)\psi_m(x,\rho)e^{j\beta(\rho)z} d\rho \tag{5.18}$$

where

$$\beta^2(\rho) = k_0^2 n_1^2 - \rho^2 \tag{5.19}$$

The first term of the equation on the right-hand side represents the incident wave with an initial amplitude $U_0(x)$ and propagation constant β_0. The second and the third terms represent the reflected guided mode and the reflected radiation modes. For the semi-infinite region of $z > 0$, only the radiation pattern is considered. The electric field of this region can be written as a Fourier integral:

$$\Phi_{II}(x,z) = \sum_{l=1}^{2} \int_0^{+\infty} T_l(s)\phi_l(x,s)e^{-j\beta(s)z}ds \tag{5.20}$$

where $\beta^2(s) = k_0^2 n_0^2 - s^2$ and s is the wave-vector in the semi-infinite region. $T_1(s)$ and $T_2(s)$ are two unknown coefficients, which represent the transmission coefficients to be determined. $\phi_1(x,s) = (\frac{1}{\sqrt{\pi}})\cos(sx)$ and $\phi_2(x,s) = (\frac{1}{\sqrt{\pi}})\sin(sx)$ are the free-space eigenwaves satisfying the orthogonality relations. The calculation of $T_1(s)$ and $T_2(s)$ can be finished by FDTD simulation. According to the above analysis and results, the Gaussian beam is applied in the whole calculation instead of the complex waveguide mode. Using the Gaussian beam also make the establishment of theoretical easily.

The model to calculate the difference of the waves from the terminated slab waveguide and with a Gaussian shape is shown in Fig. 5.21. The fields from a terminated slab waveguide and with a Gaussian shape are launched from the same position and the overlapped power using Eq. (5-15) are calculated in Fig. 5.22, where both the two waves are propagated with the same distance. The beam waist of the Gaussian beams is fixed at 2.085 um (total width is 4.17 um), while the width of the slab waveguide is a variable value, which changes from 3.5 um to 5.5 um. The results shows that the difference of the Gaussian beams and radiated waves from the slab waveguide could be ignored. Thus, the following calculations are based on the Gaussian waves, which could be easily modified by the ABCD's law.

5.3.3 Gaussian beam transmission function

The transmission and reflection characteristics of Gaussian beams are verified by the ABCD's law. The 2D model of Gaussian beam incident on a curved silica mirror is shown in Fig. 5.19. The incident angle is assumed to be 45 degree. The beam waist of the incident and reflected Gaussian beam are represented by W_{in} and W_{out}, respectively. The distance of the incident Gaussian beam and the mirror is represented by d. The radius of the mirror is represented by R.

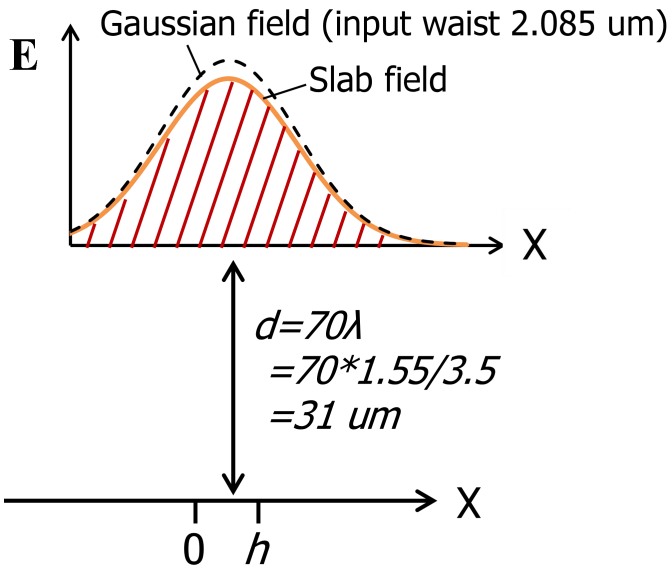

Fig. 5.21 Model of the difference of the Gaussian field used for simplification and radiated slab field in real case.

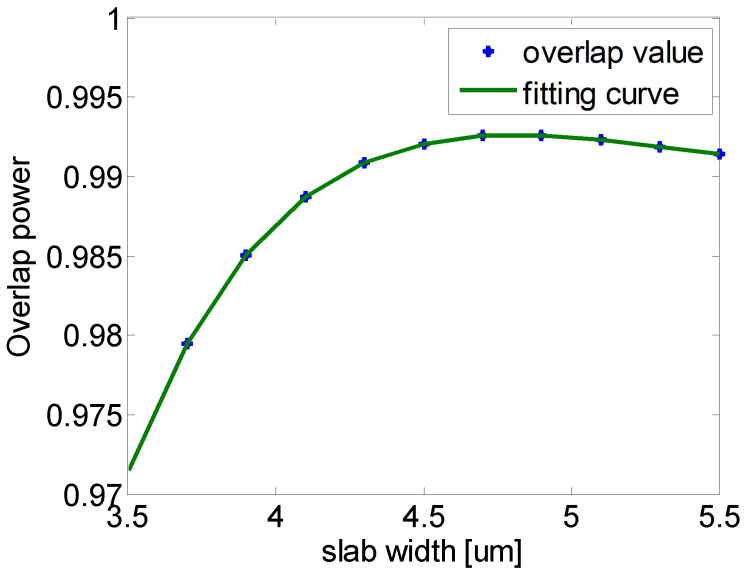

`Fig. 5.22 Calculation results of the overlap power of the radiated slab field and Gaussian field as a function of slab width.

According to the ABCS's law, the focus length and the relation of the w_{in} and w_{out} can be represented by the following two equations:

$$f = -\frac{1}{2} R\cos(\theta) \tag{5.21-1}$$

$$w_{out} = \frac{w_{in}}{\sqrt{(1 - f^{-1}d)^2 + f^{-2}z_0^2}} \tag{5.21-2}$$

where $z_0 = \frac{\pi w_{in}^2 n_{Si}}{\lambda_0}$, z_0 is the Rayleigh range of the incident Gaussian beam. These equations establish the transmission and reflection characteristics of the Gaussian beam and the curved mirror. For the case of $f = d$ and $f = z_0$, it makes the $w_{out} = w_{in}$. This configuration makes the twice reflection of Gaussian beam remaining the same as the input ones to establish inversion symmetries in both time domain and space domain. By assisting the two mirrors together and setting the distance between two mirrors as R, the transmission coefficient can be represented by $\eta = \left[1 + \frac{d - R/2}{z_0}\right]^{-1}$.

5.3.4 Discussion of Goos-Hänchen shift

It's should note that the working principle of mirrors is based on the total internal reflection (TIR). The corresponding problem with the TIR is the effect of Goos-Hanchen shift. General theory believes that the positions of reflection point and incident point are the same; however, the Goos-Hanchen shift refers the position shift of reflection position and incident position are different. The distance of realistic position and ideal position can be expressed by the following equation:

$$D = \frac{cn_2\lambda}{\sqrt{n_1^2 \sin^2(\theta) - n^2}} \tag{5.22}$$

where n_1 and n_2 are the refractive indexes of low index and high index media, referring to the incident plane and the reflection plane. c is the light speed and λ is the wavelength. Considering two incident plane waves with only small difference of incident angles, thus the complex coefficient of incident waves can be expressed by:

$$A(z) = e^{i(\beta+\Delta\beta)z} + e^{i(\beta-\Delta\beta)z} = 2\cos(\Delta\beta z)e^{i\beta z} \tag{5.23}$$

It's should note that the phase delay φ is the function of θ or β. For a small $\Delta\beta$, the corresponding $\Delta\varphi$ is also small. Then it can be written into the following equation:

$$\varphi(\beta \pm \Delta\beta) = \varphi(\beta) \pm \frac{d\varphi}{d\beta}\Delta\beta \tag{5.24}$$

Thus the complex coefficient of reflection waves can be written into:

$$B(z) = (e^{i(\Delta\beta z - 2\Delta\varphi)} + e^{-i(\Delta\beta z - 2\Delta\varphi)})e^{i(\beta z - 2\varphi)} = 2\cos[\Delta\beta z(z - 2z_s)]e^{i(\beta z - 2\varphi)} \tag{5.25}$$

where $z_s \frac{d\varphi}{d\beta}$ is the vertical displacement of light inside the high index media. Combining the reflection's law with the following equation, the following two equations can be gotten:

for TE mode, $$k_0 z_s = \sqrt{N^2 - n_2^2}\tan(\theta) \tag{5.26-1}$$

for TM mode, $$k_0 z_s = \frac{\sqrt{N^2 - n_2^2}\tan(\theta)}{\frac{N^2}{n_1^2} + \frac{N^2}{n_2^2} - 1} \tag{5.26-2}$$

The relationship of vertical displacement and longitude displacement can be

expressed by a tangent function, which is not shown here.

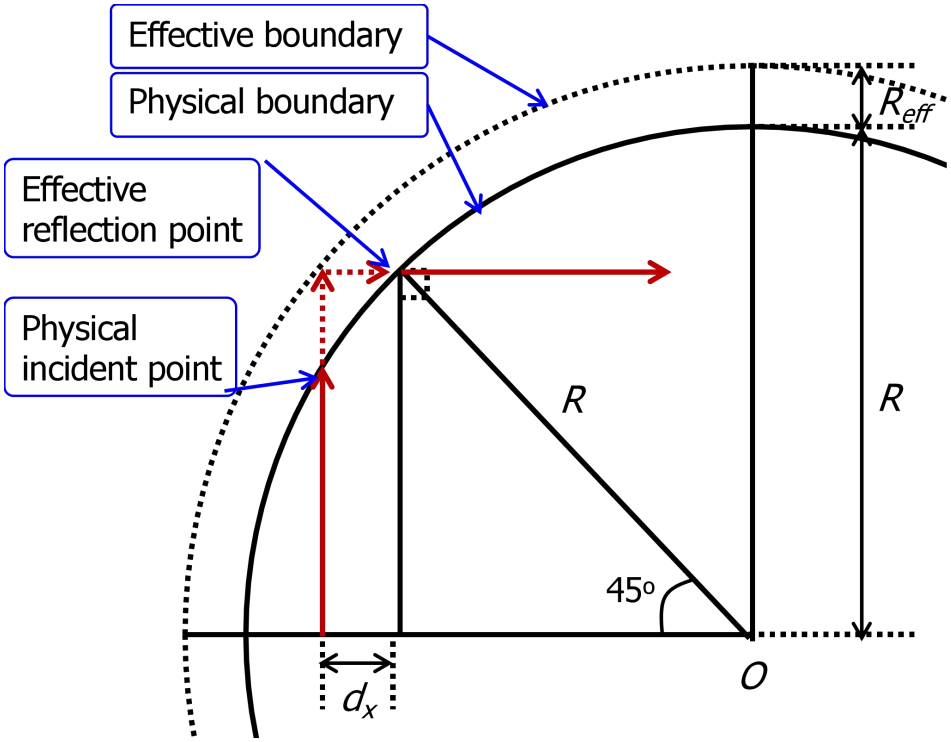

Fig. 5.23 Model of the effect of Goos-Hanchen shift by the physical boundary and effective boundary.

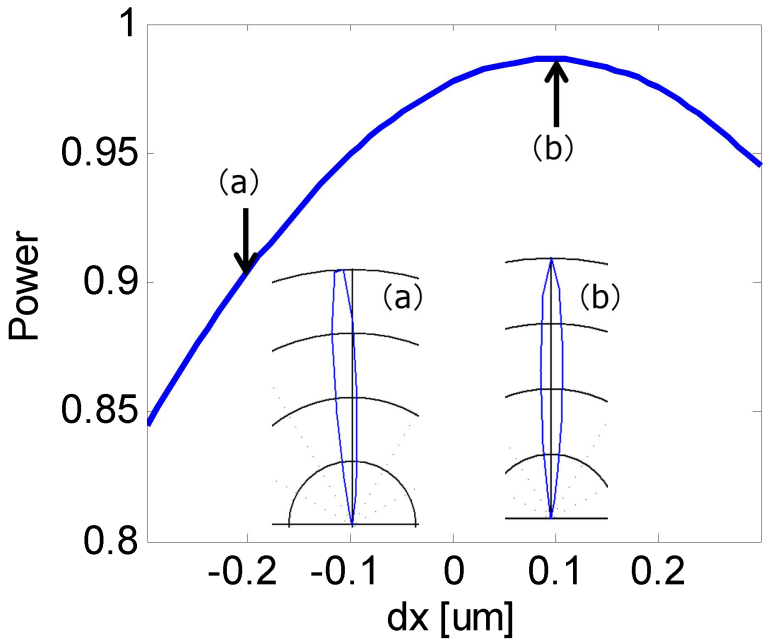

Fig. 5.24 Calculation results of the reflected power as a function of d_x, where the insert figures (a) and (b) show the radiation pattern of point (a) and (b) calculated by

the field on the simulation boundary.

The calculation model and results of E_y field based on 2D FDTD is shown Fig. 5.23 and 5.24, respectively. In Fig. 5.23, the black real line represents the profile of the curved silica mirror, which is also referred as the boundary of the silicon space and the silica mirror. It's clear seen that the waves exist inside the mirror, which is also known as the surface (evanescent) wave. The phenomenon confirms the evidence of Goos-Hanchen shift. The effective model of the Goos-Hanchen shift is represented in the following figure. The incident angle of Gaussian beam is also set to 45 degree for simplify. The black real line represents the physical boundary of the curved mirror, while the black dash line represents the effective boundary of the curved mirror, which is due to the effect of the Goos-Hanchen effect. R_{eff} represents the extra radius of the curved compared with the physical mirror. The increasing of curvature of the mirror make the reflection displacement from the previous position making the performance of the device decreasing, for example the reflection angle is not perpendicular to the incident angle for 45 degree incidence, and the the focus length is also varied with the variation of radius.

The calculated results of power of reflected Gaussian beam as a function of d_x is shown in the Fig. 5.24. The position of d_x = 0 represents the incident angle of 45 degree. It's clear seen that if the position of incident waves left shift 0.1um, the maximum power appears. The insert figures show the polar plot of the radiated far field of E_y components for points a and b. The insert figure (b) gives the direct evidence of reflected waves, which are perpendicular to the incident waves. These results show the effect of Goos-Hanchen shift. According to the calculation of the above equations, the calculated $R_{eff} \approx 0.1$ um is almost the same order of the optimized d_x.

5.3.5 Spectrum analysis

The optimized parameters for the calculation of the spectrum analysis is simply expressed as follows. For f and d equal $m/(\lambda_0/n_{Si})$ and assuming m = 70, λ_0 = 1.55 um, n_{Si} = 3.5, the f and d are set to 31 um and $r = 2f/Cos(45^o) = 62\sqrt{2}um$.

The calculated results of the transmittance as a function of wavelength for the once and twice reflection is shown in the following figure, i.e. reflection after one mirror and two mirrors. From the figure, the curved mirror shows a ultra low loss along a broad wavelength. Even after twice reflection, the wavelength range for transmittance larger than -0.04dB can be longer than 1.5 um. This is the first report of the waveguide crossing for a ultra low insertion loss and a broadband wavelength.

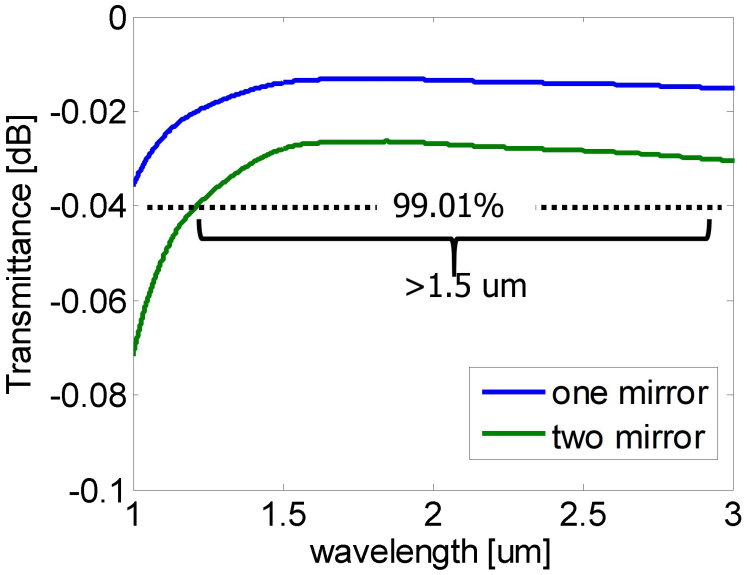

Fig. 5.25 Calculation results of the transmittance of reflection by one and two mirrors as a function of wavelength.

The field distribution of E_y component for the whole device is also shown in the Fig. 5.26. It's clear seen that the wave remain itself after twice reflection. The calculation results shows that the insertion loss and crosstalk can be less than -0.035 dB and -41 dB, respectively. It's also seen some diffracted waves due to the low calculation resolution, which is currently set to 30 nm. These diffracted waves occupy

the main loss and crosstalk in the whole system, which also show meanings in fabrication process. The roughness in industrial fabrication can be lower than 10 nm, which implies the performance of this device could be better than calculation.

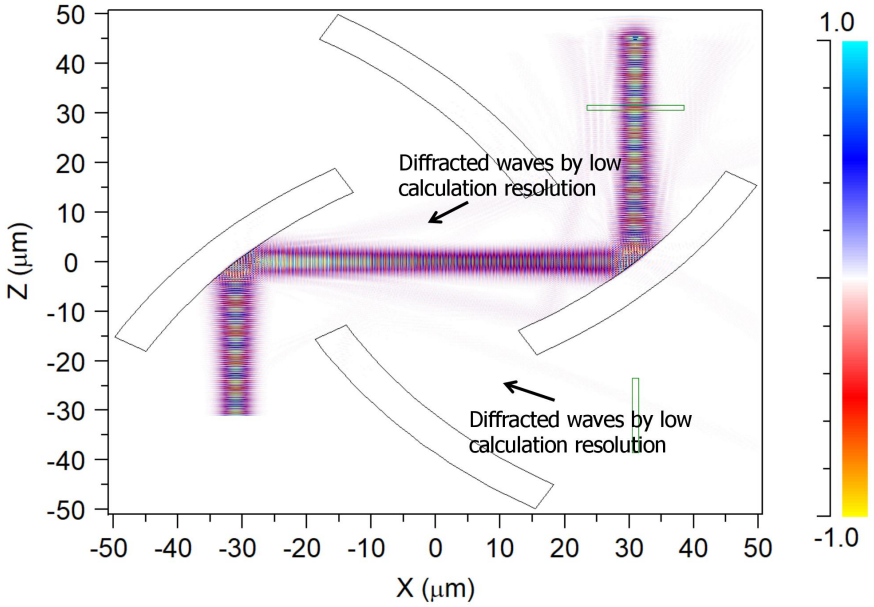

Fig. 5.26 Display of the overall distribution of E_y field after reflected twice, where the diffracted waves come from the low calculation resolution.

5.3.6 Discussion of ABCD's law

The ABCD's law is reviewed and discussed in the sub-chapter as a complement of theory. The Gaussian beam, which is incident in the tangent-plane of the curved silica mirror, can be described by the following ABCD matrix given by [149]:

$$M = \begin{bmatrix} A & B \\ C & D \end{bmatrix} = \begin{bmatrix} 1 & 0 \\ -f & 1 \end{bmatrix} \tag{5-27}$$

where $f = -0.5RCos\theta_{in}$.

The output Gaussian beam transformed and reflected by the curved mirror can be represented by the following two equations given by the characteristics of W_{out} and d_{out}, which represent the beam waist of the output Gaussian beams and the distance

between location of the output Gaussian beam waist and the point of incidence, respectively.

$$w_{out} = \frac{w_{in}}{\sqrt{(Cd_{in} + D)^2 + C^2 z_0^2}} \tag{5.28-1}$$

$$d_{out} = \frac{(Ad_{in} + B)(Cd_{in} + D) + ACz_0^2}{(Cd_{in} + D)^2 + C^2 z_0^2} \tag{5.28-2b}$$

where w_{in} is the beam waist of the incident Gaussian beam, din is the distance of location of incident Gaussian beam and incident point, and z_0 is the Rayleigh of the incident Gaussian beam. Using the above equations and the ABCD matrix represented above, the normalized characteristics of output Gaussian beam can be given by the following two equations:

$$\frac{z_r}{z_0} = \frac{1}{(1 - \frac{d_{in}}{f}) + \frac{z_0^2}{f^2}} \tag{5.29-1a}$$

$$\frac{d_{out}}{f} = \frac{z_r}{z_0}\left[\frac{z_0^2}{f^2} - \frac{d_{in}}{f}\left(1 - \frac{d_{in}}{f}\right)\right] \tag{5.29-2b}$$

where z_r is the Rayleigh range of the output Gaussian beam. The above equations describe the transformation of Gaussian beam after reflection from a curved silica mirror.

5.4 Summary

In Summary, this chapter discusses and shows the results of the research of slab space optics. First, a kind of planar chiral meta-materials is discussed and studied by 3D-FDTD methods. The circular dichroism is analyzed by the Jones matrix. The optical activity is verified by the principles of guided mode resonance (GMR) and Fabry-Perot (FP) resonance. The filtering characteristics is achieved by sandwiching two wave plates with orthogonal polarization states. The shift of resonant is achieved by varying the pitch size. Second, the results of slab space optics are discussed and analyzed in the following two parts: design and investigate a dual-layer grating

coupler for efficient fiber-chip coupling; design and investigate a functional curved silica mirror for broad band waveguide crossing. The grating coupler is designed with dual-gratings for overcoming the wavelength and polarization diversity. The phase matching condition is discussed for efficient coupling from fibers to waveguides for different polarization states and optical bands. The effect of dual-layer Fabry-Perot resonance is also investigated for high efficient coupling. A kind of waveguide crossing is designed with curved silica mirrors as reflectors. The principle of ABCD's law is presented for understanding the transformation of Gaussian beam after reflection by the curved silica mirror. The radiation modes of terminated slab waveguides and effect of Goos-Hanchen shift are discussed for a deep understanding of the principle of the device. Calculation results show that the device supports a broadband operation wavelength and low insertion loss and low crosstalk.

Chapter 6 Conclusions

6.1 Summary of contributions

This thesis related with ‘study of nano-photonics integrated devices’ is presented above and summarized in this chapter. The demands of photonics integrated devices are first introduced in the chapter 1 to response the doubt that why photonics is necessary and needed. To satisfy the huge amount of information in the right-now world and future world, photons are used as the information carrier instead of electrons is the trend for their huge bandwidth, low transmission loss, low power consumption and high degree of integration. Waveguide, as the basic transmission line, is the most important component in the photonics integrated devices. Silicon photonics based waveguides and plasmonic waveguides are then introduced for the purpose of high degree of integration. The basic theories for understand the transmission and mode characteristics of optical waves in waveguides are then introduced in chapter 2. The Finite-Difference Time-Domain (FDTD) method and Beam Propagation method (BPM) are first introduced for understanding the transmission characteristics of waveguides. The finite element method (FEM) is the introduced for calculating the mode characteristics of waveguides. In chapter 3, a kind of end-end waveguide coupler is introduced for solving the mismatching of silicon waveguides and plasmonic waveguides. By applying the funnel effect, high transmission efficiency and broad operation band can be achieved. The effective mode area and local reflectivity are calculated for understanding the high transmission efficiency and low return loss. In chapter 4, a kind of side-coupled plasmonic filter is introduced for wavelength demultiplexer. The S-matrix is established for understanding the transmission characteristics and spectrum response. The filter is composed of a directional coupler and a side-coupled Fabry-Perot cavity. The directional coupler also works as the reflectivity mirrors of the cavity. Results show that for proper design, the multiple mode wavelength filtering can be vanished and

remain single mode output. This result shows the possibility of design of the ultra wide free spectrum range filter. In chapter 5, the research on slab space optics is showed. A kind of planar chiral meta-material is designed for the filters in the multiple spectrum imaging system. The filtering characteristics is verified by the guided mode resonance and Fabry-Perot resonance. Then a kind of dual-layer grating coupler is designed for efficient fiber-chip coupling. The phase matching conditions are calculated for the diffraction waves and guided waves. For proper design, a kind of dual-wavelength and dual polarization state coupler is achieved. The dual-layer Fabry-Perot resonance is also investigated for efficient coupling. Finally, a kind of novel waveguide crossing is designed using curved silica mirrors as reflectors. The ABCD's law is used as the basic principle for understanding the transformation of input Gaussian beam and output Gaussian beam. The effect of Goos-Hanchen effect is also discussed for improving the performance of the device. Results show that this design owns characteristics of low insertion loss, low crosstalk, and broad bandwidth. The concept of slab space optics enhances the new thoughts in the design of photonics integrated chips and broaden the horizon of design.

6.2 Future research

In the thesis, series of passive devices are designed and analyzed in photonics integrated chips in numerical simulations and calculations. These designs may show new results and bring new physical concepts for other researchers. However, there are still some problems and insignificance remained. First, the experimental results are expected in the future work. Although the scientists have finished the basic theories, such as the waveguide theories and calculation methods, the experimental results are also important in design and investigation of photonics integrated devices. The impurity of materials and fabrication tolerance may effect the final results and sometimes inconsistent with the calculation results. Unfortunately, the experimental apparatuses are not sufficient in the lab. Thus, making up the experimental data wish to be finished in the future work. Second, the whole thesis is based on several

sub-devices attempting to simulate the working flow of the whole system. It's correct in science, however insufficient in engineering. The industry prefer a complete system than separated devices. Besides, verifying the correctness of a whole system is more exciting than separated components, though a big team is needed. Anyway, this thesis discusses and presents some novel concepts in the design of photonics integrated chips and hopes to bring the way forward for both science and engineering.

Bibliography

[1] Nagatsuma T, Ducournau G, Renaud C C. Advances in terahertz communications accelerated by photonics[J]. Nature Photonics, 2016, 10(6): 371.

[2] Kleine-Ostmann T, Nagatsuma T. A review on terahertz communications research[J]. Journal of Infrared, Millimeter, and Terahertz Waves, 2011, 32(2): 143-171.

[3] Argyris A, Hamacher M, Chlouverakis K E, et al. Photonic integrated device for chaos applications in communications[J]. Physical review letters, 2008, 100(19): 194101.

[4] Ibrahim T A, Amarnath K, Kuo L C, et al. Photonic logic NOR gate based on two symmetric microring resonators[J]. Optics letters, 2004, 29(23): 2779-2781.

[5] Medhekar S, Sarkar R K. All-optical passive transistor[J]. Optics letters, 2005, 30(8): 887-889.

[6] Vollmer F, Yang L. Review Label-free detection with high-Q microcavities: a review of biosensing mechanisms for integrated devices[J]. Nanophotonics, 2012, 1(3-4): 267-291.

[7] Silicon photonics for telecommunications and biomedicine[M]. CRC Press, 2011.

[8] Vollmer F, Yang L. Review Label-free detection with high-Q microcavities: a review of biosensing mechanisms for integrated devices[J]. Nanophotonics, 2012, 1(3-4): 267-291.

[9] Waggoner P S, Craighead H G. Micro-and nanomechanical sensors for environmental, chemical, and biological detection[J]. Lab on a Chip, 2007, 7(10): 1238-1255.

[10] Lambeck P V. Integrated optical sensors for the chemical domain[J]. Measurement science and technology, 2006, 17(8): R93.

[11] Passaro V, Tullio C, Troia B, et al. Recent advances in integrated photonic sensors[J]. Sensors, 2012, 12(11): 15558-15598.

[12] Chen Y, Lin H, Hu J, et al. Heterogeneously integrated silicon photonics for the mid-infrared and spectroscopic sensing[J]. ACS nano, 2014, 8(7): 6955-6961.

[13] Politi A, Matthews J C F, Thompson M G, et al. Integrated quantum photonics[J]. IEEE Journal of Selected Topics in Quantum Electronics, 2009, 15(6): 1673-1684.

[14] Dietrich C P, Fiore A, Thompson M G, et al. GaAs integrated quantum photonics: Towards compact and multi-functional quantum photonic integrated circuits[J]. Laser & Photonics Reviews, 2016, 10(6): 870-894.

[15] Silverstone J W, Bonneau D, O'Brien J L, et al. Silicon quantum photonics[J]. IEEE Journal of Selected Topics in Quantum Electronics, 2016, 22(6): 390-402.

[16] "What is big data," URL:www-01.ibm.comsoftwaredatabigdatawhat-is-big-data.html.

[17] "Intel, Facebook collaborate on future data center rack technologies," URL: https://newsroom.intel.com/news-releases/intel-facebook-collaborate-on-future-data-center-rack-technologies/.

[18] Urino Y, Usuki T, Fujikata J, et al. High-density and wide-bandwidth optical interconnects with silicon optical interposers[J]. Photonics Research, 2014, 2(3): A1-A7.

[19] Silicon photonics III: Systems and applications[M]. Springer Science & Business Media, 2016.

[20] Knickerbocker J U, Andry P S, Dang B, et al. 3D silicon integration[C] 58th Electronic Components and Technology Conference. IEEE, 2008: 538-543.

[21] M. Girtan, "Is photonics the new electronics", Materials Today, vol. 17, no. 3, pp. 100-101, 2016.

[22] Claes T, Bogaerts W, Bienstman P. Vernier-cascade label-free biosensor with integrated arrayed waveguide grating for wavelength interrogation with low-cost broadband source[J]. Optics letters, 2011, 36(17): 3320-3322.

[23] Martens D, Subramanian A Z, Pathak S, et al. Compact silicon nitride arrayed waveguide gratings for very near-infrared wavelengths[J]. IEEE Photonics Technology Letters, 2015, 27(2): 137-140.

[24] Smit M K, Van Dam C. PHASAR-based WDM-devices: Principles, design and

applications[J]. IEEE Journal of selected topics in quantum electronics, 1996, 2(2): 236-250.

[25] Liu A, Jones R, Liao L, et al. A high-speed silicon optical modulator based on a metal–oxide–semiconductor capacitor[J]. Nature, 2004, 427(6975): 615.

[26] Gardes F Y, Thomson D J, Emerson N G, et al. 40 Gb/s silicon photonics modulator for TE and TM polarisations[J]. Optics express, 2011, 19(12): 11804-11814.

[27] Ziebell M, Marris-Morini D, Rasigade G, et al. 40 Gbit/s low-loss silicon optical modulator based on a pipin diode[J]. Optics express, 2012, 20(10): 10591-10596.

[28] Fang A W, Jones R, Park H, et al. Integrated AlGaInAs-silicon evanescent racetrack laser and photodetector[J]. Optics express, 2007, 15(5): 2315-2322.

[29] Park H, Fang A W, Jones R, et al. A hybrid AlGaInAs-silicon evanescent waveguide photodetector[J]. Optics express, 2007, 15(10): 6044-6052.

[30] Vivien L, Osmond J, Fédéli J M, et al. 42 GHz pin Germanium photodetector integrated in a silicon-on-insulator waveguide[J]. Optics express, 2009, 17(8): 6252-6257.

[31] Chen L, Chen Y. Compact, low-loss and low-power 8× 8 broadband silicon optical switch[J]. Optics express, 2012, 20(17): 18977-18985.

[32] Tanabe T, Notomi M, Mitsugi S, et al. Fast bistable all-optical switch and memory on a silicon photonic crystal on-chip[J]. Optics letters, 2005, 30(19): 2575-2577.

[33] Beggs D M, White T P, O'Faolain L, et al. Ultracompact and low-power optical switch based on silicon photonic crystals[J]. Optics letters, 2008, 33(2): 147-149.

[34] Ma Y, Zhang Y, Yang S, et al. Ultralow loss single layer submicron silicon waveguide crossing for SOI optical interconnect[J]. Optics express, 2013, 21(24): 29374-29382.

[35] Jones A M, DeRose C T, Lentine A L, et al. Ultra-low crosstalk, CMOS compatible waveguide crossings for densely integrated photonic interconnection networks[J]. Optics express, 2013, 21(10): 12002-12013.

[36] Huang Y, Song J, Luo X, et al. CMOS compatible monolithic multi-layer Si 3 N

4-on-SOI platform for low-loss high performance silicon photonics dense integration[J]. Optics Express, 2014, 22(18): 21859-21865.

[37] Gao S, Lin H, Zhou L, et al. Power Efficient Thermal Optical Tunable Grating Coupler Based on Silicon Photonic Platform[J]. IEEE Photonics Technology Letters, 2019.

[38] Gostimirovic D, Winnie N Y. An Open-Source Artificial Neural Network Model for Polarization-Insensitive Silicon-on-Insulator Subwavelength Grating Couplers[J]. IEEE Journal of Selected Topics in Quantum Electronics, 2019, 25(3): 1-5.

[39] Kwon M S. Silicon photonic add-drop filter based on a grating-assisted co-directionally coupled vertical hybrid structure[J]. Optics Express, 2019, 27(8): 11748-11765.

[40] Yang B K, Shin S Y, Zhang D. Ultrashort polarization splitter using two-mode interference in silicon photonic wires[J]. IEEE Photonics Technology Letters, 2009, 21(7): 432-434.

[41] Dai D, Bowers J E. Novel concept for ultracompact polarization splitter-rotator based on silicon nanowires[J]. Optics express, 2011, 19(11): 10940-10949.

[42] Sacher W D, Barwicz T, Taylor B J F, et al. Polarization rotator-splitters in standard active silicon photonics platforms[J]. Optics express, 2014, 22(4): 3777-3786.

[43] Barnes W L, Dereux A, Ebbesen T W. Surface plasmon subwavelength optics[J]. nature, 2003, 424(6950): 824.

[44] Sorger V J, Oulton R F, Ma R M, et al. Toward integrated plasmonic circuits[J]. MRS bulletin, 2012, 37(8): 728-738.

[45] Yang R, Lu Z. Subwavelength plasmonic waveguides and plasmonic materials[J]. International Journal of Optics, 2012, 2012.

[46] Fang Y, Sun M. Nanoplasmonic waveguides: towards applications in integrated nanophotonic circuits[J]. Light: Science & Applications, 2015, 4(6): e294.

[47] Lin X S, Huang X G. Tooth-shaped plasmonic waveguide filters with nanometeric sizes[J]. Optics letters, 2008, 33(23): 2874-2876.

[48] Tao J, Huang X G, Lin X, et al. A narrow-band subwavelength plasmonic

waveguide filter with asymmetrical multiple-teeth-shaped structure[J]. Optics express, 2009, 17(16): 13989-13994.

[49] Lu H, Liu X, Mao D, et al. Tunable band-pass plasmonic waveguide filters with nanodisk resonators[J]. Optics Express, 2010, 18(17): 17922-17927.

[50] Wu T, Liu Y, Yu Z, et al. The sensing characteristics of plasmonic waveguide with a ring resonator[J]. Optics express, 2014, 22(7): 7669-7677.

[51] Zhou L, Sun X, Li X, et al. Miniature microring resonator sensor based on a hybrid plasmonic waveguide[J]. Sensors, 2011, 11(7): 6856-6867.

[52] Lu H, Liu X, Mao D, et al. Plasmonic nanosensor based on Fano resonance in waveguide-coupled resonators[J]. Optics letters, 2012, 37(18): 3780-3782.

[53] Ansell D, Radko I P, Han Z, et al. Hybrid graphene plasmonic waveguide modulators[J]. Nature communications, 2015, 6: 8846.

[54] Nikolajsen T, Leosson K, Bozhevolnyi S I. Surface plasmon polariton based modulators and switches operating at telecom wavelengths[J]. Applied Physics Letters, 2004, 85(24): 5833-5835.

[55] Piao X, Yu S, Park N. Control of Fano asymmetry in plasmon induced transparency and its application to plasmonic waveguide modulator[J]. Optics express, 2012, 20(17): 18994-18999.

[56] Tsuji Y, Koshiba M, Shiraishi T. Finite element beam propagation method for three-dimensional optical waveguide structures[J]. Journal of lightwave technology, 1997, 15(9): 1728-1734.

[57] Koshiba M, Tsuji Y. Curvilinear hybrid edge/nodal elements with triangular shape for guided-wave problems[J]. Journal of Lightwave Technology, 2000, 18(5): 737-743.

[58] Peterson A F. Vector finite element formulation for scattering from two-dimensional heterogeneous bodies[J]. IEEE transactions on antennas and propagation, 1994, 42(3): 357-365.

[59] Nédélec J C. Mixed finite elements in $\mathbb{R}$ 3[J]. Numerische Mathematik, 1980, 35(3): 315-341.

[60] Feit M D, Fleck J A. Light propagation in graded-index optical fibers[J]. Applied

optics, 1978, 17(24): 3990-3998.

[61] Yevick D, Hermansson B. Efficient beam propagation techniques[J]. IEEE Journal of quantum electronics, 1990, 26(1): 109-112.

[62] Chung Y, Dagli N. An assessment of finite difference beam propagation method[J]. IEEE Journal of quantum electronics, 1990, 26(8): 1335-1339.

[63] Zienkiewicz O C, Taylor R L, Nithiarasu P, et al. The finite element method[M]. London: McGraw-hill, 1977.

[64] Yee K. Numerical solution of initial boundary value problems involving Maxwell's equations in isotropic media[J]. IEEE Transactions on antennas and propagation, 1966, 14(3): 302-307.

[65] Yee K S, Chen J S. The finite-difference time-domain (FDTD) and the finite-volume time-domain (FVTD) methods in solving Maxwell's equations[J]. IEEE Transactions on Antennas and Propagation, 1997, 45(3): 354-363.

[66] Genov D A, Ambati M, Zhang X. Surface plasmon amplification in planar metal films[J]. IEEE Journal of Quantum Electronics, 2007, 43(11): 1104-1108.

[67] Veronis G, Fan S. Modes of subwavelength plasmonic slot waveguides[J]. Journal of Lightwave Technology, 2007, 25(9): 2511-2521.

[68] Baida F I, Belkhir A, Van Labeke D, et al. Subwavelength metallic coaxial waveguides in the optical range: Role of the plasmonic modes[J]. Physical Review B, 2006, 74(20): 205419.

[69] Zia R, Selker M D, Catrysse P B, et al. Geometries and materials for subwavelength surface plasmon modes[J]. JOSA A, 2004, 21(12): 2442-2446.

[70] Liu S, Zhou L, Wang H, et al. Hybrid plasmonic waveguide made of a nanofiber attached to a metal film[J]. Optics express, 2015, 23(13): 16984-16992.

[71] Feng N N, Brongersma M L, Dal Negro L. Metal–Dielectric Slot-Waveguide Structures for the Propagation of Surface Plasmon Polaritons at 1.55$\mu {\hbox {m}} $[J]. IEEE Journal of Quantum Electronics, 2007, 43(6): 479-485.

[72] Chen D. Cylindrical hybrid plasmonic waveguide for subwavelength confinement of light[J]. Applied optics, 2010, 49(36): 6868-6871.

[73] Bian Y, Gong Q. Optical performance of one-dimensional hybrid

metal–insulator–metal structures at telecom wavelength[J]. Optics Communications, 2013, 308: 30-35.

[74] Ginzburg P, Orenstein M. Plasmonic transmission lines: from micro to nano scale with λ/4 impedance matching[J]. Optics express, 2007, 15(11): 6762-6767.

[75] Pile D F P, Gramotnev D K. Adiabatic and nonadiabatic nanofocusing of plasmons by tapered gap plasmon waveguides[J]. Applied Physics Letters, 2006, 89(4): 041111.

[76] Feng N N, Dal Negro L. Plasmon mode transformation in modulated-index metal-dielectric slot waveguides[J]. Optics letters, 2007, 32(21): 3086-3088.

[77] Weeber J C, Dereux A, Girard C, et al. Plasmon polaritons of metallic nanowires for controlling submicron propagation of light[J]. Physical Review B, 1999, 60(12): 9061.

[78] Sanchis P, Blasco J, Martínez A, et al. Design of silicon-based slot waveguide configurations for optimum nonlinear performance[J]. Journal of Lightwave Technology, 2007, 25(5): 1298-1305.

[79] Rukhlenko I D, Premaratne M, Agrawal G P. Effective mode area and its optimization in silicon-nanocrystal waveguides[J]. Optics letters, 2012, 37(12): 2295-2297.

[80] Li X, Feng X, Xiao X, et al. Silicon slot waveguides with low transmission and bending losses at 1064 nm[J]. IEEE Photonics Technology Letters, 2016, 28(1): 19-22.

[81] Almeida V R, Xu Q, Barrios C A, et al. Guiding and confining light in void nanostructure[J]. Optics letters, 2004, 29(11): 1209-1211.

[82] Wang X, Grist S, Flueckiger J, et al. Silicon photonic slot waveguide Bragg gratings and resonators[J]. Optics express, 2013, 21(16): 19029-19039.

[83] Tan D T H, Ikeda K, Fainman Y. Cladding-modulated Bragg gratings in silicon waveguides[J]. Optics letters, 2009, 34(9): 1357-1359.

[84] Zhu S, Lo G Q, Kwong D L. Components for silicon plasmonic nanocircuits based on horizontal Cu-SiO 2-Si-SiO 2-Cu nanoplasmonic waveguides[J]. Optics express, 2012, 20(6): 5867-5881.

[85] Ono M, Taniyama H, Xu H, et al. Deep-subwavelength plasmonic mode converter with large size reduction for Si-wire waveguide[J]. Optica, 2016, 3(9): 999-1005.

[86] Nielsen M P, Elezzabi A Y. Nanoplasmonic distributed Bragg reflector resonators for monolithic integration on a complementary metal-oxide-semiconductor platform[J]. Applied Physics Letters, 2013, 103(5): 051107.

[87] Briggs R M, Grandidier J, Burgos S P, et al. Efficient coupling between dielectric-loaded plasmonic and silicon photonic waveguides[J]. Nano letters, 2010, 10(12): 4851-4857.

[88] Veronis G, Fan S. Theoretical investigation of compact couplers between dielectric slab waveguides and two-dimensional metal-dielectric-metal plasmonic waveguides[J]. Optics Express, 2007, 15(3): 1211-1221.

[89] Wahsheh R A, Lu Z, Abushagur M A G. Nanoplasmonic couplers and splitters[J]. Optics Express, 2009, 17(21): 19033-19040.

[90] Muellner P, Wellenzohn M, Hainberger R. Nonlinearity of optimized silicon photonic slot waveguides[J]. Optics express, 2009, 17(11): 9282-9287.

[91] Zayats A V, Smolyaninov I I, Maradudin A A. Nano-optics of surface plasmon polaritons[J]. Physics reports, 2005, 408(3-4): 131-314.

[92] Veronis G, Fan S. Bends and splitters in metal-dielectric-metal subwavelength plasmonic waveguides[J]. Applied physics letters, 2005, 87(13): 131102.

[93] Noual A, Akjouj A, Pennec Y, et al. Modeling of two-dimensional nanoscale Y-bent plasmonic waveguides with cavities for demultiplexing of the telecommunication wavelengths[J]. New Journal of Physics, 2009, 11(10): 103020.

[94] Chen J, Li Z, Zhang R, et al. Response line-shapes in compact coupled plasmonic resonator systems[J]. Plasmonics, 2013, 8(2): 1129-1134.

[95] Wu C, Ding H, Huang T, et al. Plasmon-induced transparency and refractive index sensing in side-coupled stub-hexagon resonators[J]. Plasmonics, 2018, 13(1): 251-257.

[96] Yang J, Song X, Chen Z, et al. Tunable multi-fano resonances in MDM-based side-coupled resonator system and its application in nanosensor[J]. Plasmonics, 2017,

12(6): 1665-1672.

[97] Zhang T, Chen L, Wang B, et al. Tunable broadband plasmonic field enhancement on a graphene surface using a normal-incidence plane wave at mid-infrared frequencies[J]. Scientific reports, 2015, 5: 11195.

[98] Kong Y, Wei Q, Liu C, et al. Nanoscale temperature sensor based on Fano resonance in metal–insulator–metal waveguide[J]. Optics Communications, 2017, 384: 85-88.

[99] Lu H, Gan X, Mao D, et al. Graphene-supported manipulation of surface plasmon polaritons in metallic nanowaveguides[J]. Photonics Research, 2017, 5(3): 162-167.

[100] Zand I, Abrishamian M S, Berini P. Highly tunable nanoscale metal-insulator-metal split ring core ring resonators (SRCRRs)[J]. Optics express, 2013, 21(1): 79-86.

[101] Lin X, Huang X. Numerical modeling of a teeth-shaped nanoplasmonic waveguide filter[J]. JOSA B, 2009, 26(7): 1263-1268.

[102] Mei X, Huang X, Tao J, et al. A wavelength demultiplexing structure based on plasmonic MDM side-coupled cavities[J]. JOSA B, 2010, 27(12): 2707-2713.

[103] Lu H, Liu X, Gong Y, et al. Enhancement of transmission efficiency of nanoplasmonic wavelength demultiplexer based on channel drop filters and reflection nanocavities[J]. Optics express, 2011, 19(14): 12885-12890.

[104] Pannipitiya A, Rukhlenko I D, Premaratne M, et al. Improved transmission model for metal-dielectric-metal plasmonic waveguides with stub structure[J]. Optics express, 2010, 18(6): 6191-6204.

[105] Zhang Q, Huang X G, Lin X S, et al. A subwavelength coupler-type MIM optical filter[J]. Optics express, 2009, 17(9): 7549-7554.

[106] Deng Y, Cao G, Wu Y, et al. Theoretical description of dynamic transmission characteristics in MDM waveguide aperture-side-coupled with ring cavity[J]. Plasmonics, 2015, 10(6): 1537-1543.

[107] Cao G, Li H, Deng Y, et al. Systematic theoretical analysis of selective-mode plasmonic filter based on aperture-side-coupled slot cavity[J]. Plasmonics, 2014, 9(5):

1163-1169.

[108] Wang S, Xu Y, Lan S, et al. Flat-top reflection characteristics in metal-dielectric-metal plasmonic waveguide structure side coupled with cascaded double cavities[J]. Plasmonics, 2011, 6(4): 689.

[109] Amnon Y, Yeh P. Optical waves in crystals: propagation and control of laser radiation[J]. New York City, NY: Wiley, 1984.

[110] Han Z, Forsberg E, He S. Surface plasmon Bragg gratings formed in metal-insulator-metal waveguides[J]. IEEE Photonics Technology Letters, 2007, 19(2): 91-93.

[111] Johnson P B, Christy R W. Optical constants of the noble metals[J]. Physical review B, 1972, 6(12): 4370.

[112] Lu H, Gan X, Mao D, et al. Flexibly tunable high-quality-factor induced transparency in plasmonic systems[J]. Scientific reports, 2018, 8(1): 1558.

[113] Konishi K, Bai B, Meng X, et al. Observation of extraordinary optical activity in planar chiral photonic crystals[J]. Optics express, 2008, 16(10): 7189-7196.

[114] Ohtera Y. Numerical analysis of artificial optical activities of planar chiral nano-gratings[J]. IEICE Transactions on Electronics, 2014, 97(1): 33-39.

[115] Taflove A, Hagness S C. Computational electrodynamics: the finite-difference time-domain method[M]. Artech house, 2005.

[116] Mur G. Absorbing boundary conditions for the finite-difference approximation of the time-domain electromagnetic-field equations[J]. IEEE transactions on Electromagnetic Compatibility, 1981 (4): 377-382.

[117] Bai B, Svirko Y, Turunen J, et al. Optical activity in planar chiral metamaterials: Theoretical study[J]. Physical Review A, 2007, 76(2): 023811.

[118] Rosenblatt D, Sharon A, Friesem A A. Resonant grating waveguide structures[J]. IEEE Journal of Quantum electronics, 1997, 33(11): 2038-2059.

[119] Themelis G, Yoo J S, Ntziachristos V. Multispectral imaging using multiple-bandpass filters[J]. Optics letters, 2008, 33(9): 1023-1025.

[120] Subbaraman H, Xu X, Hosseini A, et al. Recent advances in silicon-based passive and active optical interconnects[J]. Optics express, 2015, 23(3): 2487-2511.

[121] Soref R. The past, present, and future of silicon photonics[J]. IEEE Journal of selected topics in quantum electronics, 2006, 12(6): 1678-1687.

[122] Chu T, Yamada H, Ishida S, et al. Compact 1× N thermo-optic switches based on silicon photonic wire waveguides[J]. Optics Express, 2005, 13(25): 10109-10114.

[123] Volz T, Reinhard A, Winger M, et al. Ultrafast all-optical switching by single photons[J]. Nature Photonics, 2012, 6(9): 605.

[124] Reed G T, Mashanovich G, Gardes F Y, et al. Silicon optical modulators[J]. Nature photonics, 2010, 4(8): 518.

[125] Kita T, Yamamoto N, Kawanishi T, et al. Ultra-compact wavelength-tunable quantum-dot laser with silicon-photonics double ring filter[J]. Applied Physics Express, 2015, 8(6): 062701.

[126] Kita T, Yamamoto N, Matsumoto A, et al. Heterogeneous quantum dot/silicon photonics-based wavelength-tunable laser diode with a 44 nm wavelength-tuning range[J]. Japanese Journal of Applied Physics, 2016, 55(4S): 04EH11.

[127] Dai D, Bowers J E. Novel concept for ultracompact polarization splitter-rotator based on silicon nanowires[J]. Optics express, 2011, 19(11): 10940-10949.

[128] Matsuda N, Nishi H, Karkus P, et al. Generation of entangled photons using an arrayed waveguide grating[J]. Journal of Optics, 2017, 19(12): 124005.

[129] Takesue H, Matsuda N, Kuramochi E, et al. An on-chip coupled resonator optical waveguide single-photon buffer[J]. Nature communications, 2013, 4: 2725.

[130] Park H, Kim S, Park J, et al. A fiber-to-chip coupler based on Si/SiON cascaded tapers for Si photonic chips[J]. Optics express, 2013, 21(24): 29313-29319.

[131] Bakir B B, De Gyves A V, Orobtchouk R, et al. Low-Loss (< 1 dB) and polarization-insensitive edge fiber couplers fabricated on 200-mm silicon-on-insulator wafers[J]. IEEE Photonics Technology Letters, 2010, 22(11): 739-741.

[132] Yamada H, Nozawa M, Kinoshita M, et al. Vertical-coupling optical interface for on-chip optical interconnection[J]. Optics express, 2011, 19(2): 698-703.

[133] Taillaert D, Bogaerts W, Bienstman P, et al. An out-of-plane grating coupler for efficient butt-coupling between compact planar waveguides and single-mode fibers[J]. IEEE Journal of Quantum Electronics, 2002, 38(7): 949-955.

[134] Taillaert D, Van Laere F, Ayre M, et al. Grating couplers for coupling between optical fibers and nanophotonic waveguides[J]. Japanese Journal of Applied Physics, 2006, 45(8R): 6071.

[135] Ushida J, Tokushima M, Sobu Y, et al. Optical loss analysis and parameter optimization for fan-shaped single-polarization grating coupler at wavelength of 1.3 μm band[J]. Japanese Journal of Applied Physics, 2018, 57(5): 052502.

[136] Song J H, Rottenberg X. Low-back-reflection grating couplers using asymmetric grating trenches[J]. IEEE Photonics Technology Letters, 2017, 29(4): 389-392.

[137] Chen X, Tsang H K. Polarization-independent grating couplers for silicon-on-insulator nanophotonic waveguides[J]. Optics letters, 2011, 36(6): 796-798.

[138] Chen X, Li C, Tsang H K. Two dimensional silicon waveguide chirped grating couplers for vertical optical fibers[J]. Optics Communications, 2010, 283(10): 2146-2149.

[139] Taillaert D, Chong H, Borel P I, et al. A compact two-dimensional grating coupler used as a polarization splitter[J]. IEEE Photonics Technology Letters, 2003, 15(9): 1249-1251.

[140] Katayama T, Ito J, Kawaguchi H. Polarization-dependent coupling between a polarization-independent high-index-contrast subwavelength grating and waveguides[J]. Applied Physics Express, 2016, 9(7): 072703.

[141] Tang Y, Dai D, He S. Proposal for a grating waveguide serving as both a polarization splitter and an efficient coupler for silicon-on-insulator nanophotonic circuits[J]. IEEE Photonics Technology Letters, 2009, 21(4): 242-244.

[142] Streshinsky M, Shi R, Novack A, et al. A compact bi-wavelength polarization splitting grating coupler fabricated in a 220 nm SOI platform[J]. Optics express, 2013, 21(25): 31019-31028.

[143] Nambiar S, Hemalatha M, Sharma T, et al. Integrated silicon nitride based TE dual-band grating coupler[C]//2017 Conference on Lasers and Electro-Optics Europe & European Quantum Electronics Conference (CLEO/Europe-EQEC). IEEE, 2017: 1-1.

[144] Wang S, Hong Y, Zhu Y, et al. Compact high-efficiency perfectly-vertical grating coupler on silicon at O-band[J]. Optics express, 2017, 25(18): 22032-22037.

[145] Mizutani A, Eto Y, Kikuta H. A grating coupler with a trapezoidal hole array for perfectly vertical light coupling between optical fibers and waveguides[J]. 2017.

[146] Michaels A, Yablonovitch E. Inverse design of near unity efficiency perfectly vertical grating couplers[J]. Optics express, 2018, 26(4): 4766-4779.

[147] Dai M, Ma L, Xu Y, et al. Highly efficient and perfectly vertical chip-to-fiber dual-layer grating coupler[J]. Optics express, 2015, 23(2): 1691-1698.

[148] Watanabe T, Ayata M, Koch U, et al. Perpendicular grating coupler based on a blazed antiback-reflection structure[J]. Journal of Lightwave Technology, 2017, 35(21): 4663-4669.

[149] Glisson A. Quasioptical Systems: Gaussian Beam Quasioptical Propaga-Derived Results To Reveal The Underlying Physics And Implications [Book Review][J]. IEEE Antennas and Propagation Magazine, 1999, 41(1): 104-105.

[150] Rogers A A A, Samson S, Kedia S. Far-field evanescent wave propagation using coupled subwavelength gratings for a MEMS sensor[J]. JOSA A, 2009, 26(12): 2526-2531.

[151] Li X, Xu H, Xiao X, et al. Demonstration of a highly efficient multimode interference based silicon waveguide crossing[J]. Optics Communications, 2014, 312: 148-152.

[152] Ding W, Tang D, Liu Y, et al. Compact and low crosstalk waveguide crossing using impedance matched metamaterial[J]. Applied Physics Letters, 2010, 96(11): 111114.

Publication lists

Journal paper

[1] **Jiyao Yu**, Yasuo Ohtera, and Hirohito Yamada, "Highly efficient coupler for dielectric slot waveguides and hybrid plasmonic waveguides," *Jpn. J. Appl. Phys.* **57**, 052202 (2018).

[2] **Jiyao Yu**, Yasuo Ohtera, and Hirohito Yamada, "Scattering-parameter model analysis of side-coupled plasmonic Fabry-Perot filters," *Appl. Phys. A* **124**, 516 (2018).

[3] **Jiyao Yu** and Hirohito Yamada, "Design and investigation of a dual-layer grating coupler for efficient vertical fiber-chip coupling," *Appl. Phys. Express* **12**, 012004 (2019).

[4] Yasuo Ohtera, **Jiyao Yu**, and Hirohito Yamada, "Analysis of polarization interference-type BPF arrays for NRI spectroscopic imaging utilizing all-dielectric planar chiral metamaterials," *Progress In Electromagnetics Research (PIER) M* **66**(1), 1-10 (2018).

International conference and workshop

[1] **Jiyao Yu**, Yasuo Ohtera, and Hirohito Yamada, "S-matrix analysis of side-coupled type plasmonic Fabry-Perot waveguide filters," in ISPOC C-8, Sendai, Nov. (2017). [Poster]

[2] **Jiyao Yu,** Jialiang Guo, and Hirohito Yamada, "Numerical investigation of ultra-wide bandwidth waveguide crossing based on silicon slab mirrors," in International Workshop on Emerging ICT, Korea, Nov. (2018).

Domestic conference

[1] **Jiyao Yu**, Yasuo Ohtera, and Hirohito Yamada, "Study on coupling structures for

dielectric slot waveguides and hybrid plasmonic waveguides", 信学技報 vol. 117, no. 37, pp. 33-38 (2017).

[2] **Jiyao Yu**, Yasuo Ohtera, and Hirohito Yamada, "S-matrix model analysis of side-coupled type plasmonic Fabry-Perot waveguide filters," 信学技報 vol. 117, no. 142, pp. 165-170 (2017).

[3] **Jiyao Yu**, Yasuo Ohtera, and Hirohito Yamada, "S-parameter model analysis of side-coupled plasmonic Fabry-Perot filters", 第 598 回伝送工学研究会, May (2018).

[4] **Jiyao Yu**, and Hirohito Yamada, "Design of a dual port, polarization separately grating coupler for efficient fiber-chip coupling at O and C bands," 平成 30 年度 電気関係学会東北支部連合大会, 1E07, (2018).

[5] Jiawen Liu, **Jiyao Yu**, Xiangqing Zhang, and Hirohito Yamada, "Design and investigation of Q-values of a slab type space ring resonator," 平成 30 年度 電気関係学会東北支部連合大会, 1E08, (2018).

[6] Xiangqing Zhang, **Jiyao Yu**, and Hirohito Yamada, "Research on coupling between channel waveguides and slab waveguides," 平成 30 年度 電気関係学会東北支部連合大会, 1E09, (2018).

[7] Jialiang Guo, **Jiyao Yu**, and Hirohito Yamada, "Novel waveguide crossing with curved mirrors based on silicon slab waveguides" 平成 30 年度 電気関係学会東北支部連合大会, 1E10, (2018).

Acknowledge

First, I would like to express my gratitude to my supervisor Prof. Hirohito Yamada for his guidance during the past three years. I would admire his profound knowledge, which helps me effectively and positively in my research work.

Second, I would like to thank Prof. Taiichi Otsuji and Prof. Yoichi Uehara for joining my dissertation defense meeting. The experiences in the dissertation defense are unforgettable memories, which encourage me to move forward in the ocean of research.

Third, I would like to thank my (past) vice supervisor, Prof. Yasuo Ohtera for his assistance in my research work. Without his help, I could not finish those work. He taught me the most basic knowledge and tools and led me to the scientific research meticulously.

Then, I would like to thank Associate Prof. Nobuyuki Matsuda and Tomohiro Kita for their assistance in the the research as well as daily life in the lab. Not only their broadly knowledge, but their spirits and attitudes towards research make me admirable. I would also like to thank assistant Naomi Uchiyama. Many thanks for bringing me unforgettable memories.

I would also like to thank every members, both Japanese and Chinese, in the lab. I will remember the daily life spending with you in the past three years. The list is not shown here.

Finally, I would like to thank my parents and fiancee Yongwen Lai for supporting and encouraging me in these separated days. You are the most precious treasure in my life.